

**STUDY OF THE EFFECTS ON LOWER  
IONOSPHERE DUE TO SOLAR PHENOMENA  
USING VERY LOW FREQUENCY RADIO  
WAVE PROPAGATION**

**Thesis submitted for the degree of  
Doctor of Philosophy (Science)  
in  
Physics (Theoretical)  
by  
Tamal Basak**

**Department of Physics  
University of Calcutta  
2013**

## ABSTRACT

The ionosphere is a natural detector and it characteristically responds to ionizing actions of solar and other extraterrestrial ionizing agents. Electron and ion chemistry together with the degree of ionization of lower ionosphere evolve with solar radiation intensity. In my research work, I have dealt mainly with the lower ionosphere (60-80 km) i.e., the D-region and the lower E-region using subionospherically propagated Very Low Frequency (VLF) radio signal from a transmitter ( $T_x$ ) to a receiver ( $R_x$ ) through Earth Ionosphere Wave Guide. Along with the diurnal changes in the solar flux, the intense hard and soft X-ray spectrum during solar flares greatly perturb the ionospheric D-region and this is sensed by monitoring the amplitude and phase information of ground based VLF signal. Major part of my thesis is based on the analysis of several physical lower ionospheric parameters using the VLF data of NWC transmitter. The lower ionosphere shows a time delay in responding to those ionizing agents such as solar flares and this property is called the ‘sluggishness’ of the ionosphere. Through a rigorous data analysis, we show that the time delay ( $\Delta t$ ) of the ionosphere during solar flares varies with the strength of the flare ( $\phi_{max}$ ) and with local solar zenith angle ( $Z$ ) at flare occurrence times. Moreover, we report that the correlation between  $\Delta t$  and  $\phi_{max}$  is a strongly  $Z$  dependent phenomenon. We present possible physical explanations for this. Further, using  $\Delta t$ , we develop a new formulation to calculate the effective recombination coefficient ( $\alpha_{eff}$ ) during solar flares using VLF amplitude data ( $\Delta A_{max}$ ) and simulated D-region electron density ( $N_{e,max}$ ) using the Long Wave Propagation Capability (LWPC) code. Subsequently, we show that for flares which occurred close to local solar zenith,  $\alpha_{eff}$  has an inverse relation with  $\phi_{max}$ . In another work, we simulate the perturbed environment of lower ionosphere during M and X classes of flares. This required using three codes successively, namely, the GEANT4 Monte Carlo simulation, GPI chemical model and the LWPC simulation. With reasonable assumptions, this model reproduces the observed VLF signal behaviour during flares. Negative ions are the unique constituent of the D-region and this was estimated using the  $\lambda$ -parameter. We solved electron continuity equation for flare disturbed D-region and using  $N_{e,max}$  from LWPC, we evaluated the variation of  $\lambda$ . Apart from the flare studies, we also studied quiet global lower ionospheric environment over Indian subcontinent under quiet conditions. Using the default simulation model of LWPC, we obtained spatial distribution of VLF signal under ambient solar conditions during sunrise and sunset. Our results agree with observations.

The organization of my thesis is as follows. In Chapter 1, we give a brief de-

scription of the background of the subject, the basic details of the atmosphere and ionosphere. Since my thesis is related to evaluation of ionospheric parameters, which are closely related to the chemical components there, we briefly discuss the lower ionospheric chemistry also. Then we write about the radiations coming from the sun both regularly and sporadically during flares. The VLF is one of the best remote sensing tools for the lower ionosphere. The basic physics of propagation theories for VLF electromagnetic signal also discussed here along with a short and useful description on a popular LWPC code. Finally, the specific objective of this thesis, i.e., the VLF monitoring of solar flares and calculations of associated ionospheric parameters are introduced here.

In Chapter 2, we give a brief review of earlier works done specifically on the topics of this thesis. First, we state the method and results regarding effective recombination coefficient ( $\alpha_{eff}$ ) and its relation with electron density ( $N_e$ ) and other parameters. Due to the presence of a large number of complex ions in the D-region, its chemistry is complex. Several workers and groups developed simplified models based on theoretical and experimental results. We discuss three popular and realistic models among those. We also discuss the earlier works, which related the ionospheric time delay during flares with flare flux, solar zenith angle ( $Z$ ) and other significant of ionospheric perturbation.

Before going into the core analysis and results of this thesis, it is necessary to mention about the tools we are using for analysis, i.e. the VLF signal. In this Chapter 3, we mention the VLF transmitters of various frequencies and powers present worldwide. We also describe the VLF-receiver units used by Ionospheric and Earthquake research Centre (IERC) operating under Indian Centre for Space Physics (ICSP) and other receiving stations for continuous acquisition of data. The diurnal variation of the VLF data depends on the transmitter, receiving location, propagation path characteristics etc. To demonstrate that, we show the amplitude and phase response of VLF data coming from VTX, NWC, JJI etc. transmitters and recorders at IERC/ICSP and SNBNCBS using receiving systems such as Soft-PAL, SuperSID, ICSP-receiver etc. Finally, I describe the observations during the VLF-campaigns, organised by ICSP to carry out the ground work to identify the VLF signal propagation characteristics of all possible paths within Indian subcontinent. We generated several spatial VLF signal profiles for rough explanation of the campaign results.

The Chapter 4 is regarding the introduction and analysis of the time delay ( $\Delta t$ ) experienced by VLF signal with respect to the X-ray flux variation of solar flares. First, we formulate the definition of it. Then we state the detailed procedure of

the measurement of  $\Delta t$  and VLF amplitude perturbation ( $\Delta A$ ) from the VLF data. This procedure is the same for all the flares accommodated in these analysis. Now, we use this  $\Delta t$  and  $\Delta A$  for estimation of the effective recombination coefficient ( $\alpha_{eff}$ ). We use the standard definition of  $\alpha_{eff}$  and develop a theoretical model for it. The lower ionospheric  $N_e$  is calculated using amplitude-perturbation method and LWPC code. This  $N_e$  is supplied to analytical expression of  $\alpha_{eff}$ . In the second part of this Chapter, we sort all the recorded flares according to their occurrence time and strength. After detail analysis, we establish a direct relation between  $\Delta t$  and zenith angle ( $Z$ ) for weaker flares (C-class) and then report on the effects of  $Z$  on  $\Delta t$  and peak flare flux ( $\phi_{max}$ ) correlations.

The Chapter 5 describes a ionosphere-VLF coupling self-consistent model, which can reproduce the observed VLF signal perturbations during solar flare such as events. It is a three step model. In the first step, the electron and ion production rates are simulated during solar flares using a GEANT4-Monte Carlo simulation tool kit. In the second step, using three ions and electron GPI model we derive altitude profiles of electron production rates from the ionization rates. In the final step, we supply the  $N_e$  simulation results to LWPC for obtaining VLF perturbation estimates. Finally, a comparison of our predicted signal variation is done with observed ones.

In Chapter 6, we discuss the variation of negative ions during flares. For that, we concentrate on evaluating  $\lambda$ -parameter. Here we again simulate the D-region electron density, as in Chapter 4, using LWPC. We supply these results to the D-region electron continuity equation and solve it numerically to obtain the variation of  $\lambda$  during a flare at several heights.

In the final Chapter (Chapter 7), we draw our conclusions. Thereafter, we present our future plans.

## ACKNOWLEDGMENTS

It is my great pleasure to express my gratefulness to my Supervisor Prof. Sandip Kumar Chakrabarti who has a great personality with his inspiring guidance, motivated thoughts and continuous support. During my research period, his wide field of knowledge always helped me to achieve my research goal. His intuitive approach towards any problem and the critical views of the observations have encouraged me greatly. This has also changed my overall scientific thinking and attitude towards various problems. His moral support through thick and thin has been very inspiring. It is an honour for me to work with such a wonderful personality.

I express my gratitude to all the academic and non-academic staffs of S. N. Bose National Centre for Basic Sciences (SNBNCBS), Kolkata. I thank all the Professors who taught me during my stay here since I joined the PhD programme in 2008. I thank Prof. Arup K. Raychaudhuri, Director, SNBNCBS, for giving me an opportunity to work here and use the infrastructure of SNBNCBS.

I would like to acknowledge the SNBNCBS, Kolkata and Indian National Science Academy for sponsoring me to attend the Sharjah-Stanford AWESOME VLF Workshop in February, 2010, held in Sharjah, UAE and XXX URSI General Assembly and Scientific Symposium of IURS in August, 2011, held in Istanbul, Turkey respectively. I again acknowledge SNBNCBS, Kolkata for sponsoring me for the conferences, I attended within India. I thank the organizers and advisory committees of all those conferences I attended. Especially, I like to mention about the VELFRATO conference which held in SNBNCBS on March, 2010. Many important members of international scientific community attended it and I got the privilege to have long discussions with them on my research and related issues. I owe my thanks to them too. I thank Prof. K. J. W. Lynn and Prof. S. C. Chakraborty for their scientific visits to our institute and sharing their knowledge and experience with us. I thank Prof. D. Sulic for providing us training on the LWPC code. Attending all these gave me a broad overview of the current events in the fields of ionospheric physics, VLF radio science and various related topics, which enriched my research with the essence of the subject. Other important meetings, including Asia-Oceania Geosciences Society (AOGS), 7th Annual Meeting and Geosciences World Community Exhibition, in July, 2010 and 39th COSPAR Scientific Assembly, in July 2012 which I attended greatly improved my skill in this subject.

I would like to deeply acknowledge contribution of the Indian Centre for Space Physics (ICSP), Kolkata, where I spent many sessions attending and giving seminars, taking courses. I am thankful to ICSP for giving me an opportunity to take part actively in two all India VLF campaigns conducted by ICSP in December, 2008 and July, 2009 respectively. During those campaigns, I visited a couple of campaign stations, namely, the Department of Physics, University of Kashmir, Srinagar, JK and ICSP, Coochbehar branch, Coochbehar, WB. Where I got the first hand experience on real scientific experiments such as VLF-receiver system installation, data acquisition and analysis. I thank the campaign organisers for making me a part of these activities. I acknowledge Ionospheric and Earthquake Research Centre (IERC), Sitapur, WB, a branch of ICSP for providing me with excellent quality VLF signal data, which has enormously helped my research. I thank all senior scientists of ICSP, in particular, Prof. Sonali Chakrabarti for her valuable advices and support. I would like to acknowledge the members of the Department of Ionospheric and Atmospheric Sciences and Department of Instrumentation for Space Exploration, ICSP, specially Mr. Sujay Pal, Mr. Sourav Palit, Mr. Sushanta K. Mondal (presently at SKBU), Dr. Sudipta Sasmal, Mr. Surya K. Maji, Mr. Suman Ray and Mr. Debasish Bhowmick for the collaborations, scientific discussions and sharing the workload of the VLF team.

My heartiest thanks go to my all friends and colleagues of SNBNCBS whose active support and fruitful help drove my research up to the present mark. We shared very precious moments together and the joys are beyond to express in a few words. The unconditional support and love of my seniors, batchmates and juniors have enriched my last few years of life with good experiences. I do not want to mention anyone's name in particular, as all the unforgettable moments I shared with them will remain cherishable in my memory forever.

I should thank all my colleagues, past and present, in the Department of Astrophysics and Cosmology, SNBNCBS. I must mention the names of Dr. Himadri Ghosh (presently at ICSP), Dr. Kinsuk Giri, Mr. Sudip K. Garain, Mr. Arnab Deb, Mr. Abhishek Roy, Mr. V. U. J. Nwankwo and Mr. Tanumoy Pramanik. I am fortunate to share all my joyful and tough moments with them in SNBNCBS.

I acknowledge SNBNCBS and CSIR (File No. 09/575 (0088)/2010-EMR-I) for funding my research from August, 2008 to December, 2009 and from January, 2010 till date respectively.

The main encouragements behind this effort came from my Mother. I am very happy to deeply acknowledge the debts to her for her unconditional support, en-

couragement and advices to maintain the interest and enthusiasm. Lastly, I like to thank Rakhi and my family for keeping me motivated to research.

## PUBLICATIONS IN REFEREED JOURNALS

1. Effective recombination coefficient and solar zenith angle effects on low-latitude D-region ionosphere evaluated from VLF signal amplitude and its time delay during X-ray solar flares; **T. Basak**, S. K. Chakrabarti, *ApSS* (2013) (to appear).
2. Modeling of the Very Low Frequency (VLF) radio wave signal profile due to solar flares using the GEANT4 Monte Carlo simulation coupled with ionospheric chemistry; S. Palit, **T. Basak**, S. K. Mondal, S. Pal, S. K. Chakrabarti, *ACPD*, Volume 13 (2013), p.6007-6033; *ACP* (in press).
3. VLF campaign during the total eclipse of 22nd July, 2009: observational results and interpretations; S. K. Chakrabarti, S. Pal, S. Sasmal, S. K. Mondal, S. Ray, **T. Basak** et al., *JASTP*, Volume 86 (2012), p.65-70.
4. VLF signals in summer and winter in the Indian sub-continent using multi-station campaigns; S. K. Chakrabarti, S. K. Mondal, S. Sasmal, S. Pal, **T. Basak** et al., *IJP*, Volume 86, Number 2 (2012), 323-334.
5. Results of computing amplitude and phase of the VLF wave using wave hop theory; S. Pal, **T. Basak** and S. K. Chakrabarti, *Advances in Geosciences*, Vol. 27, p.1-11, Solar Terrestrial (2011).

## PUBLICATIONS IN PROCEEDINGS

1. Global Effects on Ionospheric Weather over the Indian subcontinent at Sunrise and Sunset; **T. Basak**, S. K. Chakrabarti and S. Pal, VELFRATO - 2010, *American Institute of Physics Conference Proceedings*. Vol 1286, pp 137-149, 2010.
2. VLF study of Ionospheric properties during solar flares of varied intensity for a fixed propagation path; **T. Basak**, S. Pal and S. K. Chakrabarti, General Assembly and Scientific Symposium, 2011 XXXth URSI, 13-20 Aug. 2011, doi: 10.1109/URSIGASS.2011.6051004.
3. Computation of the effects of solar phenomena on Global Ionospheric Weather using wave guide mode theory of VLF propagation; **T. Basak**, S. K. Chakrabarti and S. Pal, General Assembly and Scientific Symposium, 2011 XXXth URSI, 13-20 Aug. 2011, doi: 10.1109/URSIGASS.2011.6051009.
4. Modeling VLF signal amplitudes over Indian sub-continent during the total solar eclipse; S. Pal, **T. Basak** and S. K. Chakrabarti, General Assembly and Scientific Symposium, 2011 XXXth URSI, 13-20 Aug. 2011, doi: 10.1109/URSIGASS.2011.6051008.
5. A comparative study of VLF signals from several transmitters around the world as observed from Maitri station, Antarctica; S. Sasmal, S. K. Chakrabarti, S. Pal and **T. Basak**, General Assembly and Scientific Symposium, 2011 XXXth URSI, 13-20 Aug. 2011, doi: 10.1109/URSIGASS.2011.6051002.
6. VLF observational results of total eclipse of 22nd July, 2009 by ICSP team; S. K. Chakrabarti, S. Pal, S. Sasmal, S. K. Mondal, S. Ray, **T. Basak** and S. Maji, General Assembly and Scientific Symposium, 2011 XXXth URSI, 13-20 Aug. 2011, doi: 10.1109/URSIGASS.2011.6051005.
7. Results of VLF campaigns in Summer and Winter in Indian subcontinent; S. K. Chakrabarti, S. Pal, S. Sasmal, S. K. Mondal, S. Ray and **T. Basak**, General Assembly and Scientific Symposium, 2011 XXXth URSI, 13-20 Aug. 2011, doi: 10.1109/URSIGASS.2011.6051007.

## Contents

<b>1</b>	<b>INTRODUCTION</b>	<b>1</b>
1.1	The Earth's Atmosphere . . . . .	1
1.2	The Ionosphere . . . . .	3
1.2.1	Layers of the Ionosphere . . . . .	4
1.3	Chemistry of the lower Ionosphere . . . . .	7
1.3.1	D-region chemistry . . . . .	7
1.3.2	E-region chemistry . . . . .	7
1.4	Origin of solar radiation . . . . .	8
1.4.1	Quiet-day solar irradiation and lower Ionosphere . . . . .	8
1.4.2	Solar flares . . . . .	9
1.5	Subionospheric Very Low Frequency radio wave propagation . . . . .	11
1.5.1	VLF: A tool for remote sensing of ionosphere . . . . .	11
1.5.2	Propagation theories . . . . .	12
1.5.3	Long-Wavelength Propagation Capability Code . . . . .	15
1.6	Investigation of the D-region perturbed by flares . . . . .	16
1.6.1	VLF monitoring of solar flares . . . . .	16
1.6.2	Estimation of D-region parameters using VLF . . . . .	18
<b>2</b>	<b>EARLIER WORKS ON SOLAR RADIATION EFFECTS ON LOWER IONOSPHERE</b>	<b>20</b>
2.1	Solar radiation and D-region of the ionosphere . . . . .	20
2.2	Perturbation of the D-region by Solar flares . . . . .	20
2.2.1	Recombination processes during flares . . . . .	20
2.2.2	D-region chemical models . . . . .	23
2.3	Ionospheric time delay during flares . . . . .	24
<b>3</b>	<b>DIURNAL VARIATION OF VLF SIGNAL OBTAINED THROUGH ALL INDIA CAMPAIGNS</b>	<b>27</b>
3.1	VLF transmitters and receivers . . . . .	27
3.1.1	VLF transmitters . . . . .	27

3.1.2	VLF receivers and receiving stations . . . . .	29
3.2	Diurnal behaviour of VLF signal from several transmitters . . . . .	30
3.3	Multi-station VLF campaigns . . . . .	35
3.3.1	VLF campaigns and its significance . . . . .	36
3.3.2	Outcome of the VLF campaigns . . . . .	37
3.4	Spatial profile of VLF signal . . . . .	39
3.4.1	LWPC simulation during Sunrise and Sunset . . . . .	39
<b>4</b>	<b>TIME DELAY OF VLF AMPLITUDES DURING SOLAR FLARES</b>	<b>41</b>
4.1	Introduction to Time Delay . . . . .	41
4.2	Comparison of VLF and X-ray data during flare . . . . .	42
4.2.1	Measurement of VLF amplitude perturbation . . . . .	42
4.2.2	Measurements of Time Delay . . . . .	43
4.3	Effective recombination coefficient during a solar flare . . . . .	45
4.3.1	Introduction to effective recombination coefficient during a solar flare . . . . .	45
4.3.2	Theoretical formulation for effective recombination coefficient	45
4.3.3	LWPC simulation of the D-region electron density during flares	48
4.3.4	Estimation of effective recombination coefficients using Time Delay . . . . .	51
4.4	Solar zenith angle effects on Time Delay . . . . .	53
4.4.1	Direct correlation between the solar zenith angle and the time delay during C-class flares . . . . .	54
4.4.2	Zenith angle effects on the correlation between peak flare flux and time delay . . . . .	56
<b>5</b>	<b>MODELLING OF VLF SIGNALS PERTURBED BY SOLAR FLARES</b>	<b>63</b>
5.1	Overview of the model and the background . . . . .	63
5.2	The Model . . . . .	64
5.2.1	GEANT4 Monte Carlo simulation . . . . .	64
5.2.2	The Glukhov-Pasco-Inan chemical model . . . . .	66
5.2.3	LWPC modelling of VLF signal response . . . . .	73
5.3	Results and interpretation . . . . .	74

<b>6</b>	<b>BEHAVIOUR OF NEGATIVE IONS IN D-REGION DURING A SOLAR FLARE</b>	<b>77</b>
6.1	Introduction to $\lambda$ -parameter . . . . .	77
6.2	Theoretical formulation of $\lambda$ . . . . .	78
6.2.1	LWPC simulation for enhanced electron density . . . . .	78
6.2.2	Solution of the continuity equation for the electrons . . . . .	81
6.3	Results . . . . .	82
<b>7</b>	<b>CONCLUSIONS AND FUTURE PLAN</b>	<b>84</b>

## List of Figures

1.1	Schematic diagram showing the height distribution of atmospheric layers along with its typical temperature profile. Figure taken from <a href="http://www.ces.fau.edu">http://www.ces.fau.edu</a> . . . . .	2
1.2	Schematic diagram showing the height profile of typical electron densities at different ionospheric layers. Differences in values during solar maxima and solar minima are shown separately. Figure taken from <a href="http://www.weather.nps.navy.mil/">http://www.weather.nps.navy.mil/</a> . . . . .	5
1.3	Typical blackbody like solar energy spectrum. The spectrum inside and outside atmosphere are indicated. Thus, the different absorption lines of molecules are shown. Figure taken from <a href="http://www.csr.utexas.edu">www.csr.utexas.edu</a> . . . . .	8
1.4	Image of the sun showing solar flares at the coronal loop near the equatorial region of the sun on a day of solar cycle-24 in the year 2011. Figure taken from <a href="http://ilcorvopasta.com/">http://ilcorvopasta.com/</a> . . . . .	10
1.5	The schematic diagram of reflection of the 1st hop and the 2nd hop of propagating VLF-rays (from VLF transmitter to receiver) by D-region ionosphere under both solar-quiet (green rays) and active (violet rays) conditions. The $h_q$ is the typical reflection height, and due to extra X-ray (and EUV-ray) radiation from sun (e.g., solar flares) the lowered reflection height is denoted as $h_{act}$ . . . . .	12
1.6	The amplitude A (left) and phase (right) of VLF signals transmitted from NWC (19.8 kHz), as a function of time as recorded at IERC(ICSP), Sitapur (22° 27'N, 87° 45'E) on 16th Feb (solid line) and 12th Feb (dotted line) 2011. Six solar flares of different classes (C2.08 at 06:37 hrs, M1.01 at 07:11 hrs, C5.96 at 11:19 hrs, M1.15 at 13:14 hrs, C9.91 at 14:43 hrs and C3.3 at 16:04 hrs) were recorded on 16th Feb 2011. All times are in IST(=UT+5.5 hrs) (Basak and Chakrabarti, 2013a). . . . .	17

- 1.7 The Great Circular Path (GCP) of VLF signal propagation from NWC to IERC transmitter is shown (maroon line). The geomagnetic equator (black thicker line) is also drawn to show the transequatorial nature of the mentioned path. The path is also mixed type as it passes over both the land and the sea (Figure adopted from *www.turkey-visit.com*). . . . . 18
- 2.1 The effective recombination coefficient is plotted as the function of peak flare flux at 74.1 km height for 25 Flare induced Amplitude Enhancement (FAE) events, as calculated by Zigman et al. (2007). . . 21
- 2.2 The effective recombination coefficient in several heights of D-region ionosphere at the relaxation regime of the M1-class solar flare occurred on 18th Feb, 2011 (Nina et al, 2012). . . . . 22
- 2.3 The excess VLF amplitude is plotted as a function of corresponding X-ray intensity. The data recorded at Dunedin, NZ for NLK/24.8 kHz signal located at Settle. The propagation path length is 12300 km. For the flares corresponding to black dots, squares and open circles successively, the respective average solar zenith angle over the propagation path increases (Thomson and Clilverd, 2001). . . . . 25
- 2.4 The same observables are plotted as Fig. 2.3 but this data is emitted from French transmitter/18.3 kHz and recorded at Cambridge, UK. This path length is only 617 km and zenith angle variation over path is negligible. The flares indicated by black dots have zenith angle  $<60^\circ$  and it is within  $60^\circ$  and  $75^\circ$  for those with open diamonds (Thomson and Clilverd, 2001). . . . . 26
- 3.1 In the Figure above, the locations of the VLF transmitters mentioned in Section 3.1.1 and several others are indicated on a world map (red circle). Also, the IERC/ICSP VLF receiving station is indicated (green circle). (Figure adopted from *www.nova.stanford.edu*.) In the Figure below, images of VLF transmitter VTX (left) at Vijayanaranam ( $8^\circ 26'N, 77^\circ 44'E$ ), India and NWC (right) at North-West Cape ( $21^\circ 48'S, 114^\circ 9'E$ ), Australia (Figure taken from *https://maps.google.co.in*). 28

- 3.2 The transmitter-receiver VLF propagation Great Circular Paths (GCP) are drawn using coloured lines. The propagation paths are, (i) NWC-IERC (red line), (ii) VTX-IERC (blue line), (iii) JJI-IERC (brown line), (iv) NWC-SNBNCBS (green line), (v) VTX-SNBNCBS (violet line) (Figure adopted from *www.outline-world-map.com*). . . . . 30
- 3.3 The amplitude ( $A$ ) (red line) and phase (black line) of VLF signals transmitted from NWC/19.8 kHz, as a function of time as recorded at IERC/ICSP, Sitapur ( $22^{\circ} 27'N$ ,  $87^{\circ} 45'E$ ) on 12th Feb 2011. All times are in IST (=UT+5.5 hrs) (Basak and Chakrabarti, 2013a). . . 31
- 3.4 The amplitude ( $A$ ) of VLF signals transmitted from VTX/18.2 kHz (above) and JJI/22.2 kHz (below), as functions of time are recorded at IERC/ICSP, Sitapur ( $22^{\circ} 27'N$ ,  $87^{\circ} 45'E$ ) on 23rd Feb and 4th Aug 2011 respectively (see also, Chakrabarti et al. 2012a). . . . . 33
- 3.5 The amplitude of the ( $A$ ) VLF signal transmitted from NWC/19.8 kHz (above) and VTX/18.2 kHz (below), as functions of time, are recorded at SNBNCBS, Kolkata ( $22^{\circ} 34'N$ ,  $88^{\circ} 24'E$ ) on 4th Apr and 25th Apr 2011 respectively. . . . . 34
- 3.6 The normalised VLF amplitude ( $A$  in dB) diurnal variation data for Kashmir ( $34^{\circ} 08'N$ ,  $74^{\circ} 51'E$ ) (above), JK and Coochbehar ( $26^{\circ} 19'N$ ,  $89^{\circ} 28'E$ ) (below), West Bengal. The data was recorded during the summer and winter VLF campaigns respectively. Sunrise and sunset time at receiving sites are indicated by arrows (Chakrabarti et al., 2012a). . . . . 37
- 3.7 The variation of VLF signal amplitude as a function of the distance between the transmitter and receiver, as simulated from default propagation model of LWPC. The VTX-Kashmir (above) (2867 km) and VTX-Coochbehar (below) (2347 km) propagation paths are shown. The VLF data receiving points are indicated by  $R$  (Chakrabarti et al., 2012a). . . . . 38
- 3.8 The LWPC simulated spatial amplitude distribution of VTX/18.2 kHz signal over the Indian subcontinent at 6:00am (top) and 6:30pm (bottom) (IST) on a winter day. The VLF signal amplitude has been shown with colour variation and also contours of constant amplitude (in dB) are drawn. The VTX transmitter is located at the origin of this plot (Basak et al., 2010). . . . . 39

4.1 A typical example of  $\Delta t$ , the time delay of the VLF signal during an M1.46-class flare. The solid curve represents a typical soft X-ray irradiance  $\phi$  ( $\text{W m}^{-2}$ ) and the dashed curve represents the corresponding VLF amplitude deviation. The date and time are written in the ddmmyy\_hhmm format.  $\Delta A$  is in dB (Basak and Chakrabarti, 2013a). . . . . 42

4.2 Examples of (a) X-class (b) M-class and (c) C-class solar X-ray flares as recorded by GOES-15 (solid lines) along with corresponding VLF signal amplitude deviations ( $\Delta A$ ) obtained by ICSP receivers (dashed lines). Date and time (ddmmyyyy\_hhmm) are marked in respective panels (Basak and Chakrabarti, 2013a). . . . . 43

4.3 A schematic diagram showing the meaning of  $\Delta t$ , the time delay of the VLF signal. The solid curve represents a typical soft X-ray irradiance  $\phi$  ( $\text{W m}^{-2}$ ) and the dashed curve represents the corresponding VLF amplitude deviation ( $\Delta A$ ) in dB (Basak and Chakrabarti, 2013a). . . 44

4.4 Simulated effective reflection height ( $h'$ ) (km) is plotted with corresponding peak flare flux ( $\phi_{max}$ ) ( $\text{W m}^{-2}$ ) (Basak and Chakrabarti, 2013a). . . . . 48

4.5 Simulated sharpness factor ( $\beta$ ) ( $\text{km}^{-1}$ ) is plotted with corresponding peak flare flux ( $\phi_{max}$ ) ( $\text{W m}^{-2}$ ) (Basak and Chakrabarti, 2013a). . . . 49

4.6 (a) Simulated D-region electron density (circles) ( $N_{e,max}$ ) ( $\text{m}^{-3}$ ) at  $h = 74$  km is plotted with corresponding peak flare flux ( $\phi_{max}$ ) ( $\text{W m}^{-2}$ ) (b) Also  $N_{e,max}$  (squares) calculated at  $h = 74.1$  km using  $\alpha_{eff}$  values taken from Zigman et al. (2007) (Basak and Chakrabarti, 2013a). 50

4.7 VLF amplitude time delay ( $\Delta t$ ) is plotted as a function of corresponding peak flare flux ( $\phi_{max}$ ,  $\text{W m}^{-2}$ ) for the same flares shown in Fig. 4.6 (Basak and Chakrabarti, 2013a). . . . . 51

4.8 Effective reflection coefficient ( $\alpha_{eff}$ ) ( $\text{m}^3\text{s}^{-1}$ ) is plotted with corresponding peak flare flux ( $\phi_{max}$ ) ( $\text{W m}^{-2}$ ) (Basak and Chakrabarti, 2013a). . . . . 52

4.9 Solar zenith angle ( $Z$ ) and solar elevation angle ( $E$ ). . . . . 53

4.10 The time delay ( $\Delta t$ ) (s) of the ionosphere for each C-class solar flare is plotted as a function of their occurrence time  $t(\text{mins})$ . The solid line is the fitted mean curve for these data points (Basak and Chakrabarti, 2013a). . . . . 55

4.11	The time delay ( $\Delta t$ ) (s) of the ionosphere for each C-class solar flare is plotted as a function of $Z$ at their occurrence time. The solid line is the fitted straight line for those data points (Basak and Chakrabarti, 2013a). . . . .	56
4.12	Schematic diagram of the positions of the sun at $DT1$ to $DT6$ time bins. . . . .	58
4.13	Variation of the mean zenith angle ( $Z$ in deg.) as a function of $T_x$ - $R_x$ path at middle of time-bins mentioned in Table 4.2. $T_x$ is at $d = 0$ km and $R_x$ is at $d = 5691$ km (Basak and Chakrabarti, 2013a). . . . .	59
4.14	The time delay [ $\Delta t(s)$ ] for each of the solar flares has been plotted as a function of peak flare flux ( $\phi_{max}$ in $W m^{-2}$ ). The solid line is the fitted empirical function (Eqn. 4-13). The time bins are (a) $DT1$ , (b) $DT2$ and (c) $DT3$ (Basak and Chakrabarti, 2013a). . . . .	60
4.15	The same plot of time delay ( $\Delta t$ ) as in Fig. 4.14. The time bins are (a) $DT4$ , (b) $DT5$ and (c) $DT6$ (Basak and Chakrabarti, 2013a). . . . .	61
4.16	The <i>reduced</i> - $\chi^2$ (circle) and the standard deviation ( $\sigma$ ) (diamond) of the zenith angle ( $Z$ ) along $T_x$ - $R_x$ path as functions of $DT1$ , $DT2$ , $DT3$ etc (Basak and Chakrabarti, 2013a). . . . .	62
5.1	Electron density at different layers during the (a) M-class flare. The time started from 6:56:40 UT (Palit, Basak et al., 2013). . . . .	67
5.2	Electron density at different layers during the (b) X-class flare. The time started from 01:23:20 UT (Palit, Basak et al., 2013). . . . .	68
5.3	Altitude profiles of electron density as obtained from the GPI model at three different times for an M-class flare. Solid line shows the ambient profiles before the beginning of the flare while the dashed and the dot-dashed lines represent the profile during the peak and at a time during recovery (Palit, Basak et al., 2013). . . . .	69
5.4	Same as Fig. 5.3 but for an X-class flare. Solid line shows the ambient profile before the beginning of the flare while the dashed and the dot-dashed lines represent the profiles during the peak and at a time during recovery (Palit, Basak et al., 2013). . . . .	70
5.5	Altitude profile of the negative ions as obtained from the GPI scheme. Solid, dashed and dot-dashed lines represent respectively the ambient profile, that at the peak and at a time during recovery of the X-type flares discussed in the text (Palit, Basak et al., 2013). . . . .	71

5.6	Same as Fig. 5.5 except for positive ions. Solid, dashed and dot-dashed lines represent respectively the ambient profile, that at the peak and at a time during recovery of the X-type flares discussed in the text (Palit, Basak et al., 2013). . . . .	72
5.7	Same as Fig. 5.5 except for the Positive Cluster ions. Solid, dashed and dot-dashed lines represent respectively the ambient profile, that at the peak and at a time during recovery of the X-type flares discussed in the text (Palit, Basak et al., 2013). . . . .	73
5.8	Simulation results of VLF amplitude modulations (dotted line) and corresponding observed VLF data (solid line) are plotted with UT for an M-class solar flare (Palit, Basak et al., 2013). . . . .	74
5.9	Same as Fig. 5.8 except for an X-class solar flare (Palit, Basak et al., 2013). . . . .	75
6.1	VLF amplitude ( $\Delta A$ in dB) (blue line) and phase (deg.) (red line) response of NWC/19.8 kHz signal during the M1.92 class solar flare is presented. Date and flare peak times are shown in <i>yyyymmdd.hhmmss</i> format (Basak and Chakrabarti, 2013b). . . . .	78
6.2	Wait's model parameters, effective reflection height ( $h'$ in km) and sharpness factor ( $\beta$ in $\text{km}^{-1}$ ) variations during an M1.92 class flare (as obtained from the LWPC simulation) are shown (Basak and Chakrabarti, 2013b). . . . .	79
6.3	D-region electron density ( $N_e$ in $\text{m}^{-3}$ ) (green line) at a height of 74 km as simulated using LWPC, has been plotted along with solar flare X-ray flux density ( $\phi$ in $\text{Watt m}^{-2}$ ) (blue line) as measured by GOES-15 during an M1.92 class flare (Basak and Chakrabarti, 2013b). . . . .	80
6.4	Time derivative of D-region electron density ( $\frac{dN_e}{dt}$ in $\text{m}^{-3}\text{s}^{-1}$ ) at several heights (65-75 km) as simulated using LWPC. Different heights are indicated with separate colours (Basak and Chakrabarti, 2013b). . . . .	81
6.5	The altitude profile of $\lambda$ -parameter at different times during the M1.92 class flares. Different colours indicate different times (Basak and Chakrabarti, 2013b). . . . .	82
6.6	$\lambda$ -parameter variation during the M1.92 class flare at several D-region heights (Basak and Chakrabarti, 2013b). . . . .	83

## List of Tables

4.1	Data sheet of all included flares (Basak and Chakrabarti, 2013a) . . .	47
4.2	Details of flares in different time-bin (Basak and Chakrabarti, 2013a)	57

## Chapter 1

# INTRODUCTION

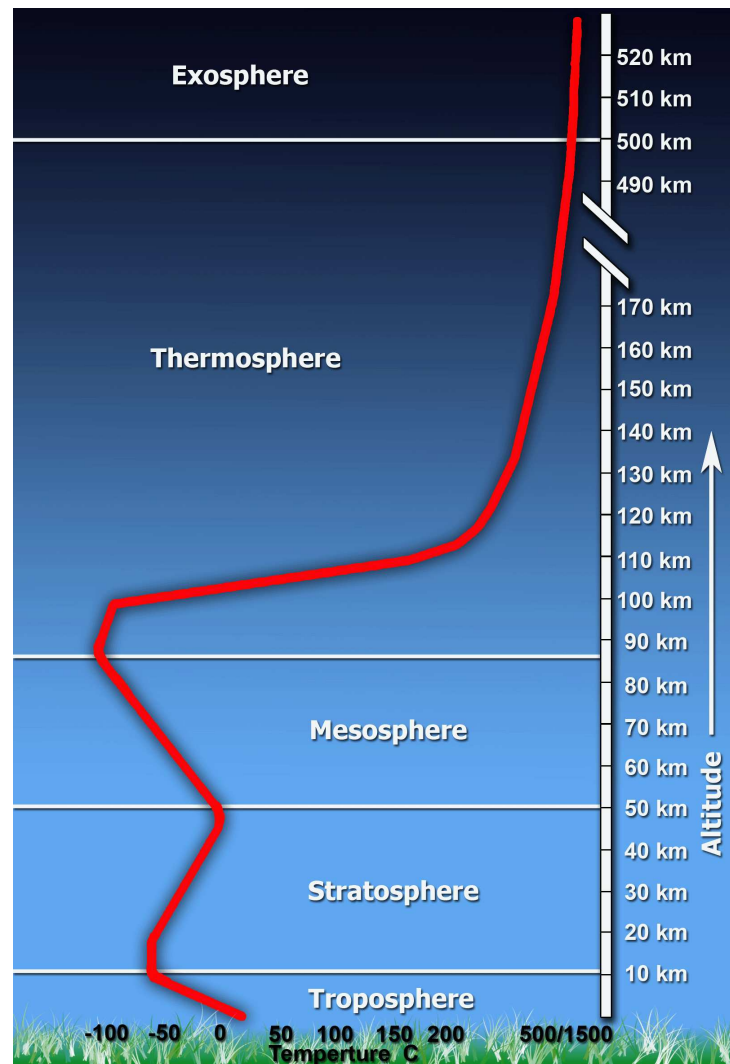
### 1.1 The Earth's Atmosphere

The mixed gaseous medium surrounding the earth is called the atmosphere. It consists of numerous components and complex chemical, mechanical, thermodynamic and fluid dynamic effects occur within it every moment. The existence and survival of life in various forms, on and around the surface of the earth has come into being due to this atmosphere around it. The nitrogen ( $N_2 \sim 78.09\%$ ), oxygen ( $O_2 \sim 20.95\%$ ), Carbon dioxide ( $CO_2 \sim 0.039\%$ ), water vapour ( $H_2O \sim 1\%$ ) are the major active and argon ( $Ar \sim 0.93\%$ ), hydrogen ( $H_2$ ), helium ( $He$ ), ozone ( $O_3$ ) etc. are other trace components of it. Though the atmosphere is spread above for nearly a thousand kilometres, almost 80% of the total mass of it lies within only 12 km from the surface of the earth. Based on the physical property variation, it is divided into five different spherical shells, namely, (i) troposphere (ii) stratosphere (iii) mesosphere (iv) thermosphere and (v) exosphere. These shells with corresponding temperature distribution are shown in Fig. 1.1.

#### *The Troposphere*

It is the lowermost layer of the atmosphere and it is in touch with the earth's surface. This is extended up to 10 – 12 km height. It consists of the major component of the atmosphere as mentioned in the earlier Section. Nearly 80% of the entire mass of the atmosphere is in this layer and obviously its density is highest because of that. The temperature decreases as the height goes up in this layer.

The unstable inversion layer in between the troposphere and stratosphere is called 'tropopause'.



boundary layer at about 55 km between it and mesosphere is called the ‘stratopause’.

### *The Mesosphere*

From the top of the stratopause, the mesosphere extends up to  $\sim 85$  km. It is the lowermost ionized layer of atmosphere and temperature goes down up to 190 K in this layer. Indeed, it is the coolest layer of atmosphere. The ionized D-region lies within this layer and the detail discussions are in the following Sections.

### *The Thermosphere*

The region between 85 km and 600 km is called the thermosphere. The reason of this nomenclature is the constant increase of temperature with height within this layer. The temperature may go up to 1750K. The deposition of solar energy in UV, EUV and X-ray regions to this layer is the principle reason for this enhancement. The wide variation of the chemical activities of this layer is given in the next Section.

### *The Exosphere*

The outermost sphere ( $> 600$  km) is called the exosphere. It ends at interplanetary gases. Due to low gravity at such an altitude, this layer contains only light gases such as the hydrogen and helium. The collision frequency among the light gas particles here is almost zero and thus the charged particles are free to move to the magnetosphere.

The ionized atmospheric layer at around 50 – 1000 km is the ‘ionosphere’, where actually the mesosphere, thermosphere and partly the exosphere lay together. This is the region of interest in this thesis. Details about the ionosphere are written in next Section.

## **1.2 The Ionosphere**

The thick ionized layer surrounding the earth between 50 km to 600 km height from the earth surface is called the ionosphere. The ionosphere includes the mesosphere ( $\sim 50 - 100$  km), thermosphere ( $\sim 100 - 600$  km) and partly the exosphere ( $> 600$  km). The ionosphere is first discovered by the famous physicist C. F. Gauss in 1839. In 1869, Lord Kelvin also proposed the existence of a thick conducting layer. In 1901, G. Marconi invented the trans-Atlantic radio communication and

then O. Heaviside, A. Kennely and K. Nagaoka discovered the role of the ionized layer responsible for such a long distance radio communication. Later scientists such as J. E. Taylor, J. A. Fleming, G. W. Pierce and others established the existence of ionosphere through various experiments.

The spread of the ionosphere is from the neutral dense lower atmosphere to the lower edge of the magnetosphere. It is the most chemically dynamic part of the atmosphere. It consists of free electrons, ions, neutral atoms, molecules etc. Its chemical ionic constituents, electron and ion-temperature, pressure, average mass density, conductivity, chemical reaction rates and other characteristics change widely from height to height. Based on this variations, the ionosphere is divided into different layers, namely, D-region, E-region, sporadic E-region and F-region as one goes from lower to higher altitudes. Some details of these regions are discussed in the next Section (Mitra, 1992).

The radio wave propagation within the earth-ionosphere cavity takes place due to the free electron content of lower ionosphere. The free electron plasma causes the reduction of dielectric constant to less than unity and that is the reason it reflects the electromagnetic wave back to the earth (Mitra, 1992). The electron density of the ionospheric plasma required to reflect the ray back surely depends on the frequency of the ray, angle of incidence and other related parameters. Basic theoretical formulation of the radio wave propagation in presence of the geomagnetic field is called ‘the magneto-ionic theory’ and it is developed by Appleton and Hartree (Appleton, 1925). Due to the presence of this magnetic field, the ionospheric composition has a strong latitude dependence.

### 1.2.1 Layers of the Ionosphere

The structure of the ionosphere is highly variable. A model to estimate the altitude profile of ionization in the ionosphere was first proposed by Sydney Chapman (Mitra, 1992, Tascione, 1994; Hunsucker and Hargreaves, 2003), who theoretically modelled the absorption of parallel rays of monochromatic radiation coming from the sun and obliquely striking the upper atmosphere.

An electron density profile of ionized region is obtained using Chapman’s theoretical analysis. To accurately model the ionosphere, a number of Chapman layers are constructed with appropriate values of different model parameters. These layers are labelled, namely, D, E, F1, and F2, the superposition of which constitutes an ionization model that approximates the actual ionosphere (Tascione, 1994) (see Fig. 1.2).

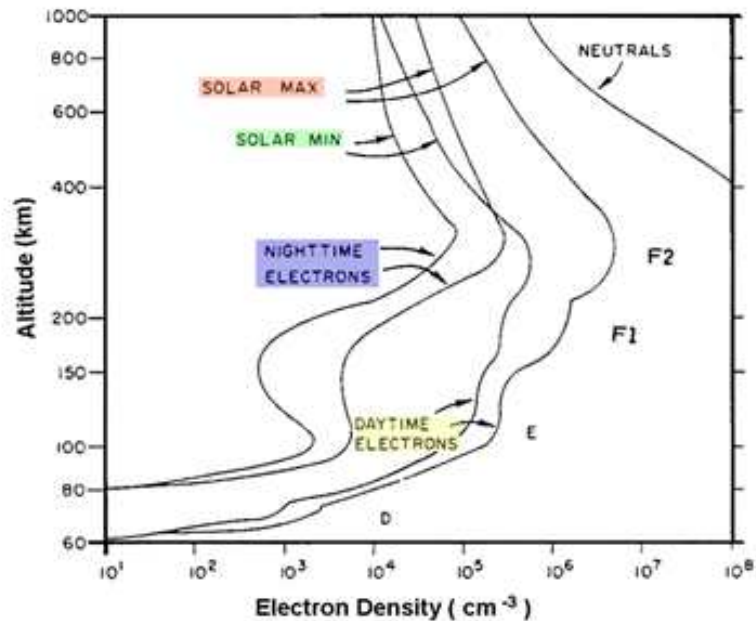


Figure 1.2: Schematic diagram showing the height profile of typical electron densities at different ionospheric layers. Differences in values during solar maxima and solar minima are shown separately. Figure taken from <http://www.weather.nps.navy.mil/>.

### *D-region*

The D-region is the lowermost layer of ionosphere. It is spread from 50 km to 90 km height. This is not a permanent layer of the ionosphere as it forms due to the  $L\alpha$  radiation (1216Å wavelength) coming from the sun. So this layer is almost absent during the nighttime apart from a minimum ionization effect due to cosmic radiations. Main components of this layer is nitric oxide (NO),  $N_2$ ,  $O_2$ , O etc. The  $N_2$  and  $O_2$  are mainly produced because of hard X-ray radiation. The negative ions are unique contents of this region. The typical free electron density of this layer is  $\sim 10^8 m^{-3}$ . The recombination processes are dominant here for such a high density. During flares, the electron density goes to 100 times higher value than the typical one. It has variation with solar zenith angle ( $Z$ ) and geomagnetic field. The mean temperature drops from 260K to 180K as height increases in this layer.

*E-region*

The E-region is located just above the D-region. The soft X-ray and far UV radiation are the main ionizing sources here. The  $L_{\beta}$  (1026Å) line ionizes molecular  $O_2$  in this region. Main molecular ions in this region are  $O_2$  and  $N_2$ , and main ions are  $O_2^+$  and  $NO_2^+$ . This is a permanent layer of ionosphere and varies with the solar zenith angle. During the dawn and the dusk, the reactions in this region become complex. Temperature in this layer increases with an increasing height. According to the names of its discoverers, this E-layer is also known as ‘Kennelly-Heaviside’ layer.

*Sporadic E-layer*

Within the E-layer, a thinner layer is situated, which is called the ‘Sporadic E-layer’ ( $E_s$ ). Origin of this layer is the transportation of metallic ions vertically with winds, tides, gravity waves etc. The metallic ions are  $Na^+(23^+)$ ,  $Mg^+(24^+)$ ,  $Mg^+(26^+)$ ,  $Al^+(27^+)$  and several others. The hydrated metallic ions are  $Na^+(H_2O)$ ,  $NaOH^+$  etc. It was experimentally observed that it has drastic density changes at the edge, and thickness of this layer may change from a few meters to several kilometres.

*F-region*

The F-region is subdivided into two layers, namely, F1 and F2. The F1-region is situated in 160 – 200 km height. The UV-radiation within  $100 < \lambda < 900 \text{Å}$  wavelength range ionizes it. Main ions here are  $NO^+$ ,  $O_2^+$  and  $O_2$  etc. Though the ion-molecular reactions here are mostly similar to those of the E-region, the ion-temperature and the electron-temperature are very different, and that is the reason for the unique identification of this layer.

*F2-layer*

The F2-layer is the uppermost layer of the ionosphere and it resides within the thermosphere. It is typically within 250 – 500 km height and largely depends on local geophysical situation. Here, the plasma density is maximum and it is able to reflect back the radio signal of frequency range from 1MHz to 30MHz. The same wavelength responsible for ionization in F1-region, also does ionization here. The ion constituents here are O,  $N_2$  and  $O_2$ . At heights above 700 km, the  $O^+$ ,  $He^+$ ,  $H^+$  ions are found. The uniqueness of this layer is the ionization loss rate, which is proportional to ion concentration directly due to very low ion density, but in cases

of other layers, this proportionality holds with the square of the ion concentration. The day-night variation of this layer is very wide.

We presented above a brief introductory discussion about the whole ionosphere. In this thesis, we shall investigate the lower ionosphere under quiet and perturbed environments. Hereafter, we shall concentrate on this region.

## 1.3 Chemistry of the lower Ionosphere

### 1.3.1 D-region chemistry

Though the D-region is the thinnest layer of ionosphere, its ion composition is most complex. The water cluster ion such as  $\text{H}^+(\text{H}_2\text{O})_n$  dominates both at daytime and nighttime below  $\sim 82$  km. Within a height range of 75 – 85 kms, the  $[\text{H}_5\text{O}_2^+]$  concentration is  $10^9\text{m}^{-3}$  at daytime but drops by six orders of magnitude typically at nighttime (Mitra, 1974). During the dawn and the dusk ( $\chi \sim 90^\circ$ ), the ion content changes by a factor of  $\sim 4$ . The sudden reduction of amount of cluster ions occurs at  $\sim 82$  km height at daytime and  $\sim 87$  km height at nighttime. But this height is drastically reduced to  $\sim 72$  km at high-latitude ‘polar cap’ regions.

The negative ions are found below  $\sim 70$  km height (Narcisi et al. 1971). These ions are  $\text{O}^-$ ,  $\text{O}_2^-$ ,  $\text{Cl}^-$ ,  $\text{NO}_2^-$ ,  $\text{NO}_3^-$ ,  $\text{CO}_3^-$ ,  $\text{HCO}_3^-$ ,  $\text{CO}_4^-$ ,  $\text{NO}_3^-(\text{H}_2\text{O})$ ,  $\text{CO}_3^-(\text{H}_2\text{O})$ . The  $\text{NO}_3^-$  and  $\text{CO}_3^-$  are dominant among those (Narisi et al, 1971). The  $\lambda$ -parameter which is the ratio of the negative ion to electron density, decreases by almost 10 times as the height in the D-region increases. Finally it becomes zero hereafter.

### 1.3.2 E-region chemistry

The  $\text{NO}^+$  and  $\text{O}_2^+$  are dominant ions of the E-region. After sunset, the molecular oxygen  $[\text{O}_2^+]$  decays by two orders of magnitude. The atomic  $[\text{O}^+]$  oxygen totally gets consumed by ion chemical reactions. The  $\text{NO}^+$  and  $\text{O}_2^+$  values get reversed at nighttime compared to the daytime values. At nighttime, the  $\text{NO}^+$  dominates in the lower E-region and the  $\text{O}_2^+$  is almost constant ( $10^8\text{m}^{-3}$ ) at higher E-regions. As one goes up to F1-region, both  $\text{NO}^+$  and  $\text{O}_2^+$  values become higher.

The sporadic E-layer consists of metallic ions like magnesium, sodium, silicon etc., as reported by Narcisi et al. (1969).

## 1.4 Origin of solar radiation

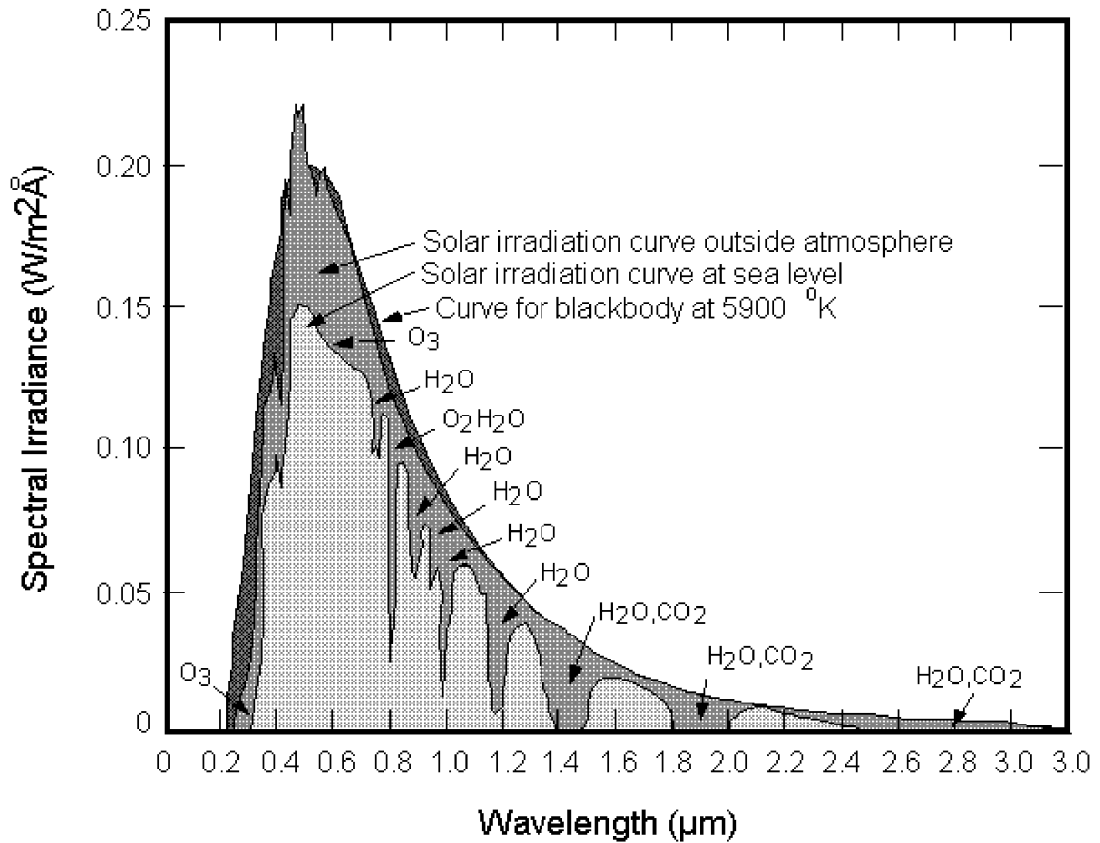


Figure 1.3: Typical blackbody like solar energy spectrum. The spectrum inside and outside atmosphere are indicated. Thus, the different absorption lines of molecules are shown. Figure taken from *www.csr.utexas.edu*.

### 1.4.1 Quiet-day solar irradiation and lower Ionosphere

The sun is a typical star. It emits continuous plasma stream and burst of energetic particles and above all, the electromagnetic radiation over the entire spectral range (see Fig. 1.3). The major ionizing source of mesospheric layers are from  $1\text{\AA}$  to  $1300\text{\AA}$  wavelength radiations. The  $\text{O}_2$  of all layers are dissociated by far-UV broad Schumann continuum from  $1350\text{\AA}$  to  $1750\text{\AA}$ . During the solar-quiet conditions, only radiation in  $100\text{\AA}$  to  $1300\text{\AA}$  are dominant. The  $L\alpha$  ( $1216\text{\AA}$ ) are responsible for the

creation and the variation of daytime D-region. That is why the D-region practically disappears at nighttime. The He I (584Å) and He II (304Å) lines are responsible for F-region ionization. Softer X-rays mainly deposit their energy to lower E-region (Hinteregger, 1969; Mitra, 1974).

During solar flares, X-rays below 8Å are incident on the ionosphere and cause changes in the D-region. It is elaborated in the next Section.

### 1.4.2 Solar flares

Solar flares were first detected by Richard Carrington in 1859. Basically, they form due to a sudden release of huge magnetic energy from the solar atmosphere. The radiation emitted during flares are spread over the entire range of the electromagnetic spectrum, i.e., from gamma-ray and X-ray emissions to radio frequency emissions. Total rate of energy released during a typical flare is  $\sim 10^{20}$  Joules. A large flare can emit up to  $\sim 10^{25}$  Joules. Along with this much energy during flares, the sun may also eject electrons, ion-plasma and even heavier nuclei. This is called ‘Coronal Mass Ejection’ (CME). Being massive, these particles reach earth after a few hours to a few days of the occurrence of a flare.

Solar flares affect all the layers of the sun, namely, photosphere, chromosphere and corona. The corona is the outermost layer of the solar sphere. Corona consists of a highly rarefied gas having temperature  $\sim 10^6$  K. But during flares, it goes higher up to  $10^7$  to  $10^8$  K. It is to be noted that, the corona is not equally bright everywhere on the solar surface. It is concentrated mostly around the equatorial region due to the dynamic magnetic field orientations of the sun (see, Fig. 1.4). The bright coronal loops are located near the stronger magnetic field region. These regions are called ‘active regions’. Generally, the sunspots are around these active regions and also the solar flares are originated there. Solar flare occurrence rate is directly related to the eleven year solar cycle. During solar maxima, this rate increases significantly. All the flares analysed in this thesis are recorded during the solar maxima in the year 2011.

In general, there are three phases of a solar flare. The initial phase is called the ‘precursor’, when the sudden energy burst is just initiated. Soft X-rays are emitted from the corona in this phase. The second phase is ‘impulsive’, where streams of electrons and protons are accelerated. They may go up to high energy of 1 MeV. The hard X-rays and gamma rays are emitted in this stage. In the final ‘decay’ stage, this soft X-ray part starts to diminish gradually. This stage may last from a few minutes to several hours.

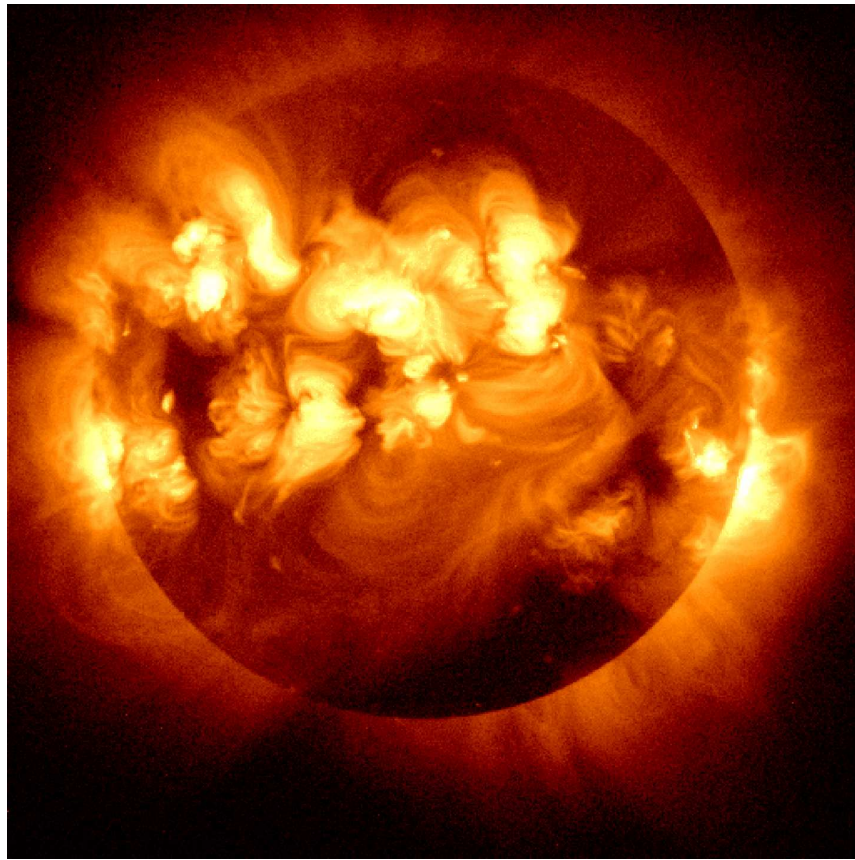


Figure 1.4: Image of the sun showing solar flares at the coronal loop near the equatorial region of the sun on a day of solar cycle-24 in the year 2011. Figure taken from <http://ilcorvopasta.com/>.

Among the entire flare emission spectrum, the X-ray and Ultra Violet (UV) radiation affect the earth's ionosphere. This perturbs the subionospheric radio communication. By monitoring VLF radio signal amplitude and phase information, the ionospheric changes can be mapped. This indirect investigation of the ionosphere during flares is the main objective of this thesis.

#### *Solar flare classification*

Solar flares are classified, based on its peak flux in the following way: (i) A-class ( $< 10^{-7} \text{ Wm}^{-2}$ ) (ii) B-class ( $10^{-7}$  to  $10^{-6} \text{ Wm}^{-2}$ ) (iii) C-class ( $10^{-6}$  to  $10^{-5} \text{ Wm}^{-2}$ ) (iv) M-class ( $10^{-5}$  to  $10^{-4} \text{ Wm}^{-2}$ ) (v) X-class ( $> 10^{-4} \text{ Wm}^{-2}$ ). The strongest flare

detected in history is a X28-class flare in 2003. The X-ray data of the flares used in this thesis are recorded by Geostationary Operational Environmental Satellite-15 (GOES-15) in both soft ( $1\text{\AA} - 8\text{\AA}$ ) and hard ( $0.5\text{\AA} - 4\text{\AA}$ ) X-ray energy bands. This data is available at [www.swpc.noaa.gov](http://www.swpc.noaa.gov). Subionospherically propagated VLF signal mimics the X-ray nature of the flare. Typically, minimum C-class flares are detected using VLF, as the A and B-classes are too feeble to deposit sufficient energy in lower ionospheric heights.

## 1.5 Subionospheric Very Low Frequency radio wave propagation

A Very Low Frequency (VLF) signal refers to the radio wave in the frequency range between 3 kHz to 30 kHz. Propagation of the VLF signal through the cavity made between the earth-surface as lower boundary and lower edge of ionosphere as upper boundary, by successive reflections is called the subionospheric propagation of VLF (Fig. 1.5). Thus, VLF radiation can propagate up to many thousands of kilometres. If the distance from a VLF transmitter to a receiving point is less than  $\sim 3000$  km, it is called a short path and if the path is greater than  $\sim 10000$  km, it is called a long path propagation. The rest is called medium path. While propagating, the VLF signal experiences some attenuation of signal strength, depending on the local ground conductivity.

### 1.5.1 VLF: A tool for remote sensing of ionosphere

The region of mesosphere starting from 50 km to 250 km is too high to probe through balloon borne experiments and too low to probe through satellite experiments. So, it is probed by VLF remote sensing method. The earth surface and the ionosphere do guide the VLF electromagnetic wave. The critical frequency ( $f_{critical}$ ) of lower ionospheric D-region plasma is higher than the frequency of the VLF range, so the wave is reflected from the waveguide boundaries. When a VLF radiation incidents on the D-region, only electrons, due to its much lighter mass compared to other ions, get affected. The dielectric constant, refractive index ( $\mu$ ) and hence the reflection coefficient influence the VLF radiation. The  $f_{critical}$  at a particular ionospheric height is related to lower ionospheric plasma electron density ( $N_e$ ) as,  $f_{critical} \propto \sqrt{N_e}$ . Thus subionospheric VLF signal carries the information regarding D-region  $N_e$  and other parameters. Diurnal variation of solar UV and Lyman- $\alpha$  on ionosphere are obtained

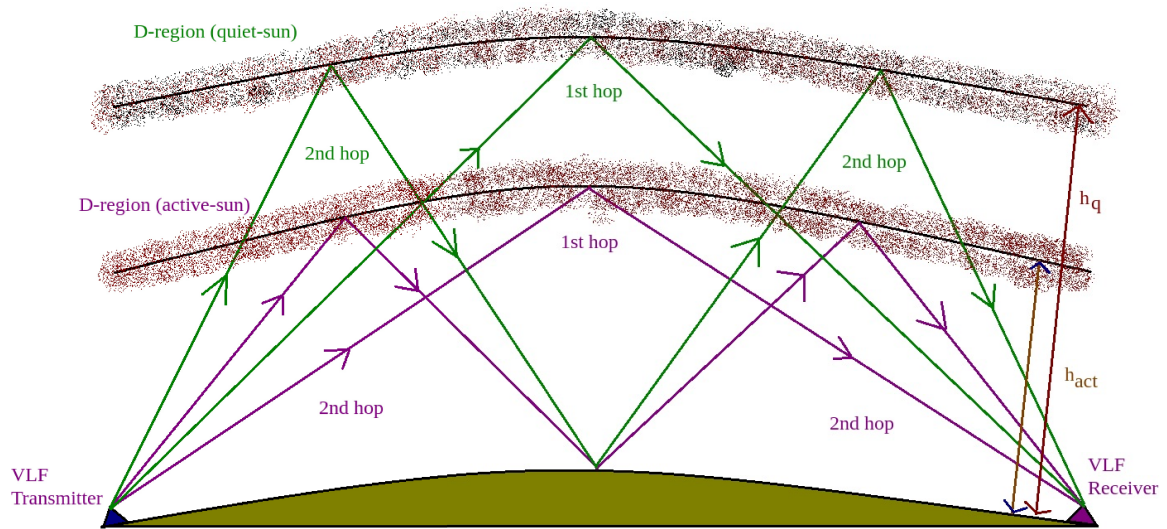


Figure 1.5: The schematic diagram of reflection of the 1st hop and the 2nd hop of propagating VLF-rays (from VLF transmitter to receiver) by D-region ionosphere under both solar-quiet (green rays) and active (violet rays) conditions. The  $h_q$  is the typical reflection height, and due to extra X-ray (and EUV-ray) radiation from sun (e.g., solar flares) the lowered reflection height is denoted as  $h_{act}$ .

by VLF measurements. Extraterrestrial high energetic sources such as solar flares and extragalactic sources such as Gamma Ray Bursts (GRB), Soft Gamma Ray Repeaters (SGR) deposit their energy on the ionosphere and perturb by enhancing its free electron density. Thus, by monitoring the VLF signal data from a ground based VLF receiver, the ionospheric physics can be studied. Several theoretical propagation models are present in the literature, such as, the wave-hop theory (Berry 1964; Bain 1985; Yoshida et al. 2008; Pal & Chakrabarti 2010), waveguide mode theory (Budden 1957; Cummer 2000) etc. to handle above mentioned phenomena (see, Section 1.5.2). Based on waveguide mode theory, the Long Wave Propagation Capability (LWPC) code has been developed (Ferguson 1998). It simulates VLF signal behaviour using realistic exponential model of  $N_e(h)$ , as proposed by Wait & Spices (1964). This is elaborated in Section 1.5.3.

### 1.5.2 Propagation theories

To theoretically predict the phase and amplitude of propagating VLF signal, two different methods are available, namely, the ray theory (or wave-hop theory) and the

waveguide mode theory. Using these approaches, the Low Frequency (LF) (30kHz to 300kHz) and Extremely Low Frequency (ELF) (300Hz to 3kHz) radio waves can also be handled. An introductory discussion on them is as follows.

### *Ray theory*

In a ray treatment, basic considerations of geometrical optics are assumed and the propagating electromagnetic signal is treated as a single ‘ray’ moving on a straight line. This ray is propagating through the cavity within the earth’s surface and horizontally stratified ionospheric layers. Rays propagating here are divided into two main types, namely, (i) ground wave and (ii) sky wave. The ‘ground wave’ consists of a direct wave, wave reflected by the ground and the surface wave (Pal and Chakrabarti, 2010). Due to the spherical shape of the earth, it is dominant within only  $\sim 300$  km from the transmitters. The ground wave dominated region is called the ‘skip zone’. The ground wave effects reduce drastically as the receiver is placed beyond the line-of-sight. It is dependent on the reflection coefficient of ground and not on ionospheric changes. The rays, which propagate through successive reflections on the ground and ionospheric layers both, are called the ‘sky waves’ (see, Fig. 1.5). All the information corresponding to the physical changes on the ionosphere are carried out by this sky wave. Depending on the Great Circular Path (GCP) from the transmitter to the receiver, the total number of successive reflections are determined. The rays reached the destination after one and two sky reflections are called 1-hop and 2-hop rays respectively (Pal and Chakrabarti, 2010). Obviously, after each reflection the ray strength gets reduced. The net signal strength at the receiving point is the resultant of all these sky waves and ground waves meeting at that point. It is necessary to mention that, multiple sky waves can reach to a receiver at a time.

*Signal strength calculation:* In this approach, the VLF signal phase and amplitude at a give location beyond the skip zone is the vector sum of all the sky wave hops and the ground wave. The resultant field up to ‘ $n$ ’ hops in general is given by (Wakai, Kurihara & Otsuka, 2004; Pal & Chakrabarti, 2010),

$$I^2 = G^2 + E_1^2 + E_2^2 + E_3^2 + \dots + E_n^2 + 2E_1G \cos \phi_1 + 2E_2G \cos \phi_2 + \dots + 2E_nG \cos \phi_n + 2E_1E_2 \cos \phi_{12} + 2E_2E_3 \cos \phi_{23} + \dots + 2E_mE_n \cos \phi_{mn}, (1-1)$$

where,

$I$  = resultant electric field strength,

$G$  = electric field strength of ground wave,

$E_n$  = electric field strength of  $n$  - th hop sky wave,

$\phi_n$  = relative phase of  $n$  - th hop sky wave with respect to ground wave,

$\phi_{mn}$  = phase difference between  $m$  - hop &  $n$  - hop sky waves (provided that  $m \neq n$ ).

Now, the electric field strength of  $n$  - hop wave received by a loop antenna, is calculated in mV/m as (Wakai, Kurihara and Otsuka, 2004),

$$E_n = \frac{600\sqrt{P_t}\cos\psi R_{i1}R_{i2}R_{i3}\dots R_{in}F_{i1}F_{i2}F_{i3}\dots F_{in}R_{g1}R_{g2}R_{g3}\dots R_{g,n-1}D_{g1}D_{g2}\dots D_{g,n-1}}{L_n} \quad (1-2)$$

where,

$P_t$  = power of transmitter in kWatts,

$\psi$  = angle making with horizontal, while signal departing from transmitter,

$R_{in}$  = reflection coefficient of  $n^{th}$  - hop reflection point at ionosphere,

$F_{in}$  = focusing factor of  $n^{th}$  - hop reflection point at ionosphere,

$R_{gn}$  = focusing factor of  $n^{th}$  - hop reflection point at ground,

$D_{in}$  = divergence factor of  $n^{th}$  - hop reflection point at ground,

$L_n$  = total geometrical path length of  $n$  - hop sky wave.

The ground reflection coefficient ( $R_g$ ) for vertical polarization is a function of ray frequency  $f$ , elevation angle  $\psi$ , dielectric constant  $\epsilon$  and ground conductivity ( $\sigma$ ). Thus,  $R_g$  is calculated accordingly. Using these theoretical formulae, a computer code has been developed (Pal and Chakrabarti, 2010). Suitable and approximate models for effective reflection height &  $R_{in}$  (for daytime & nighttime both) have been employed in the code to incorporate the terminator related effects. Other parameters are supplied from the literature as inputs.

### Waveguide mode theory

In this propagation theory, the ‘mode’ is defined as the propagation form of waves which is characterised by a particular field pattern in the plain transverse to the direction of propagation. The field pattern is independent of the position along the axis of a waveguide (Davies, 1990). Basic development of the subject has been done by Budden (1961), Wait (1970, 1986) and others. The vertical electric field strength between the ground and the ionosphere is given by the sum of the waveguide modes as (Lynn, 2010),

$$E(d) = \frac{k}{\sqrt{a \sin d/a}} \sum_{n=1}^N G_n \Lambda_n \exp[-\alpha_n d + j[\varphi_n + \frac{2\pi f d}{c}(1 - \frac{c}{V_n})]], \quad (1-3)$$

where,

$k$  - transmitter power factor,

$\Lambda_n$  - magnitude of  $n^{\text{th}}$  mode excitation factor,

$\alpha_n$  -  $n^{\text{th}}$  mode attenuation rate,

$\varphi_n$  -  $n^{\text{th}}$  mode phase excitation factor,

$V_n$  -  $n^{\text{th}}$  mode phase velocity,

$f$  - frequency of transmitter,

$d$  - path length,

$c$  - speed of light,

$a$  - earth radius.

For long distance propagation, the ionosphere acts like a magnetic conductor. The resonance condition is,

$$2hC_n = (n - \frac{1}{2})\lambda, \quad (1-4)$$

where,  $C_n = \frac{n\lambda}{2h}$ . The waves are polarised with their electric field in the vertical plane of propagation and their magnetic fields being transverse to the plane of propagation. This modes are called the transverse magnetic (TM) modes. The minimum cut-off frequency, below which the wave would not propagate is,  $f_n = \frac{nc}{2h}$ .

This waveguide mode theory is used in LWPC calculation described below.

### 1.5.3 Long-Wavelength Propagation Capability Code

Long-Wavelength Propagation Capability code (LWPC) is a collection of separate and self-complete programs, which is used to simulate the VLF signal propagation characteristics. This has been developed by Space and Naval Warfare System centre, San Diego (Ferguson, 1998). Subroutines of LWPC are developed using FORTRAN and in few cases, C-language. The LWPC integrates the vertical radio fields at the waveguide boundary using mode conversion model (Ferguson and Snyder, 1980). Using LWPC spacial maps, VLF signal availability can be generated, because it can simulate VLF signal profile along a path from a VLF transmitter to a receiver in the world.

Default propagation model of LWPC is Long Wave Propagation Model (LWPM). LWPC considers the space between earth-surface and lower boundary of ionosphere as a waveguide. LWPM employs an exponentially increasing conductivity with height model of lower ionosphere. This simplified exponential ionospheric model is defined by two vital parameters, namely, log-linear slope ( $\beta$ ) and the effective

reflection height ( $h'$ ). This model was derived from the theoretical analysis and measurements done by Ferguson (1992), Morfitt (1977) and Wait & Spies (1964). In LWPC, the propagation paths are divided into horizontally homogeneous segments of adjustable lengths to accommodate different ground conductivity and geomagnetic field values at different points.

Apart from LWPM, the LWPC uses other recognized models, namely, HOMOGENEOUS, CHI, RANGE and GRID. Basically, these models allow users to override LWPM model and to accommodate several perturbation effects of lower ionosphere. The HOMOGENEOUS model considers uniform ionosphere over all paths. In the RANGE model, one can put different ionospheric parameters at different points on path. The GRID treats ionosphere along geographic grids. The CHI is capable of incorporating solar zenith angle ( $Z$ ) effects. The specific inputs can be fed to those models with the help of substrings. First of them is called EXPONENTIAL, where model parameters  $h'$  and  $\beta$  can be supplied. In the second substring TABLE, the direct values can be supplied in tabular form.

The field strengths are plotted as functions of distance using LWFLOT routine. Different control strings of it are used under different circumstances. Among them, we frequently use BEARING control string to incorporate all possible bearing angles and to simulate VLF signal profile over Indian subcontinent for VTX (see Section 3.4.1). While calculating the enhanced D-region electron density ( $N_e$ ) during solar flares we use the RANGE model and EXPONENTIAL substring. Subsequently, the  $h'$  and  $\beta$  corresponding to observed signal perturbations are obtained (see Sections 4.3.3 and 6.2.1). For 3-step modeling of observed VLF amplitude behaviour during flares, in the final step in LWPC, we used HORIZONTAL TABULAR string (see Section 5.2.3).

## 1.6 Investigation of the D-region perturbed by flares

### 1.6.1 VLF monitoring of solar flares

For the VLF amplitude measurement, we record the electric field component of NWC/19.8kHz transmitter signal in the units of dB above  $1\mu\text{V m}^{-1}$  and with 1s resolution. Besides, the VLF signal amplitude and phase from VTX, JJI and other transmitters are also recorded. During a solar flare, all VLF data is compared with solar X-ray data taken in the range, 0.1 – 0.8 nm ( $\phi$  in  $\text{W m}^{-1}$ ) from GOES-15. The recording period of data used in this thesis belongs to the rising phase of Solar Cycle no. 24. Similar VLF responses were reported by Thomson and Clilverd (2001) for

NLK/24.8 kHz to Dunedin, New Zealand path. For NWC-IERC propagation path which is transequatorial in nature (see Fig. 1.7), we detected hundreds of flares during this period. In Fig. 1.6, we present a typical diurnal variation of 19.8 kHz

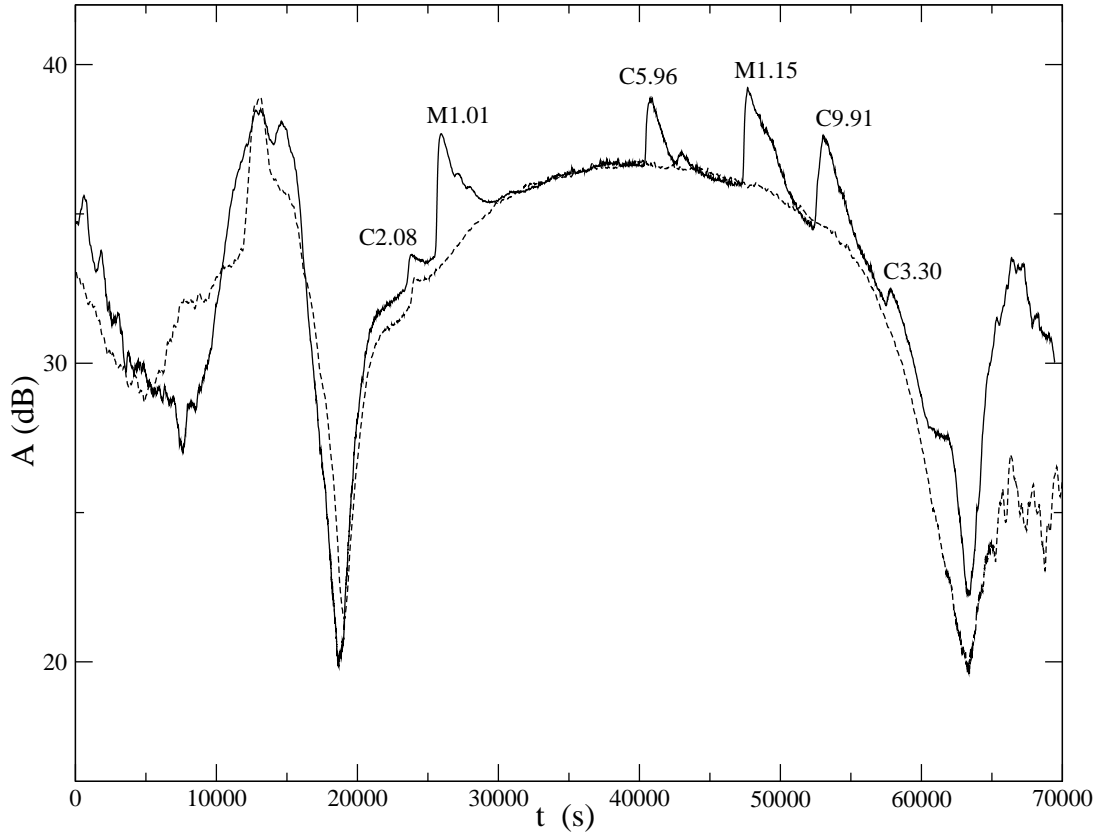


Figure 1.6: The amplitude  $A$  (left) and phase (right) of VLF signals transmitted from NWC (19.8 kHz), as a function of time as recorded at IERC(ICSP), Sitapur ( $22^{\circ} 27'N$ ,  $87^{\circ} 45'E$ ) on 16th Feb (solid line) and 12th Feb (dotted line) 2011. Six solar flares of different classes (C2.08 at 06:37 hrs, M1.01 at 07:11 hrs, C5.96 at 11:19 hrs, M1.15 at 13:14 hrs, C9.91 at 14:43 hrs and C3.3 at 16:04 hrs) were recorded on 16th Feb 2011. All times are in IST(=UT+5.5 hrs) (Basak and Chakrabarti, 2013a).

VLF signal, recorded on 16th Feb 2011 (a solar-active day with several solar flares at different times) and on 12th Feb 2011 (a solar-quiet day). A total of six solar flares of different classes are detected on the 16th Feb 2011. The sharp rise and the slow decay pattern of a typical X-ray irradiance is exhibited by the VLF signal amplitude. Also in Fig. 4.2 of Section 4.1, we present a few examples of typical

VLF amplitude response for X, M and C class flares recorded by our receiver. These are superposed on the X-ray light curve (details of those flares are marked in the Figure).

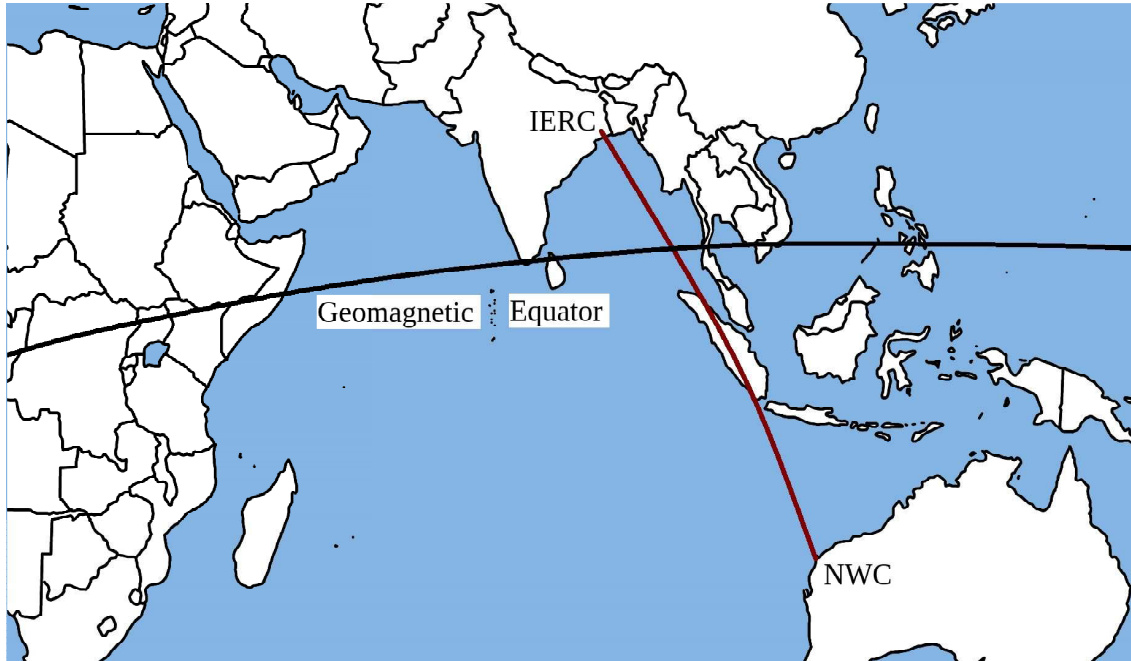


Figure 1.7: The Great Circular Path (GCP) of VLF signal propagation from NWC to IERC transmitter is shown (maroon line). The geomagnetic equator (black thicker line) is also drawn to show the transequatorial nature of the mentioned path. The path is also mixed type as it passes over both the land and the sea (Figure adopted from [www.turkey-visit.com](http://www.turkey-visit.com)).

### 1.6.2 Estimation of D-region parameters using VLF

The investigation of ionospheric parameters are possible by indirect method using VLF as a tool. Details are stated in Section 1.5.1. The VLF amplitude and phase get modified with the flare-time changes of lower ionosphere. The connecting bridges between the ionospheric properties and VLF characteristics are the propagation theories, namely, the wavehop theory and the waveguide mode theory (see Section 1.5.2). The ray model of wavehop theory is best applicable for shorter paths (e.g. VTX transmitter to IERC/ICSP) (Pal and Chakrabarti, 2010) and waveguide mode theory is essential for longer VLF paths. In this case, VLF signal strength is

calculated by summing the contribution from total modes present (Eq. 1-3). As, we analyse the NWC-IERC (distance  $\sim 5691$  km) data, we considered the mode theory approach for our calculations (Basak and Chakrabarti, 2013a, b; Palit, Basak et al. 2013). The LWPC code is developed by following the basic assumptions of mode theory (Section 1.5.3). Supplying VLF amplitude and phase perturbation method within LWPC, we simulate the flare-time enhanced electron densities ( $N_e$ ) (Section 4.3.3 and Section 6.2.1). We develop a theoretical model of effective recombination coefficient ( $\alpha_{eff}$ ) in terms of  $N_e$  and hence use LWPC generated model  $N_e$  values (Section 4.3.2 and Section 4.3.4). We follow this LWPC simulation method and used it to evaluate a different parameter called  $\lambda$ -parameter also, which measures the negative ion content (Chap. 6). In this case, we solved the electron continuity equation (Section 6.2.2 and Section 6.3).

In another approach, we calculate the D-region time delay ( $\Delta t$ ) experienced by VLF signal (Section 4.1). This time delay directly corresponds to the chemical reaction time-scales and their evolutions during flares. Through rigorous analysis of the data, we establish a correlation of it with the solar zenith angle variation as well as the peak X-ray strength of the flare. Physically, the decomposition of complex hydrated ions to simpler ions can be explained from it (Section 4.4).

## Chapter 2

# EARLIER WORKS ON SOLAR RADIATION EFFECTS ON LOWER IONOSPHERE

## 2.1 Solar radiation and D-region of the ionosphere

There are several works in the literature on the changes in VLF signal amplitude and phase. Some studies on the time delay have been carried out for studying the evolution of the D-region due to solar flares. Earlier theoretical works on ionospheric changes were done by Wait (1962), Wait and Spies (1964), Mitra (1974) etc. Thomson and Clilverd (2001) and Thomson et al. (2005) probed the changes of the D-region during flares through the VLF amplitude analysis.

## 2.2 Perturbation of the D-region by Solar flares

### 2.2.1 Recombination processes during flares

In the early years, the basic studies on the recombination of electrons and ions in lower ionosphere (mainly D-region) were made by Appleton (1953), Mitra (1953), Mitra (1974) etc. Subsequently, in a series of works, with the ionospheric data obtained from rocket measurements and other field experiments, and using the electron continuity theory, the dissociative recombination coefficient ( $\alpha_D$ ), mutual ionic recombination coefficient ( $\alpha_i$ ), electron to negative ion ratio ( $\lambda$ ) etc. were estimated and modelled (Whitten and Poppoff, 1961-62; Poppoff and Whitten, 1962). Mitra (1963) reported different methods to estimate recombination coefficients including the height profile at different ionospheric conditions, e.g., diurnal asymmetry method, eclipse method and solar decay curve method. Values of  $\alpha_i$  and  $\alpha_D$  obtained by the above mentioned methods agree with the experimental results. Whitten et

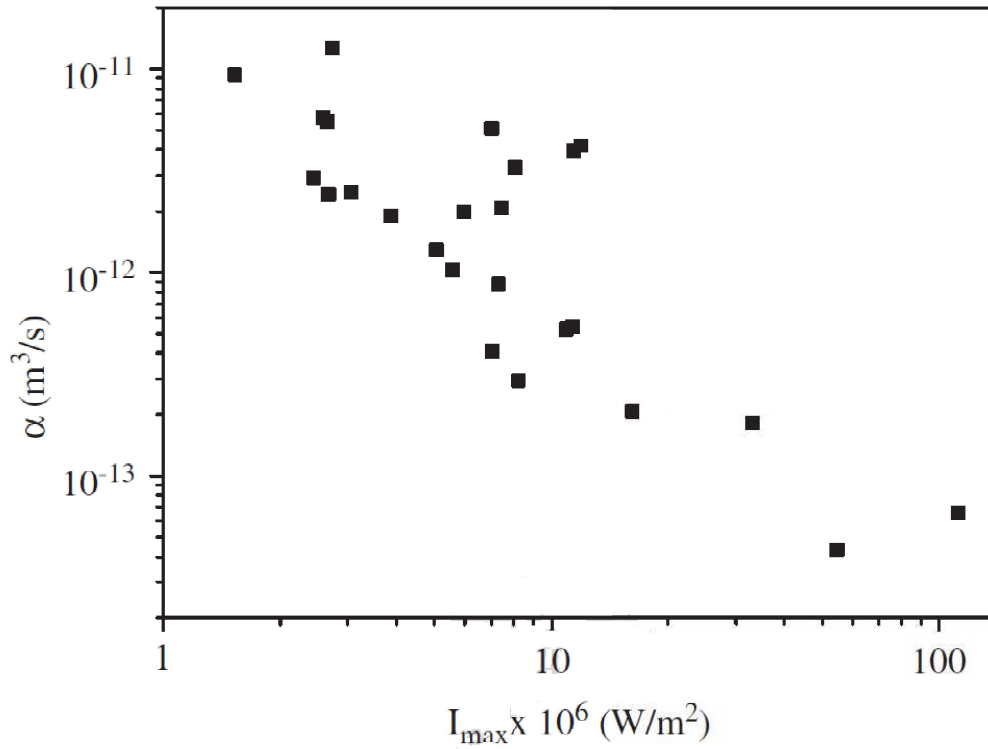


Figure 2.1: The effective recombination coefficient is plotted as the function of peak flare flux at 74.1 km height for 25 Flare induced Amplitude Enhancement (FAE) events, as calculated by Zigman et al. (2007).

al. (1965), Parthasarathy and Rai (1965) and Gledhill (1986) developed theoretical methods for empirical expressions for  $\alpha_{eff}$  (it includes  $\alpha_i$ ,  $\alpha_D$ ,  $\lambda$  and other dust capture coefficients of aerosol theory). Wagner and Thome (1972) proposed a different method, namely, ‘Thomson Scatter Experimental Technique’ to simulate electron density and  $\alpha_{eff}$  during solar flares, relative to pre-flare condition at E-region. According to Appleton (1953), the  $N_e$  and  $\alpha_{eff}$  are directly related to time delay  $\Delta t$ . This  $\Delta t$  appears due to ‘inertial’ properties and chemical reaction time scales of the D-region ionosphere. This  $\Delta t$  is nearly similar to the *sluggishness* (Appleton, 1953; Valnicek, 1972) and *relaxation time* (Mitra, 1974). Balchandra Swamy (1991) analysed photo-ionization rates in detail for different ion constituents ( $\text{NO}^+$ ,  $\text{O}_2^+$ ) and for different solar X-ray bands. Hence, assuming photo-chemical equilibrium, he computed the height profile of  $\alpha_{eff}$  for different M and X classes of flares. In the last few years, the calculation of the recombination coefficients during different types

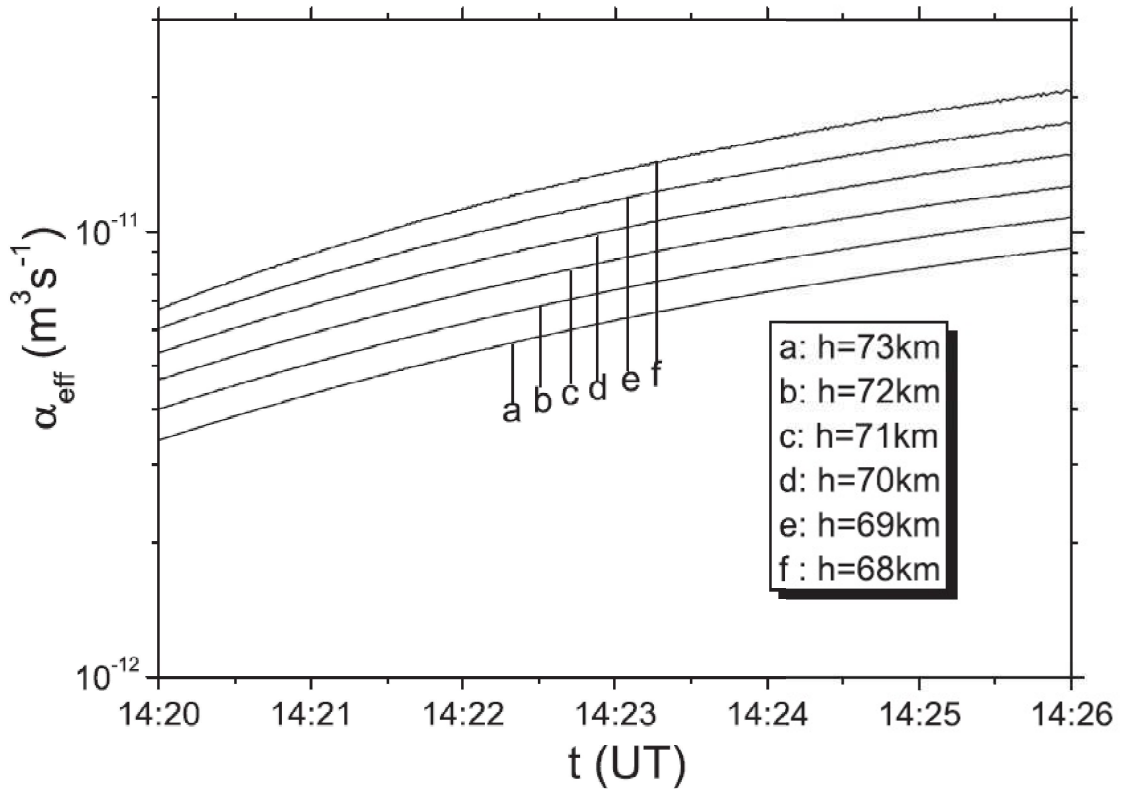


Figure 2.2: The effective recombination coefficient in several heights of D-region ionosphere at the relaxation regime of the M1-class solar flare occurred on 18th Feb, 2011 (Nina et al, 2012).

of solar and geomagnetic events have been done. Pozo et al. (1997) estimated  $\alpha_{eff}$  for nighttime auroral ionosphere using EISCAT radar data and showed clearly that,  $\alpha_{eff}$  is greatly decreased with the increase in particle precipitation flux at higher energy. The same EISCAT radar observation was used by Osepian et al. (2009) to model  $\alpha_{eff}$  during solar proton events. To compare experimental measurements of  $\alpha_{eff}$  with theoretical counterparts, Friedrich et al. (2004) inserted temperature and pressure of lower ionosphere in  $\alpha_{eff}$  expression empirically. Using two different approaches of D-region electron continuity theory, workers such as Zigman et al. (2007) calculated  $\alpha_{eff}$  during the flare peak (Fig. 2.1) and Nina et al. (2011) during the decay regime of a flare (Fig. 2.2).

## 2.2.2 D-region chemical models

D-region chemistry is complex. Detail modelling of so many positive and negative ions as well as hydrated cluster ions and several reactions taking place among them is difficult. Many workers chose the most chemically abundant ions and the most frequent chemical reactions in presence of high energy radiations. They developed chemical models accordingly. These will be discussed in this Section.

*6ion+electron chemical model:* To deal with the D-region chemistry at lower heights ( $\sim 70$  km), Mitra and Rowe (1972) proposed a 6-ion + electron simplified model, where the ions are  $O_2^-$ ,  $NO^+$ ,  $O_2^+$ ,  $O_4^+$ ,  $H^+(H_2O)_n$  and  $NO_3^-(H_2O)_n$ . After studying all the reaction channels, Mitra and Rowe (1972) reported that, at lower heights, the variation of positive and hydrated ions are less even due to strong flare induced ionization. In the D-region above 74-75 kms, the negative ions are practically absent. There, the main ion contents are  $NO^+$  and  $H_2O_5^+$ . At 75 to 80 km height, the generation of  $O_2^+$  is less than  $NO^+$  under quiet and flare X-ray conditions (Mitra and Rowe, 1974). So, the main clustering is formed with  $NO^+$  through,  $NO^+ \rightarrow NO^+ \cdot CO_2 \rightarrow H^+(H_2O)_3$  (Mitra and Rowe, 1972). Clustering of  $O_2^+$  and  $O_4^+$  are possible only during direct photo-ionization process under flare conditions. But a large fraction of hydrates are lost, as they go back to  $O_2^+$  and  $NO_2^+$ . Thus, under flare conditions  $[H_2O]$  and  $[O]$  vary, and as ionization rates go up, the percentages of hydrate ion go down with  $\alpha_{eff}$ .

*GPI model:* Another simplified model is Glukhov-Pasco-Inan (GPI) chemical model (Glukhov et al. 1992). Here, three types of ion species are taken, namely,  $N^+$ ,  $N^-$ ,  $N_x^+$  and  $N_e$ . Though this model is a simplified one, for evolution of D-region at 65 km to 70 km heights, this works very well. Lehtinen and Inan (2007) used this for even at an atmospheric height of 50 km, as they included  $N_x^-$  ions also to the model. More description of this model is presented in Section 5.2.2.

*SIC model:* Sodankyla Ion Chemistry (SIC) model was developed as the alternative steady state model to handle D-region chemistry. Considering chemical equilibrium, it calculates the electron concentrations ( $N_e$ ) for D and E-regions ( $\sim 70$  km to 100 km). It was developed by Turunen et al. (1992).  $N_2$ ,  $O_2$ ,  $O$ ,  $NO$  and  $O_2(^1\Delta_g)$  are the affected neutral ions due to solar and extragalactic radiations. These were incorporated in this model. The neutral atmosphere in this model is supplied by semi-empirical model, MSIS-90 (Hedin, 1991). The main ionization sources are

photoionization and galactic cosmic rays. Chemical transportation processes are generally neglected. This model is first used by Burns et al, (1991) and Turunen (1993).

Apart from these, there are many other models in the literature, namely, (a) Low latitude ionosphere-plasmasphere model, (b) Global theoretical ionospheric model, (c) Coupled thermosphere-ionosphere model, (d) Mid-latitude ionospheric model and so on (Schunk, 1996).

### 2.3 Ionospheric time delay during flares

In a review, Tsurutani et al. (2009) discussed long term effects on the ionosphere by solar flares, followed by Fast Interplanetary Coronal Mass Ejections (ICMEs). Qian et al. (2011) showed the dependency of Total Electron Content (TEC) of ionosphere on the solar zenith angle. Le et al. (2007, 2012), Zhang et al. (2011) and others reported that, flare induced TEC decreases when zenith angle increases. All these works discuss the effects of solar zenithal angle on the upper and middle ionosphere.

Mitra (1974) established a relation of  $\tau$  with the maximum electron density ( $N_{e,max}$ ). Mitra (1974) showed that, during a given solar flare, the ' $\tau$ ' is inversely related with  $N_{e,max}$ , i.e., during stronger flares, the ionospheric response is more instantaneous. A similar result was reported by Valnicsek and Ranzinger (1972). Using the X-ray data obtained by Inter-cosmos 1 satellite, they showed that the 'sluggishness' ( $\Delta t$ ) decreases when the solar induced ionizing activity increases and vice versa. Zigman et al. (2007) calculated the time variation of  $N_e$  for several classes of flares using 'electron continuity theory' and  $\Delta t$  as crucial parameters (where, VLF signal along NAA/24.0 kHz to Belgrade propagation baseline are used for analysis). Thomson and Clilverd (2001) studied both long (NLK/24.85 kHz to Dunedin, 12.3 Mm) and short (French  $T_x$ /18.3 kHz to Cambridge, 617 km) path VLF propagation. They showed that for VLF amplitude perturbation due to wide variation of  $Z$  for a long path, the net  $Z$ -effect is less and conversely,  $Z$ -effect is significant for shorter paths. In Fig. 2.3, we see that flares corresponding to open circles nearly follow the mean curve, instead of having higher  $Z$  values. But in Fig. 2.4, most of the flare amplitude responses denoted by open diamonds (with higher  $Z$ ) are significantly away from the mean curve. Grubor et al. (2005) monitored the VLF response during flares for a shorter path (GQD/22.1 kHz to Belgrade  $\sim$  2000 km) and they showed that, the  $Z$ -effect on amplitude and phase delay are not prominent enough, but the flares occurred at higher zenith angle (i.e., during dusk

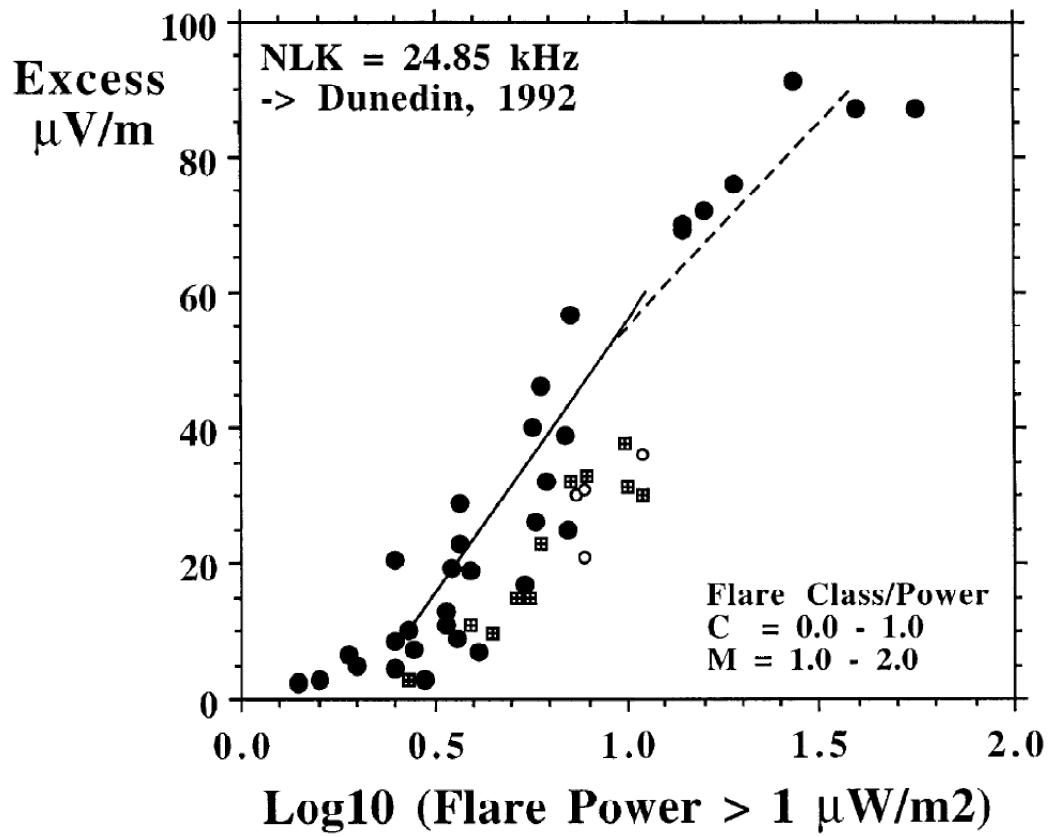


Figure 2.3: The excess VLF amplitude is plotted as a function of corresponding X-ray intensity. The data recorded at Dunedin, NZ for NLK/24.8 kHz signal located at Settle. The propagation path length is 12300 km. For the flares corresponding to black dots, squares and open circles successively, the respective average solar zenith angle over the propagation path increases (Thomson and Clilverd, 2001).

and dawn) can cause amplitude and phase delay, if they are strong enough.

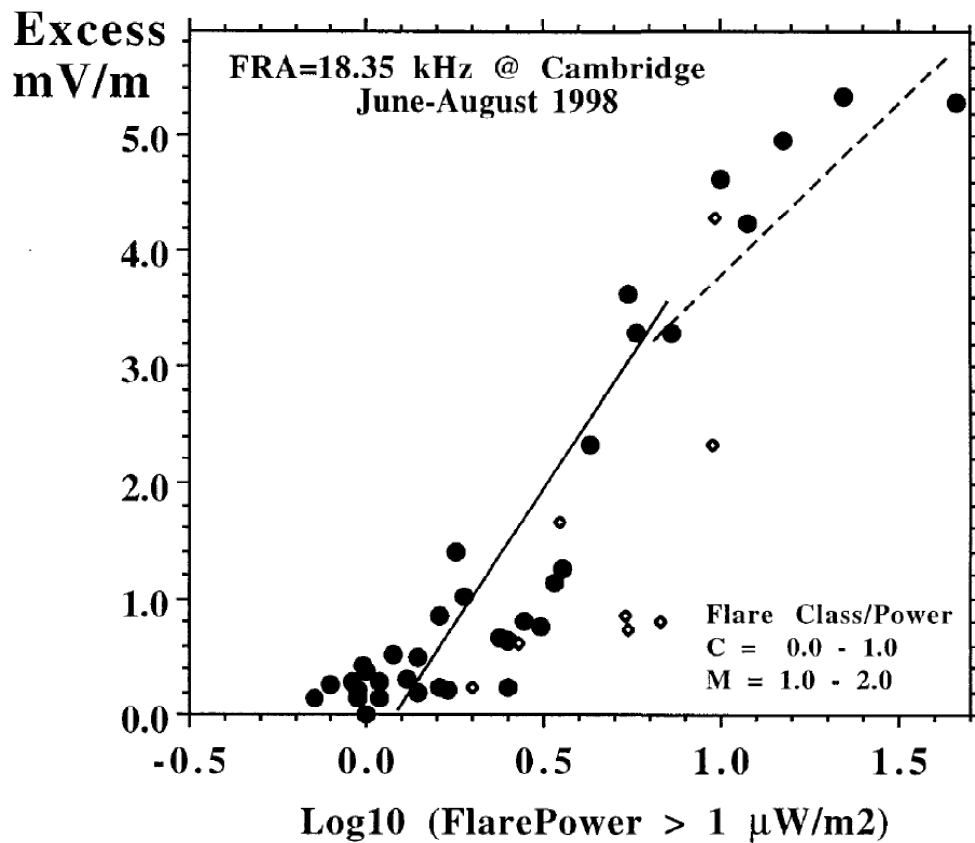


Figure 2.4: The same observables are plotted as Fig. 2.3 but this data is emitted from French transmitter/18.3 kHz and recorded at Cambridge, UK. This path length is only 617 km and zenith angle variation over path is negligible. The flares indicated by black dots have zenith angle  $<60^\circ$  and it is within  $60^\circ$  and  $75^\circ$  for those with open diamonds (Thomson and Clilverd, 2001).

## Chapter 3

# DIURNAL VARIATION OF VLF SIGNAL OBTAINED THROUGH ALL INDIA CAMPAIGNS

A Very Low Frequency signal, generated from a transmitter, propagates worldwide through earth-ionosphere waveguide. They are being received by VLF-receiver systems and the data is used for studies of the ionospheric physics through remote sensing method. In this Chapter, we will discuss the diurnal variation in VLF signal in lower ionospheres. We present the VLF amplitude and phase data coming from VLF transmitters spread worldwide. The description and scientific outcomes of ICSP lead VLF campaigns are presented, to demonstrate the dependence of nature of signal on propagation path characteristics. We have carried out LWPC simulation to reproduce spatial profile of VLF signal over the Indian subcontinent, which qualitatively supports the overall observation of the VLF campaign.

### 3.1 VLF transmitters and receivers

#### 3.1.1 VLF transmitters

There are several VLF transmitters working worldwide, namely, VTX1/16.3 kHz, VTX2/17 kHz, VTX3/18.2 kHz and VTX4/19.2 kHz at Vijayanarayanan, India, NWC/19.8 kHz at North-West Cape, Australia, JJY/40 kHz, JJI2/19.1 kHz at Japan, DHO/23.4 kHz at Germany, NLK/24.8 kHz and OMEGA -transmitters at USA etc (see Fig. 3.1). We regularly monitor VTX3/18.2 kHz ( $8^{\circ}26'N, 77^{\circ}44'E$ ) due to its proximity from our receiver sites and its unique geographic location for ionospheric study over Indian subcontinent. We constantly record VLF signal from NWC/19.8 kHz ( $21^{\circ}48'S, 114^{\circ}9'E$ ) (see, Fig. 3.1) also due to its phase stable nature

and special signal propagation path, which is medium length (5668 km) and transequatorial (see Fig. 1.7). We monitor DHO/23.4 kHz, JJI/22.2 kHz occasionally also to do comparative studies of several propagation path effects.

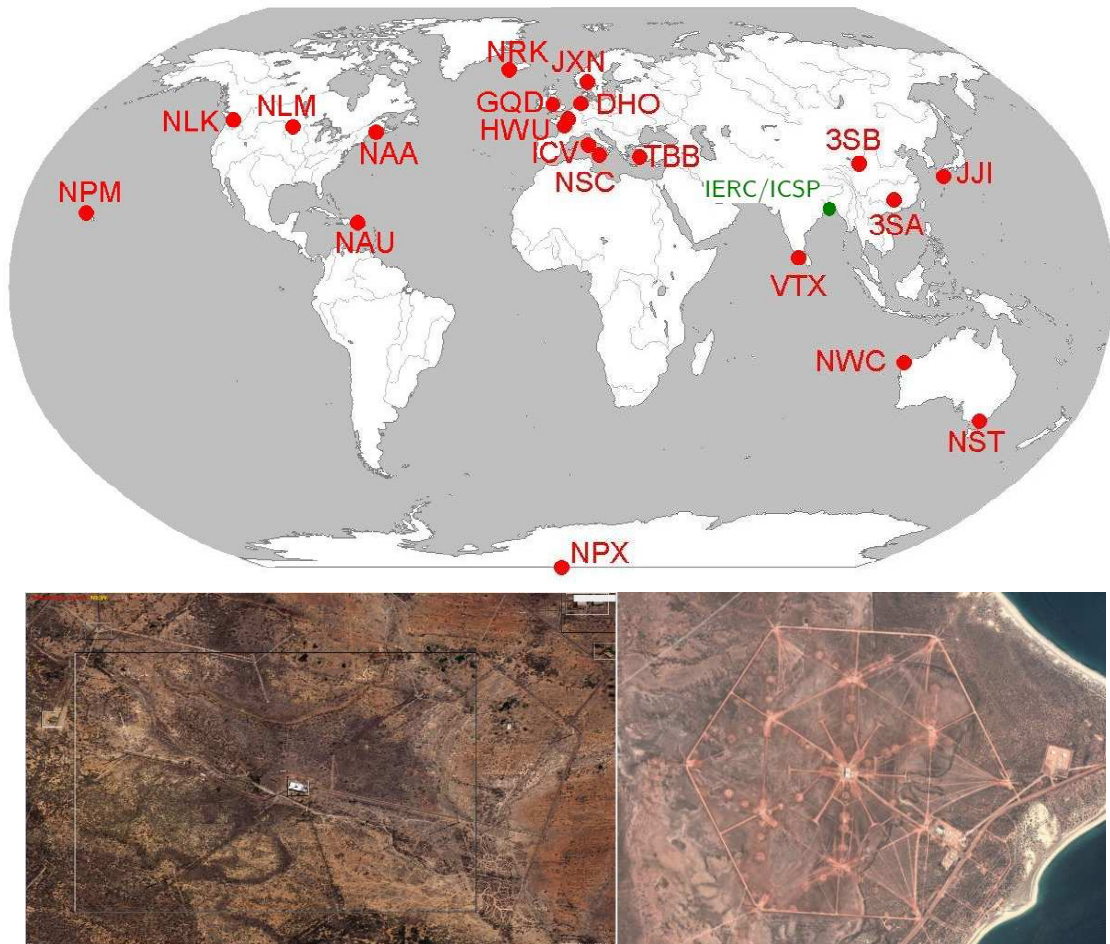


Figure 3.1: In the Figure above, the locations of the VLF transmitters mentioned in Section 3.1.1 and several others are indicated on a world map (red circle). Also, the IERC/ICSP VLF receiving station is indicated (green circle). (Figure adopted from [www.nova.stanford.edu](http://www.nova.stanford.edu).) In the Figure below, images of VLF transmitter VTX (left) at Vijayanaranam ( $8^{\circ}26'N, 77^{\circ}44'E$ ), India and NWC (right) at North-West Cape ( $21^{\circ}48'S, 114^{\circ}9'E$ ), Australia (Figure taken from <https://maps.google.co.in>).

### 3.1.2 VLF receivers and receiving stations

We monitor both narrowband and broadband data from several VLF transmitters for analysis of ionosphere. One of the mostly used receivers is the SoftPAL VLF receiver. It records the electric field component of a VLF signal in units of dB above  $1\mu\text{V m}^{-1}$  and with 1 s resolution. It is basically a full software version of AbsPAL (Absolute Phase and Amplitude Logger), - developed by the Radio and Space Physics Group of Otago University, New Zealand. It is capable of recording amplitude and phase informations from multiple VLF transmitters simultaneously. A GPS unit is attached to the system for putting the time stamp on the data. The data is directly stored in a computer which can be viewed using the Lab-Chart software. This system is installed at Ionospheric and Earthquake Research Centre (IERC) of Indian Centre for Space Physics (ICSP), at Sitapur ( $22^\circ 27'\text{N}$ ,  $87^\circ 45'\text{E}$ ), West Bengal, India. This institute is located at a radio quiet place, where the signal to noise ratio is high.

We also use Gyrator-III type VLF receiving system, which is fully developed by ICSP, Kolkata. This system consists of a square loop antenna of 3.5 ft on each side. It uses an analogue band pass filter of 5 – 30 kHz range. By setting suitable amplification level, which is adjustable, it can record a single frequency at a time. But using digitised filtering technique, multiple frequencies can be recorded simultaneously. This system is also permanently installed at IERC/ICSP, Sitapur, ICSP, Kolkata ( $22^\circ 27'\text{N}$ ,  $88^\circ 23'\text{E}$ ) and at some other stations, such as Malda, and Coochbehar.

SuperSID VLF receiving system is developed by Stanford University VLF Group. It consists of an antenna, pre-amplifier and the data is transferred to a computer through a sound card. Due to the VLF electromagnetic wave, some voltage is induced at the loop antenna and then it gets amplified by pre-amplifier. It is installed in SNBNCBS, Kolkata ( $22^\circ 34'\text{N}$ ,  $88^\circ 24'\text{E}$ ) and ICSP, Kolkata and good quality data is obtained. All these systems described above, are developed for recording narrowband data. For broadband data, we use the AWESOME VLF receiver, which is developed by Stanford University VLF Group. It records the magnetic field component of VLF signal and by taking Fourier Transform of the recorded data, the spectrogram is obtained. Along with all other systems this is also successfully running at IERC/ICSP, Sitapur and at ICSP, Kolkata ( $22^\circ 27'\text{N}$ ,  $88^\circ 23'\text{E}$ ).

For all the works done in this thesis, we analysed the narrowband NWC/19.8 kHz VLF data, recorded using SoftPAL VLF receiver at IERC/ICSP, Sitapur, West Bengal, India (GCP is shown in Fig. 1.7). For the analysis of the spatial variation

of VLF signal in this Chapter, we simulated the VTX/18.2 kHz data.

### 3.2 Diurnal behaviour of VLF signal from several transmitters

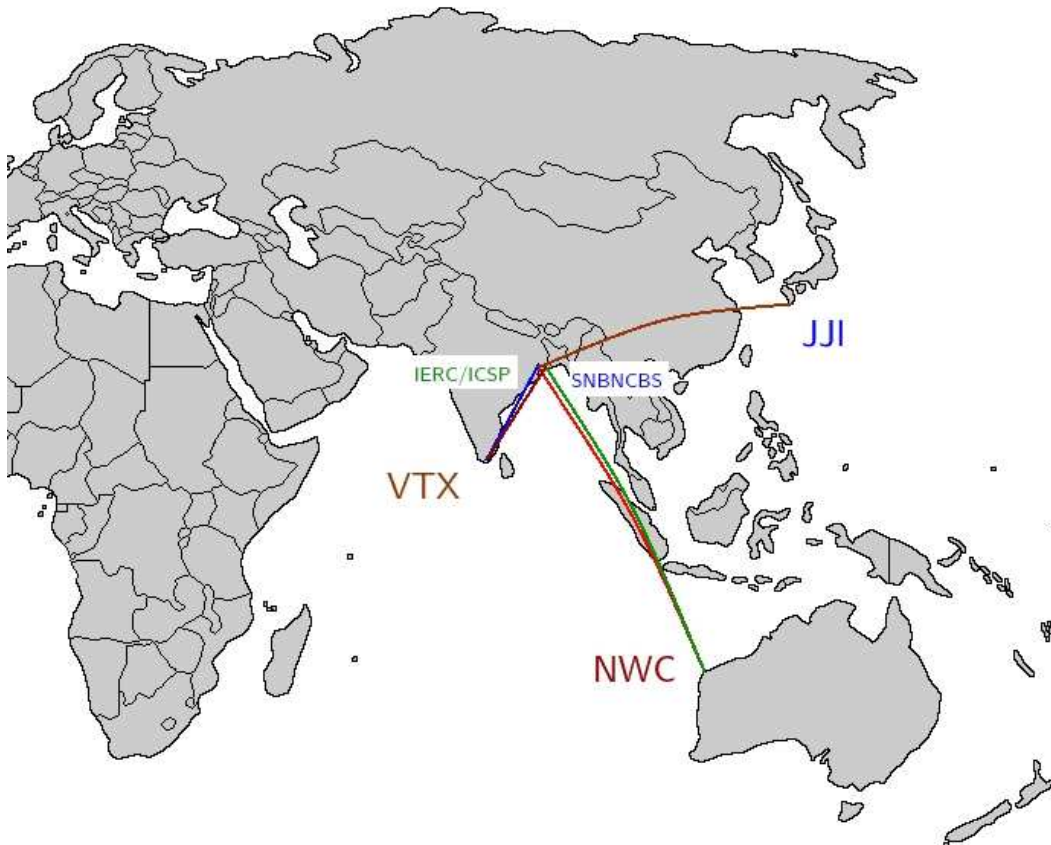


Figure 3.2: The transmitter-receiver VLF propagation Great Circular Paths (GCP) are drawn using coloured lines. The propagation paths are, (i) NWC-IERC (red line), (ii) VTX-IERC (blue line), (iii) JJI-IERC (brown line), (iv) NWC-SNBNCBS (green line), (v) VTX-SNBNCBS (violet line) (Figure adopted from *www.outline-world-map.com*).

In general, monitoring of the changes occurred in the lower ionosphere are carried out by subionospherically propagated VLF signal. Some discussions of it have been done in Sec. 1.5.2. Now, we would present some diurnal amplitude and phase

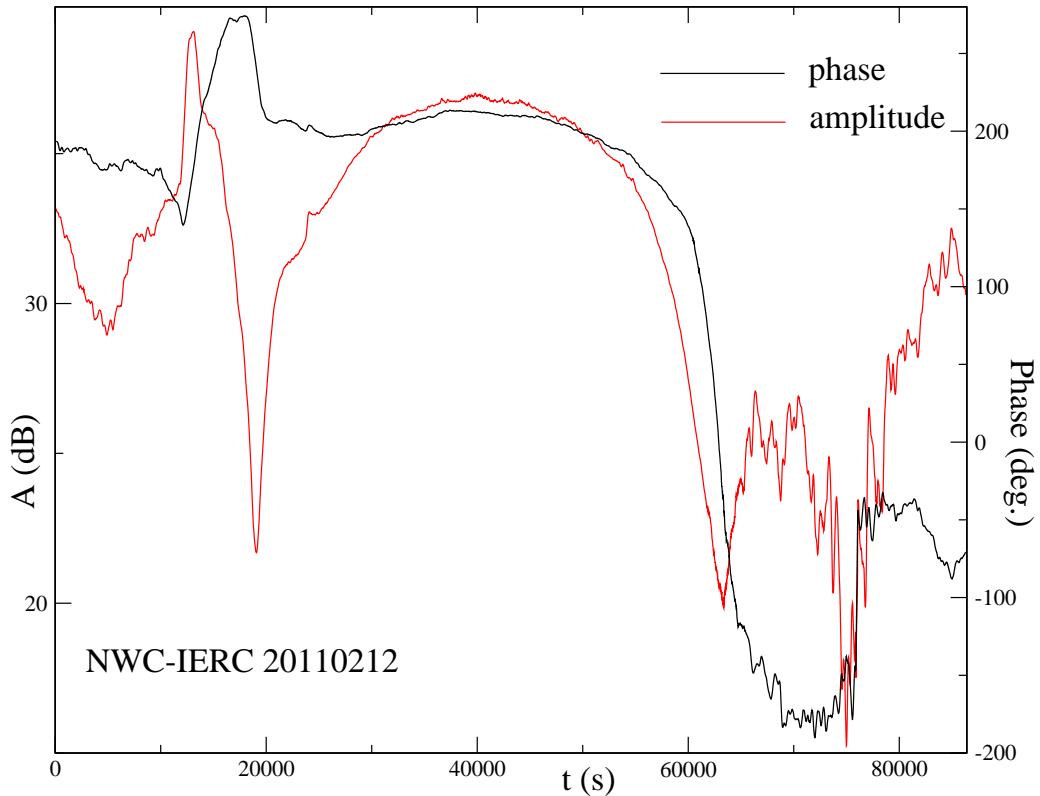


Figure 3.3: The amplitude ( $A$ ) (red line) and phase (black line) of VLF signals transmitted from NWC/19.8 kHz, as a function of time as recorded at IERC/ICSP, Sitapur ( $22^{\circ} 27'N$ ,  $87^{\circ} 45'E$ ) on 12th Feb 2011. All times are in IST (=UT+5.5 hrs) (Basak and Chakrabarti, 2013a).

variation for different  $T_x$ - $R_x$  pair and try to understand the propagation path effects on the signal characteristics. All Great Circular Paths (GCP) are shown in Fig. 3.2. In Fig. 3.3, we plot the amplitude and phase of NWC-VLF signal recorded at IERC/ICSP using SoftPAL receiving system. Daytime signal variation is clean enough and nicely reflects the zenithal variation of the solar flux. The phase stability of NWC/19.8 kHz signal is helpful for deeper analysis of lower ionospheric perturbations. Using the same receiving system, the amplitude informations from VTX/18.2 kHz and JJI/22.2 kHz are also recorded (Figs. 3.4). 23rd Feb 2011 was a solar-quiet day but on 4th Aug 2011 one M9-class solar flare was recorded near the mid-day along with other C-class weak flares.

The diurnal variation of the VLF signal depends on the propagation path and

receiving location also. We installed SuperSID monitor at SNBNCBS, Salt Lake, Kolkata and recorded VLF data from several transmitters. Among them, the data from NWC/19.8 kHz and VTX/18.2 kHz are shown in Figs. 3.5. Though this location is just  $\sim 80$  km away from IERC/ICSP site, the difference in relative signal strength between daytime and nighttime are notable. The interference among several VLF waveguide modes differ for those signal propagation paths and this could be the possible reason for the difference.

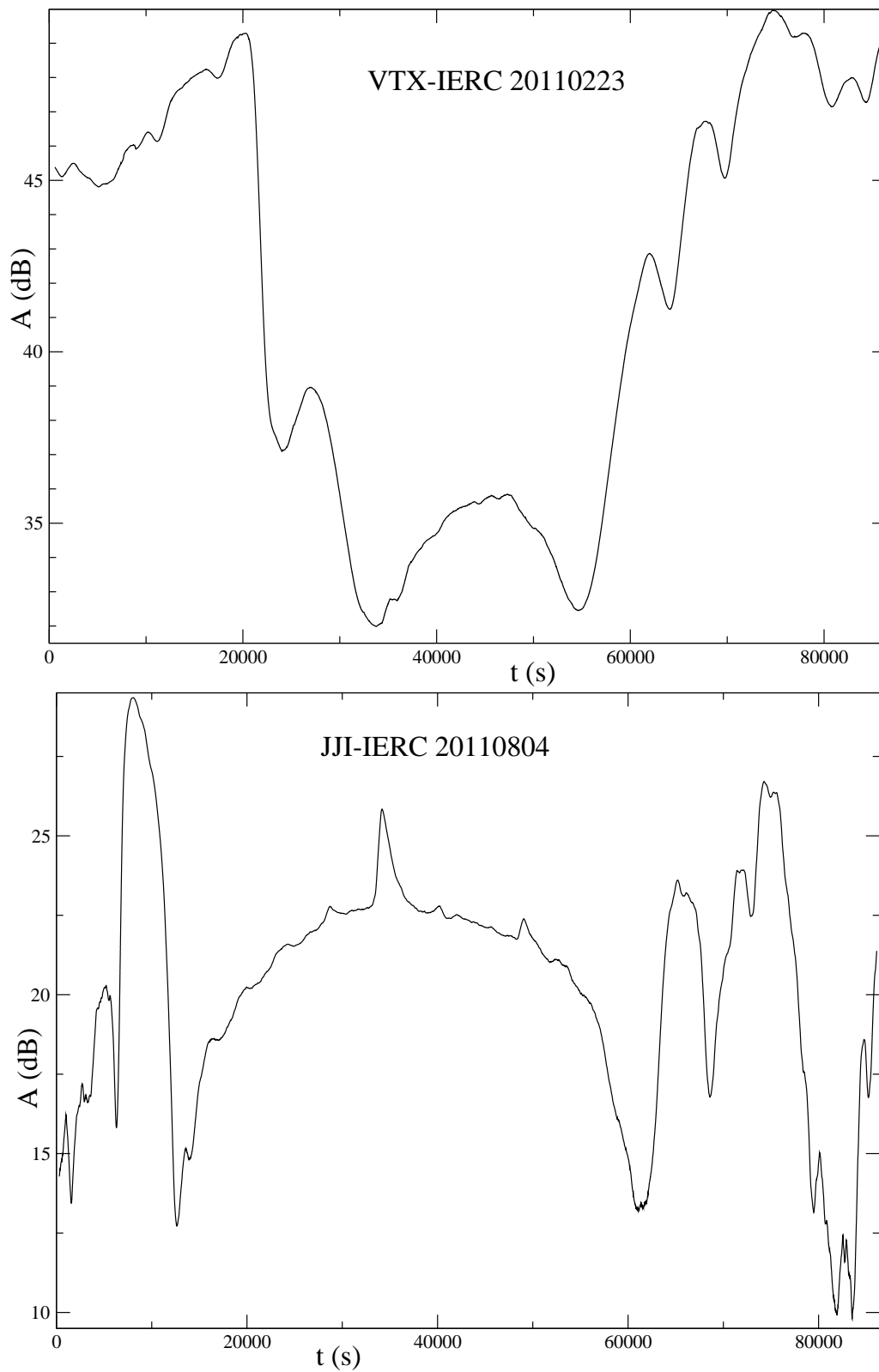


Figure 3.4: The amplitude ( $A$ ) of VLF signals transmitted from VTX/18.2 kHz (above) and JJI/22.2 kHz (below), as functions of time are recorded at IERC/ICSP, Sitapur ( $22^{\circ} 27'N$ ,  $87^{\circ} 45'E$ ) on 23rd Feb and 4th Aug 2011 respectively (see also, Chakrabarti et al. 2012a).

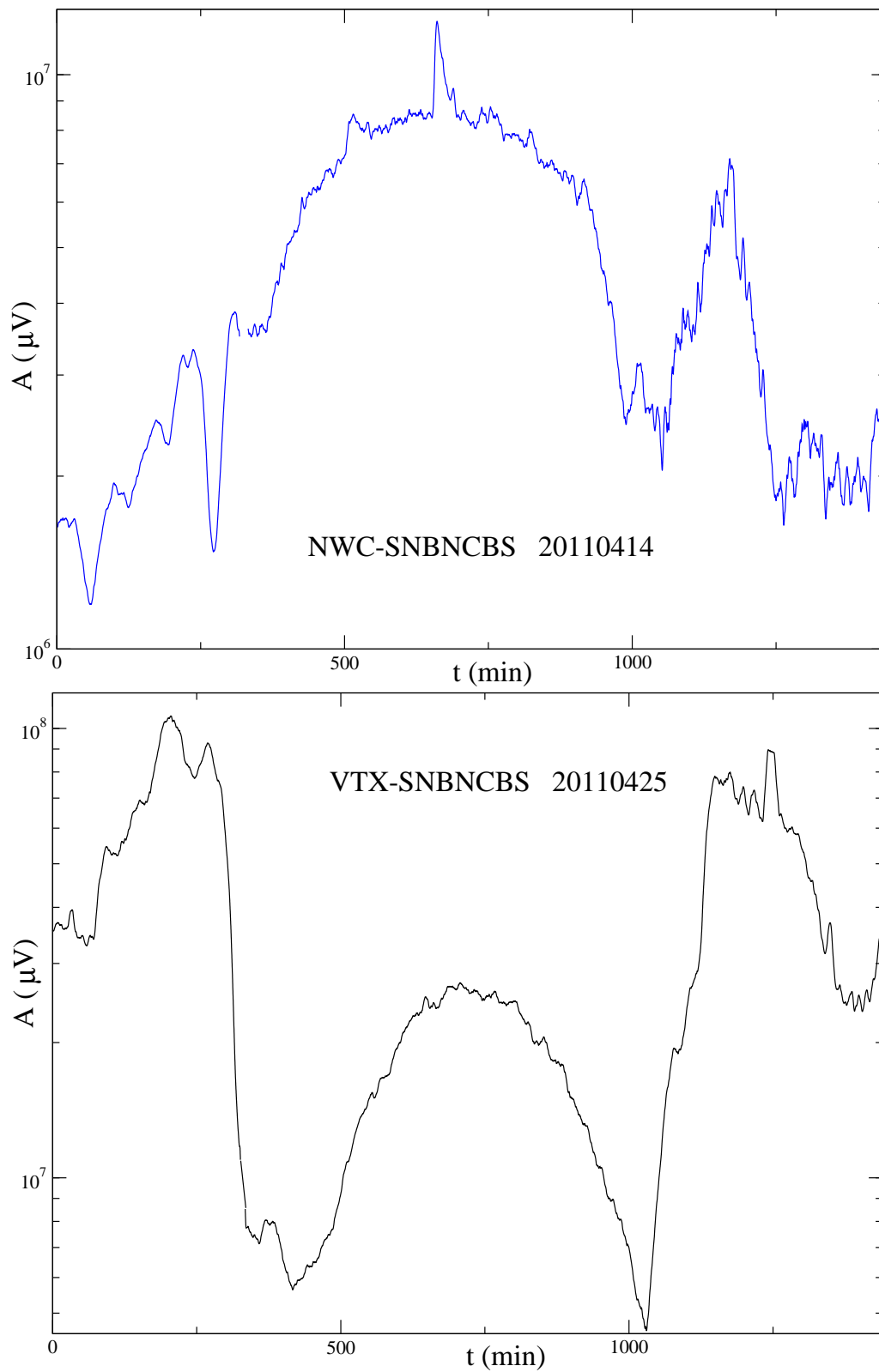


Figure 3.5: The amplitude of the ( $A$ ) VLF signal transmitted from NWC/19.8 kHz (above) and VTX/18.2 kHz (below), as functions of time, are recorded at SNBNCBS, Kolkata ( $22^\circ 34'N$ ,  $88^\circ 24'E$ ) on 4th Apr and 25th Apr 2011 respectively.

### 3.3 Multi-station VLF campaigns

The location of VTX transmitter roughly divides the landmass of the Indian subcontinent into two parts, which makes it an ideal test bed for the theoretical modelling of VLF signal propagation through the Earth Ionosphere Waveguide (EIWG). ICSP, Kolkata has been recording VLF radio signal for about a decade and reported those observations related to Leonid meteor showers (Chakrabarti et al., 2002) and solar flares (Chakrabarti et al., 2003) before. Now, we present the results of the VLF signal amplitude variation which are simultaneously received at over a dozen of locations from all over India and Nepal both in the summer and the winter. All locations are at short VLF path from VTX (less than 3,000 km). Due to the unique location of the VTX transmitter and the geographic position of the Indian sub-continent itself, it was possible to monitor both the east-west and west-east propagation effects at short distances during campaigns (Chakrabarti et al., 2012a, b). All data recorded during campaigns can be explained by two complimentary theories, namely the wavehop theory and waveguide mode theory (discussion has been done on Sec. 1.5.1). Presently, we use LWPC code and show the VLF amplitude variation as the function of propagation path. This procedure roughly reproduces the observed east-west asymmetry (Chakrabarti et al., 2012a).

One of the objectives of these campaigns was to calibrate the actual VLF observations as the function of geographical location. Based on this ground work, the global effects on lower ionosphere due to extraterrestrial and terrestrial seismic activities can be probed (Chakrabarti et al., 2012a).

In the campaigns, the data was received at various stations in the summer and the winter. The winter campaign stations are Imphal (Manipur), Agaratala (Tripura), Salt Lake (WB), Malda (WB), Khukurdaha (WB), Kathmandu (Nepal), Hyderabad (AP), Gwalior (MP), Bengaluru (Karnataka), Pune (Maharashtra), Bhuj (Gujarat), Kashmir (JK), Ahmedabad (Gujarat) and Suri (WB). The summer campaign stations are Coochbehar (WB), Saltlake (WB), Malda (WB), Raigunj (WB), Khukurdaha (WB), Bhagalpur (Bihar), Kathmandu (Nepal), Kangra (HP), Jaipur (Rajasthan), Kashmir (JK), Pune (Maharashtra), Bhuj (Gujarat), Benaras (UP) and Bolpur (WB) (Chakrabarti et al., 2012a, b). Seven stations were common to both the campaigns. The places were distributed in a way that the entire Indian sub-continent may be covered. The geomagnetic equator goes roughly from east to west, and passes within less than a degree north of the VTX transmitter. The 150°E geomagnetic meridian, which passes through the transmitter roughly divides India into two halves (Chakrabarti et al., 2012a). To detect the non-reciprocity of the

east-west propagation effects, we placed the stations on both sides of this central meridian in each of the campaigns as well as in Bangalore, which is just near the skip distance from VTX.

### 3.3.1 VLF campaigns and its significance

#### *Winter campaign*

It was conducted from the 21st to 31st of December, 2008. Station locations have been presented in the earlier Section. Among fourteen stations, ten were in the east and four were in the west of CGM (Chakrabarti et al., 2012a). Depending on the relative signal strength of night w.r.t. daytime, all the observed diurnal patterns are classified into two groups, namely *Eastern*-type and *Western*-type. Nighttime amplitude is stronger for *Eastern* type and vice-versa. In Bangalore data, the daytime solar zenithal variation is absent, as it is ground wave dominated region. Using default propagation model of LWPC, we plot the VLF signal amplitude as function of propagation path during midday and midnight (Chakrabarti et al., 2012a). Simulations are generally in agreement with relative night and daytime signal strength observations i.e. the *Eastern* and *Western* characteristics. LWPC also verifies that Bangalore is a ground wave dominated region (Chakrabarti et al., 2012a).

#### *Summer campaign*

This campaign was conducted from the 20th to 27th of July, 2009. Among fourteen stations, nine were in the east and five were in west of CGM. In Fig. 3.6, we present the received signals of Coochbehar (below) and Kashmir (above). Like the winter campaign, the *Eastern* and *Western* classification is also present here (Chakrabarti et al., 2012a, b). The VLF data at Coochbehar belongs to *Eastern* type. Signal strength at Kashmir is weak and solar zenithal variation is absent. The same LWPC simulation for the receiver locations of Fig. 3.6 are plotted in Fig. 3.7. Just like the observations of winter campaigns, the LWPC can explain the *Eastern* and *Western* nature of this campaign results also (Chakrabarti et al., 2012a, b). However, for a few locations such as Kashmir (Fig. 3.6) the noise level is high and data is not easily explainable.

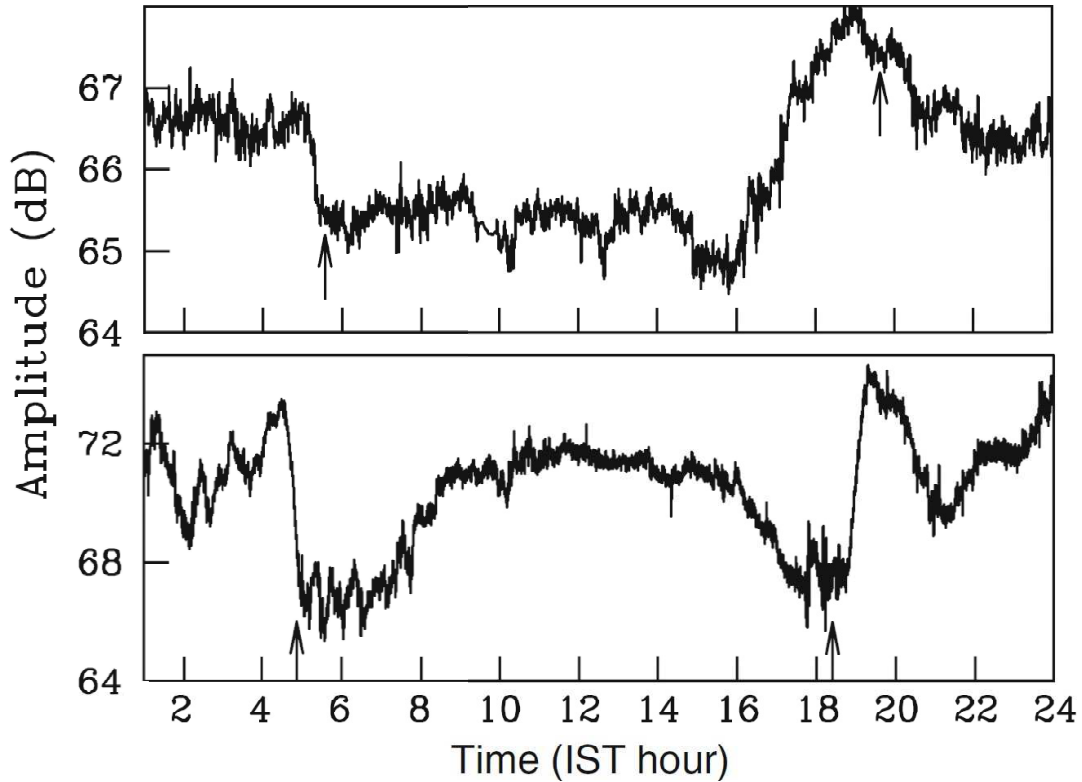


Figure 3.6: The normalised VLF amplitude ( $A$  in dB) diurnal variation data for Kashmir ( $34^{\circ} 08'N$ ,  $74^{\circ} 51'E$ ) (above), JK and Coochbehar ( $26^{\circ} 19'N$ ,  $89^{\circ} 28'E$ ) (below), West Bengal. The data was recorded during the summer and winter VLF campaigns respectively. Sunrise and sunset time at receiving sites are indicated by arrows (Chakrabarti et al., 2012a).

### 3.3.2 Outcome of the VLF campaigns

We observe the data during the VLF campaign with receiving stations spanning the whole of Indian sub- continent including Nepal, a region covering around 4 million sq km. The unique location of the VTX station and the division of Indian sub- continent (geomagnetic meridian passing through VTX) by almost two equal parts makes it an ideal test-bed for the existing theoretical models of propagation through the EIWG. From the data, we could easily distinguish *Eastern* and *Western* type signals (Chakrabarti et al., 2012a). LWPC code can generally reproduce this variation. In majority of the campaign locations, the average amplitude at night and day match with that given by LWPC code. The E (Eastern)-type amplitude varia-

tions are formed when the signal propagates from the west to the east, while the W (Western)-type signals are found to form when the signal propagates from the east to the west. As the magnetic field is included in LWPC, the effect is caused by the switching of the sign of the magnetic field with respect to the propagation direction (Barbar and Crombie, 1959). Thus, evidently the *Eastern* and *Western* types can be correlated with magnetic field direction (Chakrabarti et al., 2012a). The day time data of Bangalore is very weak perhaps because of dominance of the ground wave at that location. The observations during the campaign gave an overall picture of the nature of the VLF data during solar quiet days nationwide (Chakrabarti et al., 2012a). Detecting the deviation from these observations, the detection of ionospheric perturbation due to terrestrial and extraterrestrial sources are possible.

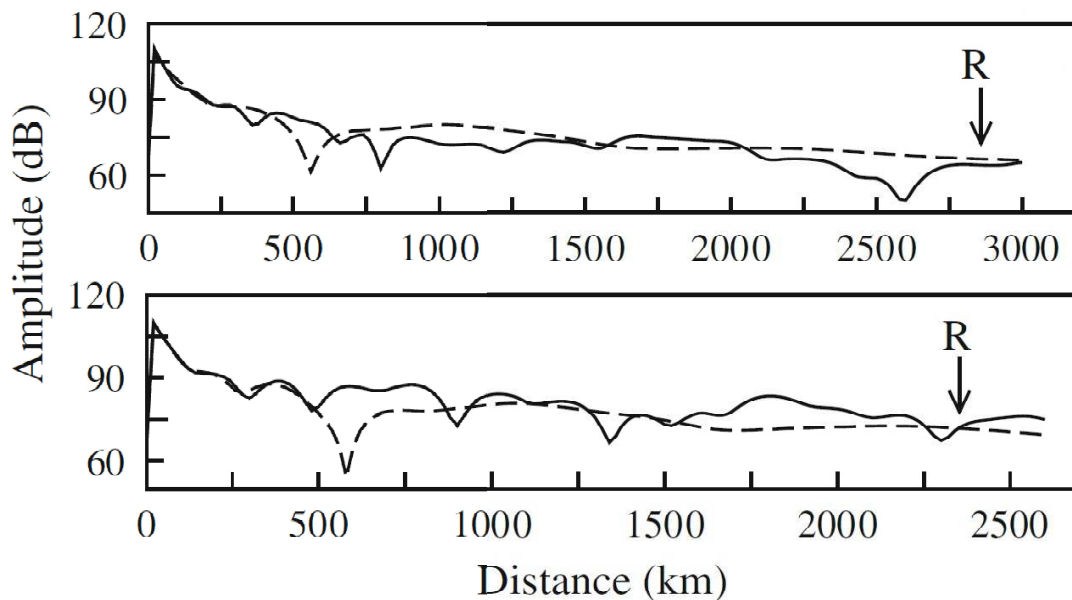


Figure 3.7: The variation of VLF signal amplitude as a function of the distance between the transmitter and receiver, as simulated from default propagation model of LWPC. The VTX-Kashmir (above) (2867 km) and VTX-Coochbehar (below) (2347 km) propagation paths are shown. The VLF data receiving points are indicated by *R* (Chakrabarti et al., 2012a).

### 3.4 Spatial profile of VLF signal

#### 3.4.1 LWPC simulation during Sunrise and Sunset

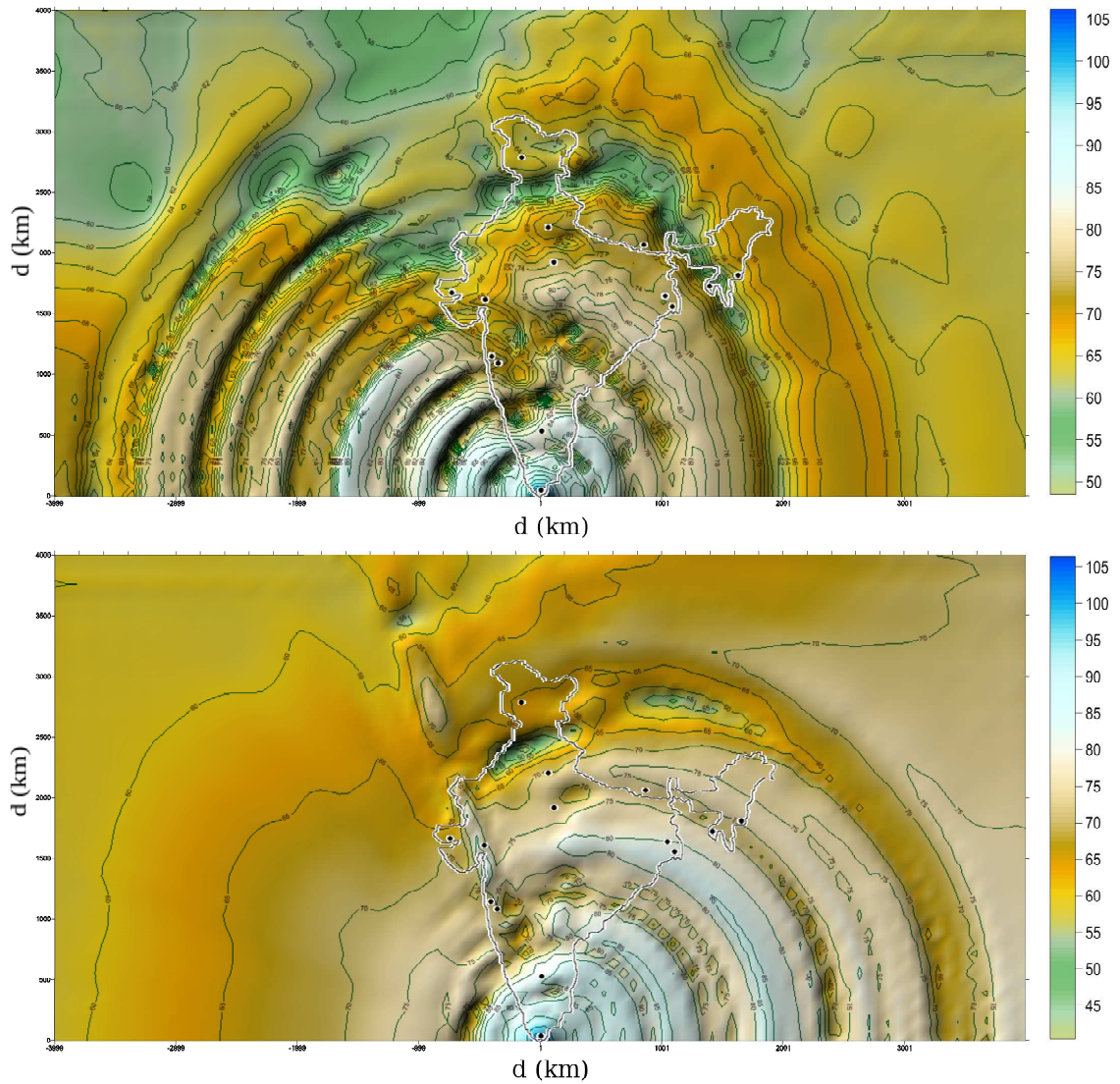


Figure 3.8: The LWPC simulated spatial amplitude distribution of VTX/18.2 kHz signal over the Indian subcontinent at 6:00am (top) and 6:30pm (bottom) (IST) on a winter day. The VLF signal amplitude has been shown with colour variation and also contours of constant amplitude (in dB) are drawn. The VTX transmitter is located at the origin of this plot (Basak et al., 2010).

In the waveguide mode theory, the signal propagates through several modes. In general, the higher order modes get attenuated as the distance from the transmitter increases. The LWPC code is based on this theory. The default propagation model of LWPC is the Long Wave Propagation Model (LWPM). It deals with the model of exponentially increasing ionospheric conductivity with height. A log-linear slope ( $\beta$  in  $\text{km}^{-1}$ ) and reference height ( $h'$ ) characterise the propagation model (also see Sec. 1.5.3). In the default case, for daytime ionosphere,  $\beta = 0.3 \text{ km}^{-1}$  and  $h' = 74 \text{ km}$  are constants for all frequencies between 10 kHz to 60 kHz. In the night-time ionosphere,  $h' = 87 \text{ km}$  and  $\beta$  varies from 0.3 to  $0.8 \text{ km}^{-1}$  depending on the frequency (Ferguson 1998; Pal & Chakrabarti 2010) (Basak et al., 2010). The ‘bearing’ sub-program of LWPC calculates the VLF signal amplitude and phase as the functions of distance from the transmitter. We calculated such VLF amplitude for each geomagnetic bearing angle to obtain entire spatial variation of the amplitude at a given time over Indian subcontinent for VTX/18.2 kHz signal (Basak et al., 2010).

In Basak et al. (2010), we have carried out this simulation at several times in a day. To show the effects of sunrise and sunset terminators on this spatial variation, we chose the times of simulations to be 6:00am and 6:30pm (IST) timings (Pal et al. 2011; Basak et al. 2011b). In the night-time, the interference patterns (see, Fig. 3.8) are more frequent due to the presence of many dominant modes. But in the daytime, the lower ionospheric weather is totally governed by solar flux variation, so that the spatial VLF amplitude profile evolves with local solar zenith angle. The presence of the terminator line in both the Figures are visible, which indicates the formation and dissolution of D-region during sunrise and sunset respectively. The 3-dimensional simulation results are in general agreement with the VLF campaign observations to a great extent (Basak et al., 2010). We divide the campaign data into *Eastern* and *Western* types (see Sec 3.3.1). Salt Lake, Malda, Khukurdaha, Kathmandu and some other sites have shown *Eastern* type during winter campaign. Fig. 3.8 also shows relatively higher amplitude level during nighttime (Basak et al., 2010).

## Chapter 4

# TIME DELAY OF VLF AMPLITUDES DURING SOLAR FLARES

### 4.1 Introduction to Time Delay

Due to ‘inertial’ properties of the ionosphere, the response to photo-ionization induced reactions is not instantaneous. Appleton (1953) calls it as the ‘sluggishness’ of the lower ionosphere. Basically, it arises due to several chemical reactions which take finite timescales to occur in the D-region. Some of these time scales are very long (Basak and Chakrabarti, 2013a). A parameter, similar to this, namely, the relaxation time ( $\tau$ ) has been calculated by Mitra (1974). A type of analysis of the relaxation time was reported by Valnicsek and Ranzinger (1972). Zigman et al. (2007) measured the time delay of VLF signal with respect to X-ray response of the flare and named it as the ‘VLF amplitude time delay’. In this work, we define this time delay as (Basak and Chakrabarti, 2013a),

$$\Delta t = APT - FPT, \quad (4-1)$$

where,  $APT$  is the Amplitude Peak Time of VLF signal and  $FPT$  is the X-ray Flare Peak Time. First, we compute the time delay of the response of the VLF signals with respect to all the classes of the solar X-ray flux variation (as recorded by GOES) (Basak and Chakrabarti, 2013a). Fig. 4.1 is a good example, which shows  $\Delta t$  for an M-class flare. In Fig. 4.2, we present a few examples of typical VLF amplitude response for X, M and C class flares. These are superposed on the X-ray light curve (details of those flares are marked in the Figure) as obtained by GOES-15 satellite. The general pattern of the X-ray light curve is the same as the VLF amplitude (Basak and Chakrabarti, 2013a).

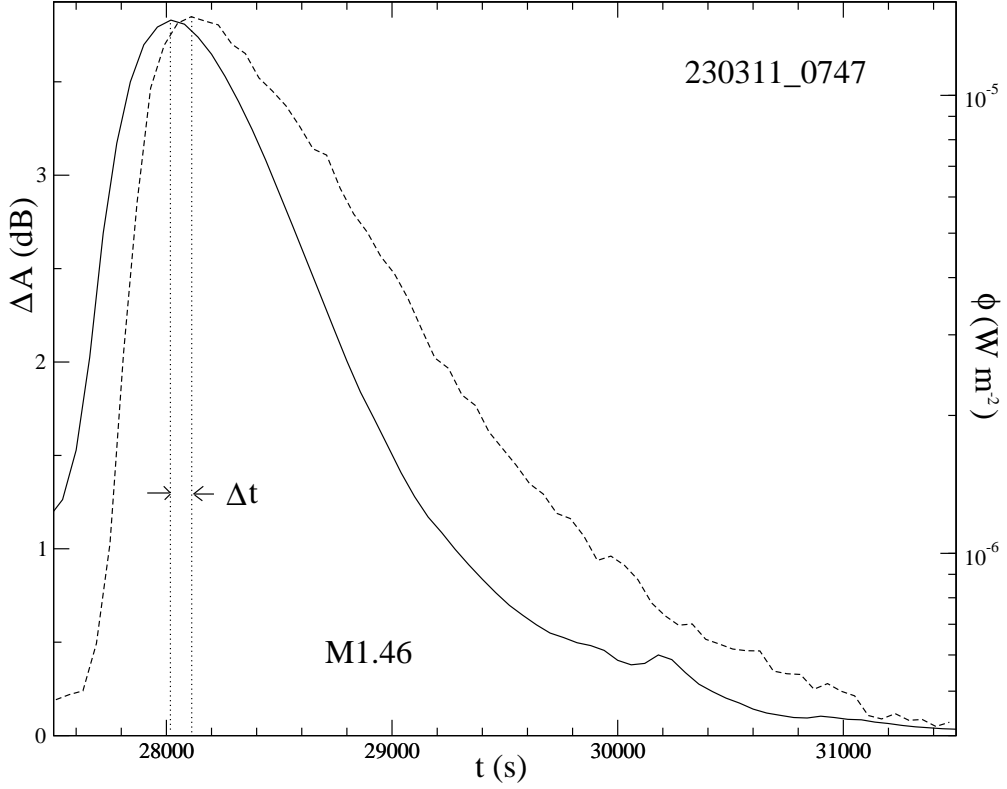


Figure 4.1: A typical example of  $\Delta t$ , the time delay of the VLF signal during an M1.46-class flare. The solid curve represents a typical soft X-ray irradiance  $\phi$  ( $\text{W m}^{-2}$ ) and the dashed curve represents the corresponding VLF amplitude deviation. The date and time are written in the ddmmyy\_hhmm format.  $\Delta A$  is in dB (Basak and Chakrabarti, 2013a).

## 4.2 Comparison of VLF and X-ray data during flare

### 4.2.1 Measurement of VLF amplitude perturbation

Maximum perturbed VLF amplitude ( $\Delta A_{max}$ ) is an important parameter for the D-region electron density simulation, which is defined as (Basak and Chakrabarti, 2013a),

$$\Delta A_{max} = A_{perturbed,max} - A_{quiet}, \quad (4-2)$$

where,  $A_{perturbed,max}$  is the maximum VLF perturbation for a given solar flare and  $A_{quiet}$  is the mean of the available data of five solar-quiet days around the ‘flare day’. We fitted the peak region of the  $\Delta A$  data with a higher order polynomial and chose

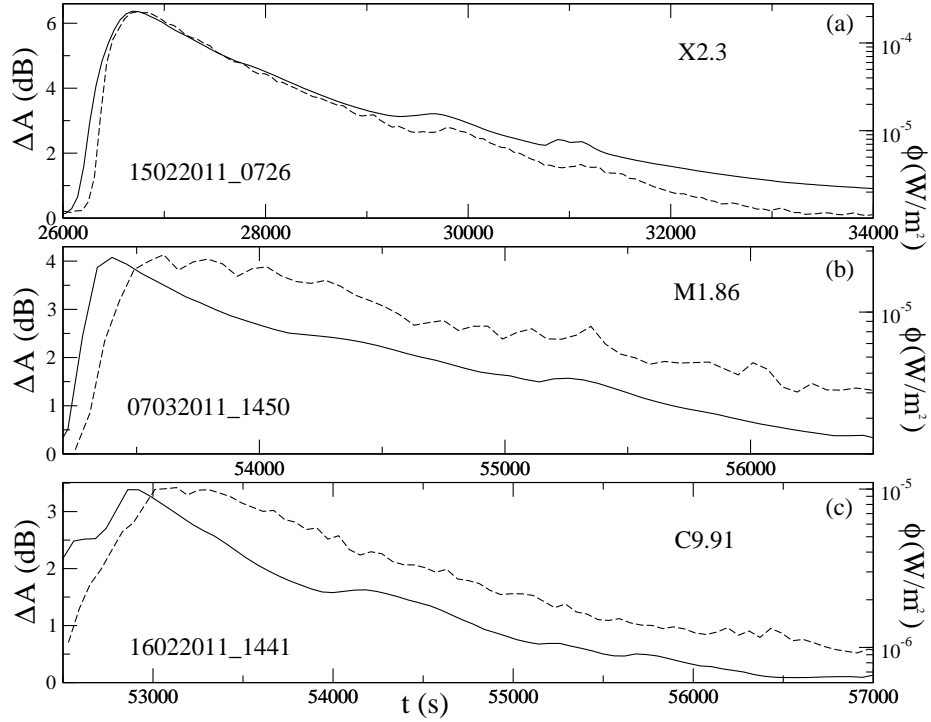


Figure 4.2: Examples of (a) X-class (b) M-class and (c) C-class solar X-ray flares as recorded by GOES-15 (solid lines) along with corresponding VLF signal amplitude deviations ( $\Delta A$ ) obtained by ICSP receivers (dashed lines). Date and time (ddmmyyy\_hhmm) are marked in respective panels (Basak and Chakrabarti, 2013a).

the  $\Delta A_{max}$  from the peak of the fitted polynomial (Basak and Chakrabarti, 2013a). Thus the possible error from direct measurements of the data was eliminated. We have chosen solar-quiet days, so that they are free from perturbations.  $\Delta A_{max}$  is in dB units (Basak and Chakrabarti, 2013a). This procedure is repeated for all the flares presented.

#### 4.2.2 Measurements of Time Delay

We already defined  $\Delta t$ . In all the cases under this analysis, the flare induced amplitude enhancements of the VLF signal lags behind the corresponding X-ray data (Basak and Chakrabarti, 2013a). A similar  $\Delta t > 0$  observations are reported by Zigman et al. (2007) for NAA/24kHz to Belgrade and other paths. We follow a few

steps to obtain this time delay accurately. The  $A_{perturbed,max}$ , we obtained is the perturbation of the signal strength due to the flare induced ionization of the D-region (Basak and Chakrabarti, 2013a). To obtain the peak time accurately, we adopted a new procedure. We used  $\phi$  directly from GOES satellite and assumed that the

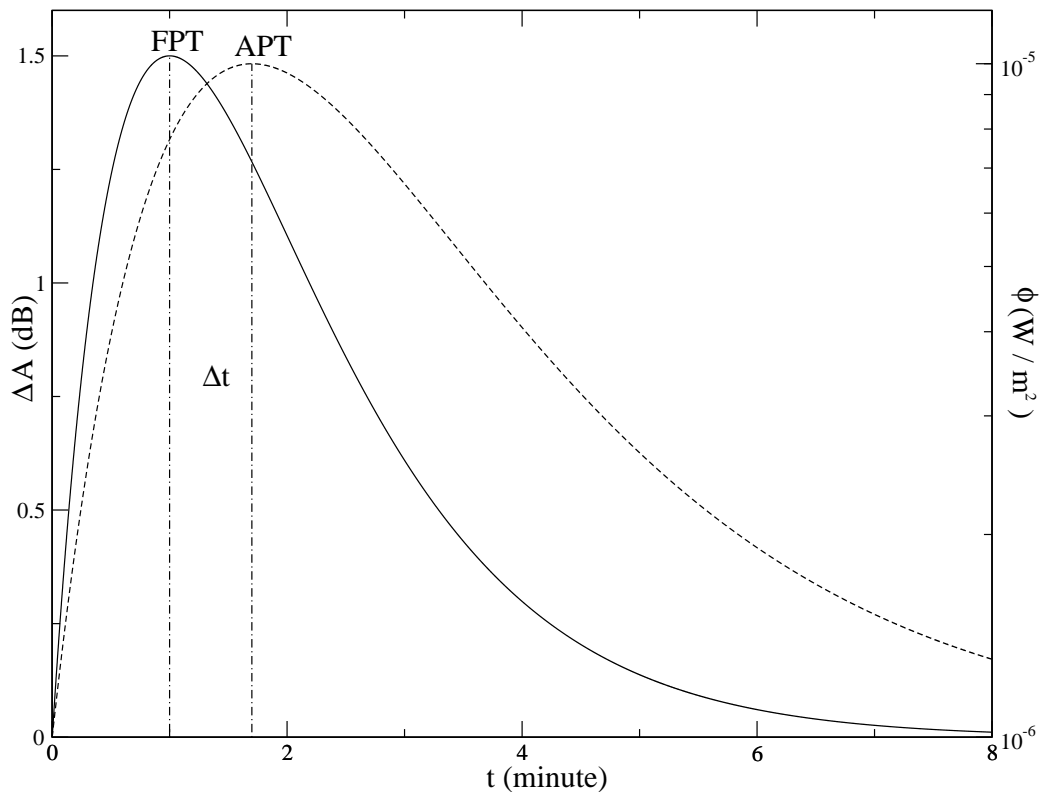


Figure 4.3: A schematic diagram showing the meaning of  $\Delta t$ , the time delay of the VLF signal. The solid curve represents a typical soft X-ray irradiance  $\phi$  ( $\text{W m}^{-2}$ ) and the dashed curve represents the corresponding VLF amplitude deviation ( $\Delta A$ ) in dB (Basak and Chakrabarti, 2013a).

background irradiance,  $\phi_{background}$  is constant during a flare (Basak and Chakrabarti, 2013a). The resolution of the available online data is one data point per minute. In this case, a proper detection of the peak X-ray flux density time ( $FPT$ ) and hence  $\Delta t$  especially for comparatively stronger flares is difficult. This limitation was overcome by using higher order polynomial fitting method, mentioned earlier in Section 4.2.1 and we took the peak time of the fitted graph of the polynomial as  $FPT$  (Basak and Chakrabarti, 2013a). Using Eqn. (4-1), we calculated  $\Delta t$ . We repeated the whole procedure described above, for each solar flare event presented

in this Chapter (Basak and Chakrabarti, 2013a). Fig. 4.3 shows  $\Delta t$  schematically.

### 4.3 Effective recombination coefficient during a solar flare

#### 4.3.1 Introduction to effective recombination coefficient during a solar flare

Ionospheric recombination coefficient indicates the time rate of recombination among positive, negative and neutral ions per unit volume after an ionizing action on ionosphere. The dissociative recombination coefficient ( $\alpha_D$ ) indicates the recombination among electrons, positive ions and positive cluster ions respectively. The mutual ionic recombination coefficient ( $\alpha_i$ ) measures the recombination among positive and several negative ions in the D-region. The effective recombination coefficient ( $\alpha_{eff}$ ) represents a combined effect of them along with the  $\lambda$ -parameter (Basak and Chakrabarti, 2013a), which would be discussed in Chapter 6.  $\alpha_{eff}$ -analysis is useful to represent overall recombining behaviour of lower ionosphere through simpler analysis. Early pioneering studies of the recombination of electrons and ions in lower ionosphere were made by Appleton (1953), Mitra and Jones (1953), Whitten et al. (1965), Wagner and Thome (1972), Whitten and Poppoff (1962), Mitra (1957,74), Rishbeth and Garriott (1969), Gledhill (1986) etc.

In this Section, we formulate a method to estimate the *effective recombination coefficient* ( $\alpha_{eff}$ ) at a low-latitude D-region ionosphere with the help of some established methods. The VLF amplitude time delay ( $\Delta t$ ) and VLF amplitude perturbation ( $\Delta A$ ) during a solar flare are crucial parameters. We particularly concentrated to calculate electron density because the positive and negative ions, due to their comparatively heavier masses than an electron, hardly affect the VLF propagation in lower ionosphere (Mitra 1992; Basak and Chakrabarti, 2013a). In Section 4.2, we described the way we estimated  $\Delta t$  and  $\Delta A$  from our VLF data. We concentrated on 22 flares which have a nearly similar  $Z$  in order to eliminate the effects of  $Z$ . We showed that  $\alpha_{eff}$  has an inverse relation with  $\phi_{max}$  (Basak and Chakrabarti, 2013a).

#### 4.3.2 Theoretical formulation for effective recombination coefficient

Our main aim in this Section is to obtain an expression of the *effective recombination coefficient* ( $\alpha_{eff}$ ) of D-region. The fundamental assumption of this calculation is that, the sub-ionospheric VLF signal quickly senses the changes in D-region elec-

tron density ( $N_e$ ) and adjusts itself accordingly (Basak and Chakrabarti, 2013a). Therefore, the VLF signal amplitude almost follows the temporal variation of  $N_e$  even during flares (i.e.,  $t_{\Delta A_{max}} = t_{N_{e,max}}$ ). Keeping total charge neutrality in mind, the D-region electron continuity equation can be written as (Whitten and Poppoff 1961; Rowe et al. 1970,74; Thomas and Bowmen, 1985; Hargraves and Birch 2005; Basak and Chakrabarti, 2013a),

$$\frac{dN_e}{dt} = \frac{q(t)}{1 + \lambda} - \frac{N_e}{1 + \lambda} \frac{d\lambda}{dt} - [\lambda^2 \alpha_i + \lambda(\alpha_i + \alpha_D) + \alpha_D] N_e^2, \quad (4-3)$$

where,  $\alpha_i$  is the ion-ion recombination coefficient,  $\alpha_D$  is the dissociative recombination coefficient and  $\lambda$  is the ratio of negative ion and electron density. The electron production rate of the D-region due to  $\phi(t)$  during the flare is given by (Zigman et al. 2007; Basak and Chakrabarti, 2013a),

$$q(t) = \frac{C\phi(t)}{eH} \cos Z, \quad (4-4)$$

where,  $e = 2.71828$ ,  $C = \rho^{-1}$  ( $\rho$  is the amount of energy required to create an electron-ion pair) and the scale height is given by (Mitra 1992; Basak and Chakrabarti, 2013a),

$$H = \frac{k_b T}{g m_{avg}}, \quad (4-5)$$

where,  $k_b$  is the Boltzman constant,  $g$  is the gravitational acceleration,  $m_{avg}$  is the mean molecular mass and  $T$  is the average temperature of lower ionosphere. According to Rowe et al. (1970) and Mitra (1974),  $\lambda$  is a slowly varying function of time. So we set,  $d\lambda/dt \simeq 0$ . Whitten et al. (1965) and Mitra (1974) reported that,  $\lambda \ll 1$  for altitudes above 70 km. So the Eqn. (4-3) can be approximated as (Basak and Chakrabarti, 2013a),

$$\frac{dN_e}{dt} = q(t) - \alpha_{eff} N_e^2, \quad (4-6)$$

where, *the effective recombination coefficient* as described in Section 4.3.1 is as follows,

$$\alpha_{eff} = \lambda(\alpha_i + \alpha_D) + \alpha_D. \quad (4-7)$$

Applying Eqn. (4-6) near  $t = t_{N_{e,max}}$  and  $t_{\phi_{max}}$ , the *effective recombination coefficient* would be (Zigman et al. 2007) (Basak and Chakrabarti, 2013a),

$$\alpha_{eff} = \frac{0.375}{\Delta t (N_{e,max} - q_{max} \Delta t)}. \quad (4-8)$$

Table 4.1: Data sheet of all included flares (Basak and Chakrabarti, 2013a)

<i>Date</i> ( <i>yyyymmdd</i> )	<i>time(s)</i> [ <i>IST</i> ]	$\phi_{max}$ ( $Wm^{-2}$ )	<i>Flare</i> <i>class</i>	$\Delta A_{max}$ ( <i>dB</i> )	<i>Z(deg.)</i>	$\Delta t(s)$	$N_{e,max}$ ( $m^{-3}$ )	$\alpha_{eff}$ ( $m^3s^{-1}$ )
20110121	35230	$3.33 \times 10^{-6}$	C3.33	1.315	27.0	151	$5.19 \times 10^9$	$9.155 \times 10^{-13}$
20110210	43560	$1.88 \times 10^{-6}$	C1.88	0.68	28.7	353	$3.34 \times 10^9$	$153.44 \times 10^{-13}$
20110210	44873	$2.06 \times 10^{-6}$	C2.06	0.791	32.4	307	$3.63 \times 10^9$	$23.94 \times 10^{-13}$
20110216	40526	$5.96 \times 10^{-6}$	C5.96	2.199	20.5	222	$9.71 \times 10^9$	$5.319 \times 10^{-13}$
20110218	37272	$4.03 \times 10^{-6}$	C4.03	1.039	18.0	183	$4.38 \times 10^9$	$27.67 \times 10^{-13}$
20110218	43365	$8.57 \times 10^{-6}$	C8.57	2.325	26.7	147	$10.84 \times 10^9$	$5.523 \times 10^{-13}$
20110219	45278	$2.63 \times 10^{-6}$	C2.63	0.918	32.4	247	$3.86 \times 10^9$	$23.197 \times 10^{-13}$
20110308	34140	$15.0 \times 10^{-6}$	M1.5	3.244	24.3	121	$26.65 \times 10^9$	$1.752 \times 10^{-13}$
20110308	38246	$5.5 \times 10^{-6}$	C5.5	2.021	14.2	140	$8.97 \times 10^9$	$5.182 \times 10^{-13}$
20110310	34052	$2.95 \times 10^{-6}$	C2.95	0.955	24.6	264	$4.06 \times 10^9$	$67.33 \times 10^{-13}$
20110311	36141	$5.5 \times 10^{-6}$	C5.5	2.11	17.9	140	$9.89 \times 10^9$	$4.4 \times 10^{-13}$
20110311	45175	$3.05 \times 10^{-6}$	C3.05	0.83	29.6	181	$3.70 \times 10^9$	$21.175 \times 10^{-13}$
20110414	39420	$4.99 \times 10^{-6}$	C4.99	1.957	14.3	134	$8.60 \times 10^9$	$5.282 \times 10^{-13}$
20110416	40071	$3.55 \times 10^{-6}$	C3.55	1.641	14.7	150	$6.45 \times 10^9$	$6.542 \times 10^{-13}$
20110607	43800	$25.5 \times 10^{-6}$	M2.55	3.005	28.8	90	$18.36 \times 10^9$	$5.929 \times 10^{-13}$
20110727	43760	$3.07 \times 10^{-6}$	C3.07	0.63	26.8	179	$3.270 \times 10^9$	$37.65 \times 10^{-13}$
20110728	36861	$2.29 \times 10^{-6}$	C2.29	0.761	23.2	190	$3.48 \times 10^9$	$14.855 \times 10^{-13}$
20110802	42542	$14.9 \times 10^{-6}$	M1.49	3.088	22.6	128	$20.57 \times 10^9$	$2.626 \times 10^{-13}$
20110803	36131	$17.3 \times 10^{-6}$	M1.73	3.123	23.8	145	$23.71 \times 10^9$	$2.283 \times 10^{-13}$
20110804	34017	$93.1 \times 10^{-6}$	M9.31	3.818	29.3	74	$44.5 \times 10^9$	$4.835 \times 10^{-13}$
20110817	35940	$2.31 \times 10^{-6}$	C2.31	0.647	22.1	298	$3.82 \times 10^9$	$29.61 \times 10^{-13}$
20110830	44009	$1.5 \times 10^{-6}$	C1.5	0.966	24.7	241	$4.06 \times 10^9$	$6.832 \times 10^{-13}$

Comparing Eqns. (4-4), (4-5) and (4-8) we get,

$$\alpha_{eff} = \frac{0.375}{\Delta t(N_{e,max} - \frac{\phi_{max} g m_{avg} \Delta t}{\rho e k_b T} \cos Z)}. \quad (4-9)$$

Among the constant terms in Eqn. (4-9),  $m_{avg} = 4.8 \times 10^{-26}$  kg (Mitra 1992) and  $\rho = 34$  eV (Whitten et al. 1965). Using SROSS-C2 satellite data, Sharma et al. (2004) measured electron and ion temperature changes of the ionosphere. They showed that electron temperature ( $T_e$ ) changes from 1.3 to 1.9 times and ion temperature ( $T_i$ ) changes from 1.2 to 1.4 times respectively during flares in comparison with normal days. Thus, the change of  $\alpha_{eff}$  due to the changes in  $T_e$  and  $T_i$  is low enough, compared to other ion-chemical effect induced changes. So for simplicity, we justifiably assumed a thermal equilibrium and took  $T = 210$  K (Schmitter 2011) to perform the entire calculation (Basak and Chakrabarti, 2013a). Since only solar flares which occurred close to the mid-day have been considered in this analysis to eliminate dependence on  $Z$ , we assume mean  $\cos Z = 0.90$  for our calculation (Basak and Chakrabarti, 2013a). This is justified because for the flares included here, the zenith angle varies between  $33^\circ$  to  $14^\circ$  (the  $Z$  values at each flare peak time are in Table 4.1) (Basak and Chakrabarti, 2013a). Our simulation procedure to obtain  $N_{e,max}$  will be discussed in the next Section.

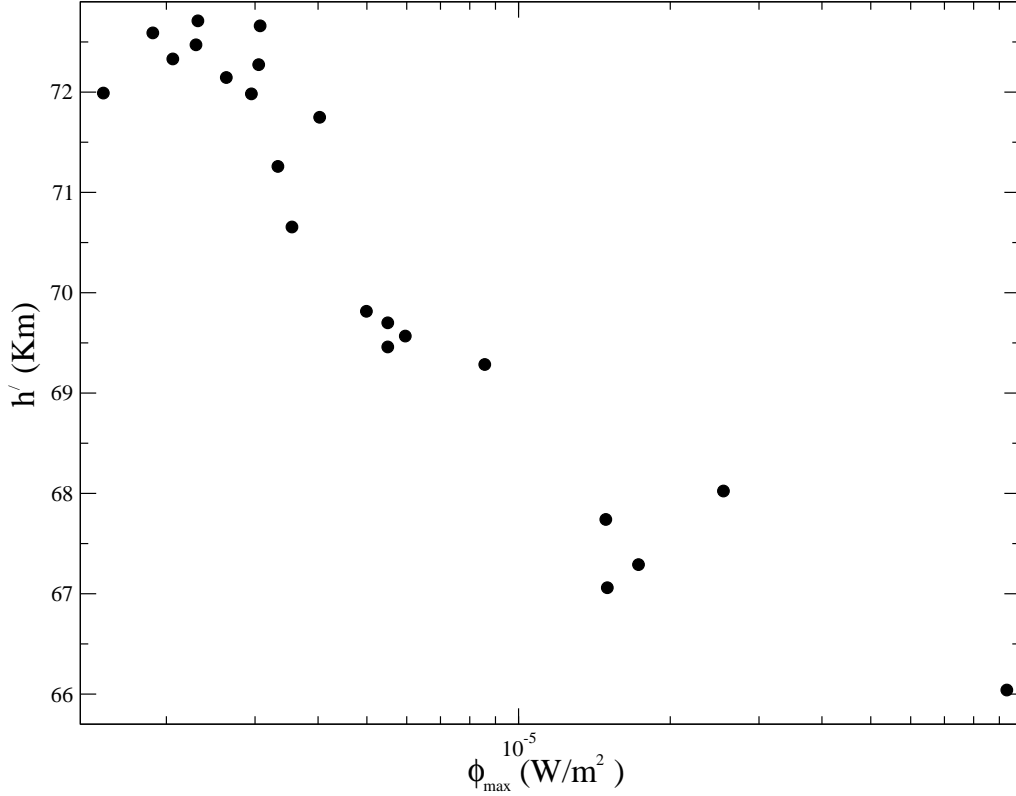


Figure 4.4: Simulated effective reflection height ( $h'$ ) (km) is plotted with corresponding peak flare flux ( $\phi_{max}$ ) ( $\text{W m}^{-2}$ ) (Basak and Chakrabarti, 2013a).

### 4.3.3 LWPC simulation of the D-region electron density during flares

Long Wave Propagation Model (LWPM) is the default propagation model of the lower ionosphere (Ferguson 1998). It has an exponential increase in  $N_e$  and conductivity. A sharpness factor ( $\beta$ ) and effective reflection height ( $h'$ ) define this ionosphere model (Wait and Spies 1964).  $h' = 74 \text{ km}$  and  $\beta = 0.3 \text{ km}^{-1}$  are constant values being assumed to define daytime unperturbed ionosphere, even constant for the entire VLF range (Basak and Chakrabarti, 2013a). We carried out the simulation of lower ionosphere over a single  $T_x$ - $R_x$  propagation path from NWC transmitter to IERC, Sitapur receiving station. As we mentioned in Section 4.3.1 that in  $\alpha_{eff}$  analysis, to avoid the zenith angle ( $Z$ ) dependence, we only accommodated those flares, which occurred when the sun was close to the zenith (all  $Z$  values averaged over  $T_x$ - $R_x$  path are mentioned in Table 4.1) with respect to VLF signal propagation path (Basak and Chakrabarti, 2013a). So we assumed that the flare induced

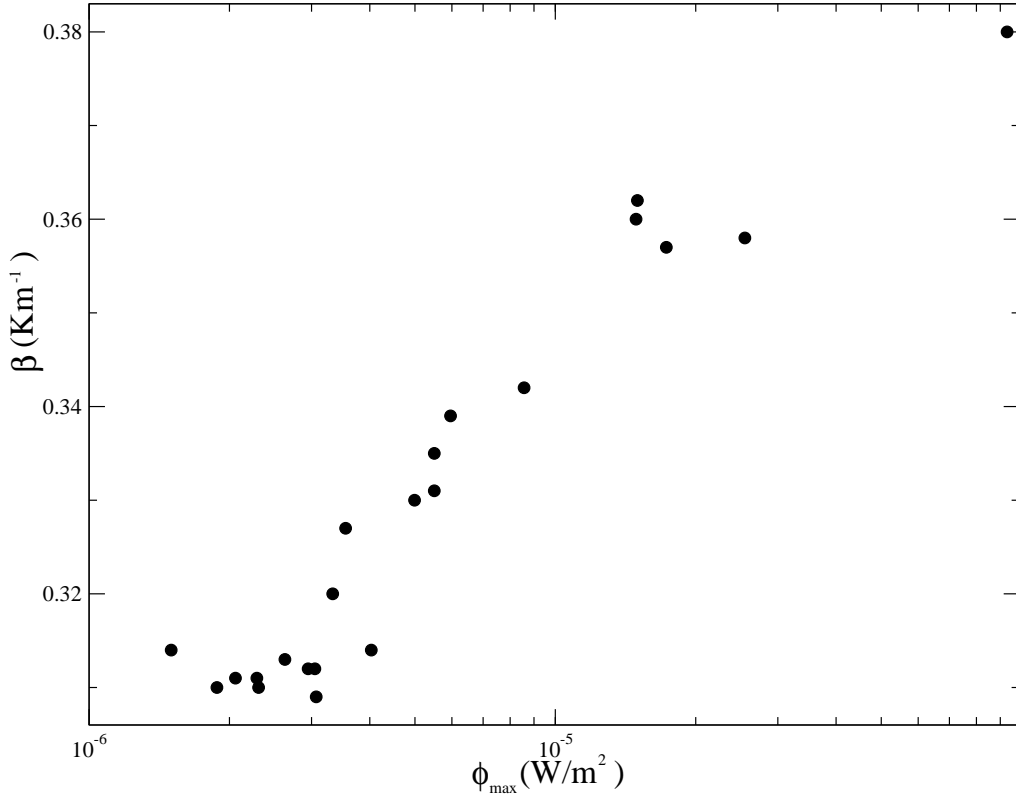


Figure 4.5: Simulated sharpness factor ( $\beta$ ) ( $\text{km}^{-1}$ ) is plotted with corresponding peak flare flux ( $\phi_{max}$ ) ( $\text{W m}^{-2}$ ) (Basak and Chakrabarti, 2013a).

perturbation of the reflection height for the entire horizontal path segments are the same (Basak and Chakrabarti, 2013a).

We used RANGE EXPONENTIAL model to handle the perturbed ionosphere due to flares. First, we added the  $\Delta A_{max}$  with unperturbed ionosphere VLF amplitude ( $A_{lwpc}$ ) corresponding to  $h' = 74 \text{ km}$  and  $\beta = 0.3 \text{ km}^{-1}$  (Pal and Chakrabarti 2010; Pal et al. 2012a, b; Basak and Chakrabarti, 2013a). The unperturbed D-region electron density is calculated as,  $N_{e,unperturbed} = 2.2 \times 10^8 \text{ m}^{-3}$ . To authenticate  $N_{e,unperturbed}$ , we obtain the same unperturbed value (averaged over the entire propagation path) from IRI-model of NASA as,  $(N_{e,unperturbed})_{IRI} = 4.4 \times 10^8 \text{ m}^{-3}$ . There is a little disagreement because LWPC follows Wait's 2-parameter lower ionospheric approximate model instead of the exact and more realistic model. This small disagreement would not affect the results, as flare induced  $N_e$  is high by a few orders of magnitude than the unperturbed values (Basak and Chakrabarti, 2013a).

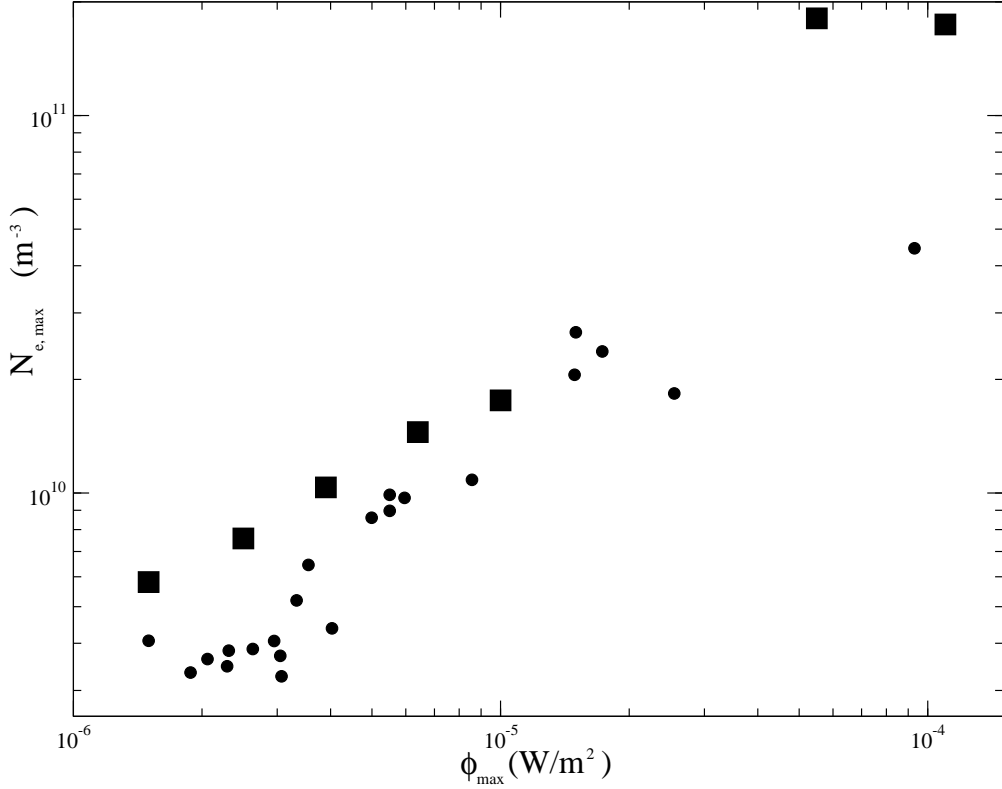


Figure 4.6: (a) Simulated D-region electron density (circles) ( $N_{e,max}$ ) ( $\text{m}^{-3}$ ) at  $h = 74$  km is plotted with corresponding peak flare flux ( $\phi_{max}$ ) ( $\text{W m}^{-2}$ ) (b) Also  $N_{e,max}$  (squares) calculated at  $h = 74.1$  km using  $\alpha_{eff}$  values taken from Zigman et al. (2007) (Basak and Chakrabarti, 2013a).

We now run the program to simulate Wait's parameters corresponding to the perturbed VLF amplitude ( $A_{lwpc} + \Delta A_{max}$ ) and this process is repeated for all 22 flares which are detected close to local mid-day (Basak and Chakrabarti, 2013a).

In Figs. 4.4 and 4.5, these  $h'$  and  $\beta$  are plotted with corresponding  $\phi_{max}$  respectively. Now using Wait's formula (Wait and Spies 1964; Pal and Chakrabarti 2010; Pal et al. 2012a, b; Basak and Chakrabarti, 2013a),

$$N_{e,max} \propto e^{-\beta h'} e^{(\beta - \beta_0)h}, \quad (4-10)$$

where,  $\beta_0 = 0.15 \text{ km}^{-1}$ , we got electron density at a height  $h$ . We repeated the entire LWPC simulation for several complex ion density profile values and we noted hardly any change for VLF signal amplitude perturbation results.

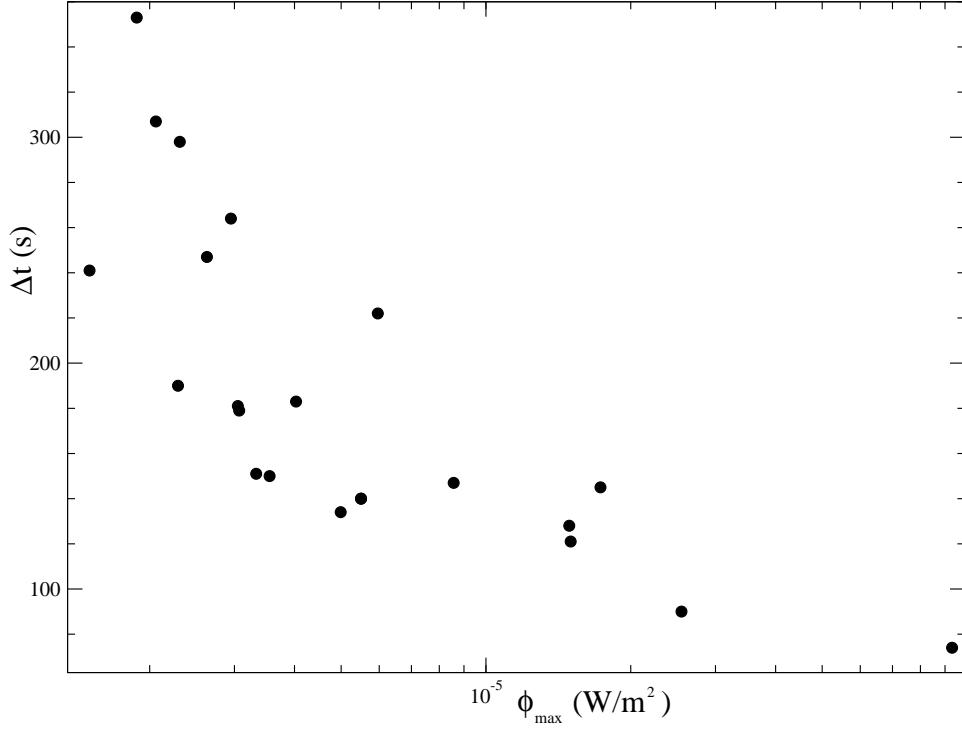


Figure 4.7: VLF amplitude time delay ( $\Delta t$ ) is plotted as a function of corresponding peak flare flux ( $\phi_{max}$ ,  $\text{W m}^{-2}$ ) for the same flares shown in Fig. 4.6 (Basak and Chakrabarti, 2013a).

#### 4.3.4 Estimation of effective recombination coefficients using Time Delay

We analysed 22 solar flares having  $Z$  within  $\sim 15^\circ$  to  $30^\circ$ . We got the expression for  $\alpha_{eff}$  as Eqn. (4-9) and from LWPC simulation, we estimated  $N_{e,max}$  for each flare (Eqn. 4-10). In Fig. 4.6, the LWPC simulated  $N_{e,max}$  (at height  $h = 74$  km) is plotted with corresponding  $\phi_{max}$ . Also for verification of our LWPC simulation results, we again calculated  $N_{e,max}$  at  $h = 74.1$  km height, using  $\alpha_{eff}$  values taken from Zigman et al. (2007). Though the simulated  $N_{e,max}$  values are a bit underestimated with respect to the values adapted from literature, by keeping our measurement errors in mind, the general agreement is good (Basak and Chakrabarti, 2013a). Substituting each  $N_{e,max}$  to Eqn. (4-9),  $\alpha_{eff}$  can be calculated (see, Table 4.1). The values of  $\Delta t$  are depicted in Fig 4.7 (Basak and Chakrabarti, 2013a). In Fig. 4.8,  $\alpha_{eff}$  versus  $\phi_{max}$  has been shown, the values of  $\alpha_{eff}$  go from  $\sim 10^{-13} \text{ m}^3\text{s}^{-1}$

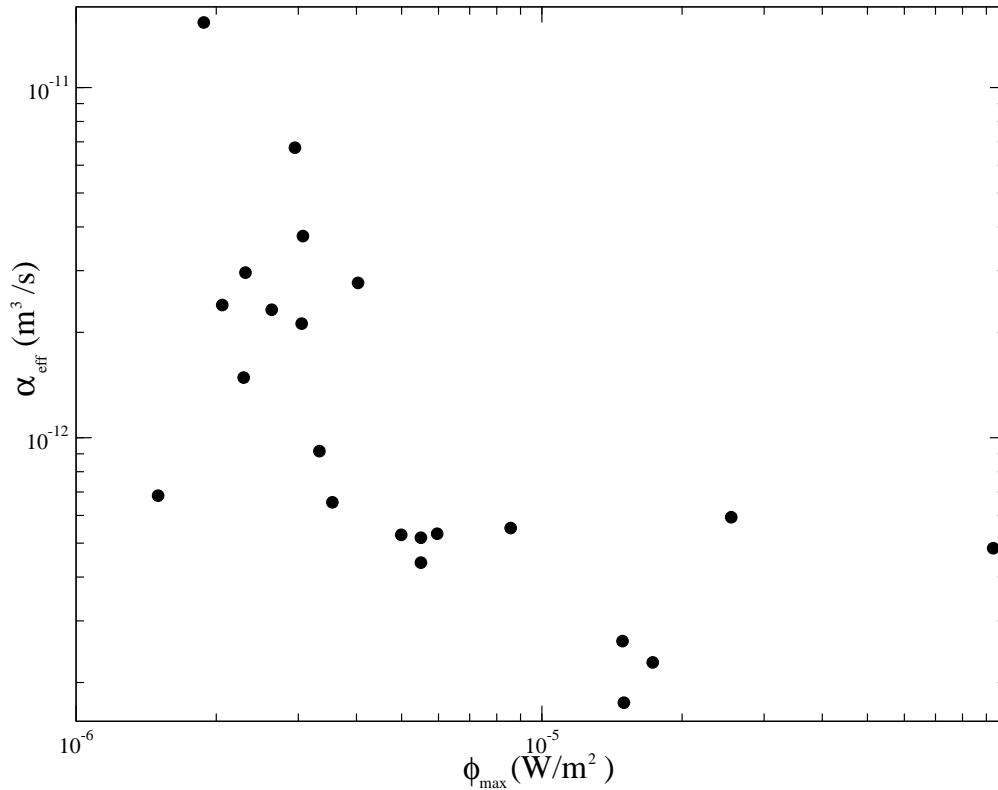


Figure 4.8: Effective reflection coefficient ( $\alpha_{eff}$ ) ( $m^3s^{-1}$ ) is plotted with corresponding peak flare flux ( $\phi_{max}$ ) ( $W m^{-2}$ ) (Basak and Chakrabarti, 2013a).

to more than  $10^{-11} m^3s^{-1}$  for  $\sim$  C1.0 to M9.0 classes of flares. We see that  $\alpha_{eff}$  and  $\phi_{max}$  are generally correlated with some exceptions (Basak and Chakrabarti, 2013a). That exception may be due to the zenith angle ( $Z$ ) variation during observation. The calculated values of  $\alpha_{eff}$  for low latitude D-region ionosphere generally agree with the results of Parthasarathy and Rai (1965); Balachandra Swamy (1991); Zigman et al. (2007). Fehsenfeld and Ferguson (1969); Mitra and Rowe (1972); Mitra (1974) reported that increase in solar flux intensity transforms the water-cluster ions to molecular ions. Though that process is dominant near mesopause region, but we report that at 74 km in D-region the transformation occurs at a significant level and hence  $\alpha_{eff}$  is reduced. Our results support this observation (Basak and Chakrabarti, 2013a).

#### 4.4 Solar zenith angle effects on Time Delay

The solar zenith angle ( $Z$ ) is the angle measured from the local zenith to the geometric centre of the solar disc, as described here using a horizontal coordinate system (Fig. 4.9). It depends on the local time and latitude of the location of measurement. The solar elevation angle ( $\theta_L$ ) is the complementary angle of  $Z$ , which measures the angular altitude of the sun from the horizon to the centre of the solar disc. The

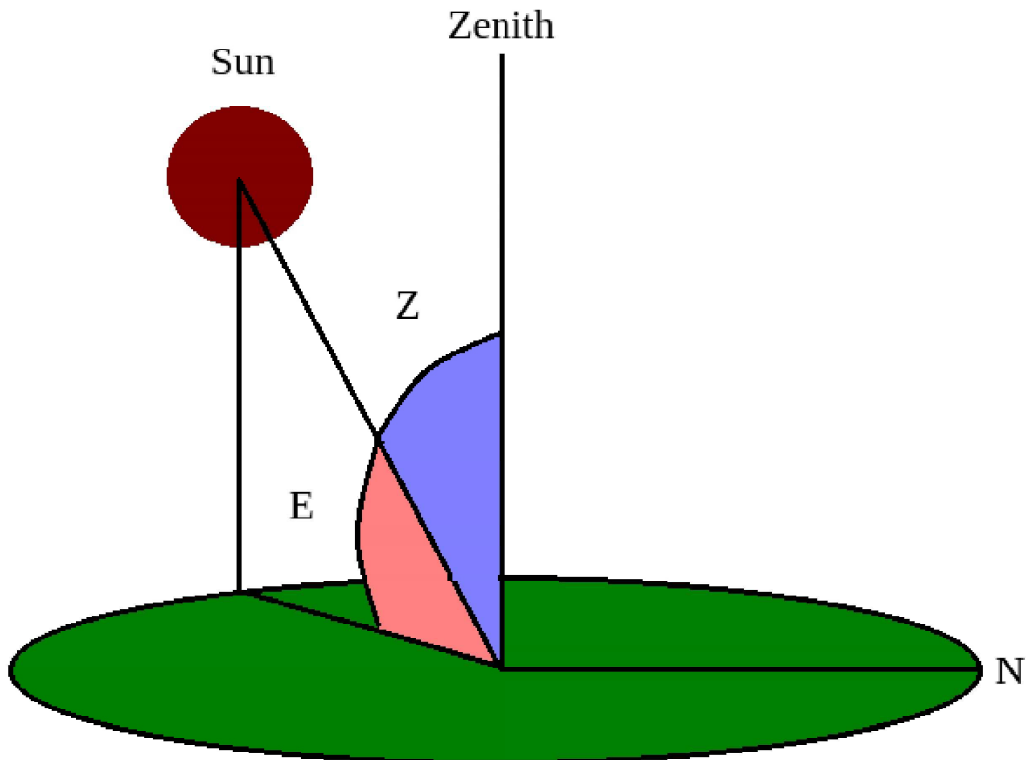


Figure 4.9: Solar zenith angle ( $Z$ ) and solar elevation angle ( $E$ ).

solar zenith angle is given by,

$$Z = \cos^{-1}(\sin L_t \sin \delta + \cos L_t \cos \delta \cos H), \quad (4-11)$$

where, the  $L_t$  is given by local latitude,  $\delta$  is the solar declination angle and  $H$  is the local time dependent solar hourly angle.

The present Section consists of two different analysis. First of these is related to how measured  $\Delta ts$  vary (for a certain type of flares) depend on  $Z$  which is computed

along the propagation path at the flare occurrence time. We investigated a total of 22 flares. As the  $\Delta t$  has been found to depend on the strength of flares, we chose only the C-class flares (as they are also numerous). We observe that the average zenith angle ( $Z$ ) over the path during flare occurrence has a linear correlation with  $\Delta t$  (Basak and Chakrabarti, 2013a). We compute this correlation quantitatively. Ours is an alternative method to estimate the relation between  $N_e$ -profile of D-region and  $Z$ , because  $\Delta t$  is directly connected to  $N_e$  (Mitra 1974; Zigman et al. 2007; Basak and Chakrabarti, 2013a). Similar correlations of time delay with  $Z$  can be tested for the M-class or X-class flares, but since their numbers are much lower, for a good statistics, we need to collect the data for a longer period.

#### 4.4.1 Direct correlation between the solar zenith angle and the time delay during C-class flares

In the Section, we discuss the variation of ionospheric time delay ( $\Delta t$ ) during flares with  $Z$  over the NWC-IERC signal propagation path. We calculate the average zenith angle ( $Z$ ) by taking the mean of the zenith angle values at every  $10km$  interval along the propagation path at the peak time of the flare (Basak and Chakrabarti, 2013a). We did this to incorporate different inclinations of solar radiation at different path segments. We computed this for the 22 C-class flares which are from C2 to C7. One of the reasons to confine our discussion for a single C-class is this: the  $\Delta t$  has a dependence on  $N_{e,max}$  and hence on  $\phi_{max}$  according to Mitra (1974) (Basak and Chakrabarti, 2013a). If we mix various classes of the flares, such a dependence might shadow the effect we are after. Thus, we concentrated on flares of the same class occurring at various times of the day. We could do similar analysis for other classes also, but their numbers were too few to establish a correlation beyond any reasonable doubt (Basak and Chakrabarti, 2013a). In Fig. 4.10, the  $\Delta t$ s are plotted against their occurrence times ( $t$ ) [IST] and the fitted curve has been drawn to show the variation with diurnal time and hence with  $Z$ . It is interesting that the mean curve closely follows typical diurnal  $Z$  variation.  $Z$  starts decreasing after sunrise. It is minimum during the mid-day when the sun is close to the zenith and gradually increases towards the sunset (Basak and Chakrabarti, 2013a). The errorbars of  $\Delta t$  represent the resolution of the recorded VLF amplitude data and the available online X-ray flux. Le et al. (2007, 2012) has shown the  $Z$ -dependence of the upper ionosphere using TEC measurements and here we showed the  $Z$  dependence of lower ionospheric response (Basak and Chakrabarti, 2013a). For further analysis, we plot  $\Delta t$  directly with corresponding  $Z$  (Fig. 4.11) and fit them with a straight

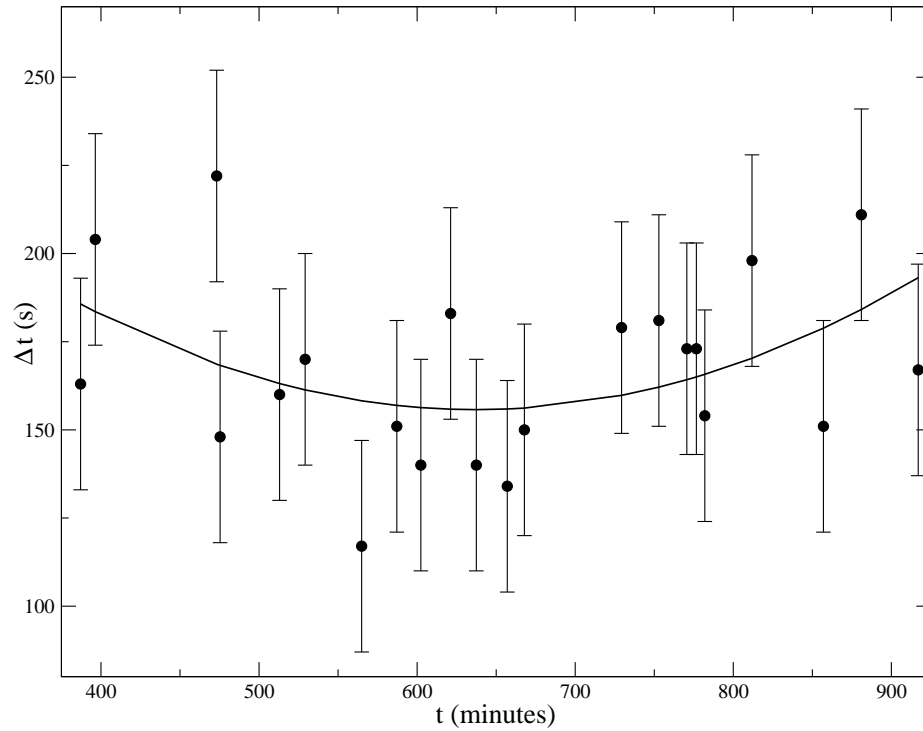


Figure 4.10: The time delay ( $\Delta t$ ) (s) of the ionosphere for each C-class solar flare is plotted as a function of their occurrence time  $t(\text{mins})$ . The solid line is the fitted mean curve for these data points (Basak and Chakrabarti, 2013a).

line to show a direct correlation. In the equation of the straight line (Basak and Chakrabarti, 2013a),

$$\Delta t = a_1 Z + a_2, \quad (4-12)$$

the fitted values are  $a_1 = 0.7556 \text{ deg}^{-1} \text{ s}$  and  $a_2 = 137.24 \text{ s}$ . The goodness of the fit is established as the *reduced- $\chi^2$*  = 0.92 (No. of data points  $N = 22$  and fitted using,  $P = 2$  parameters (see Eqn. 4-12), so the available degrees of freedom for this  $\chi^2$  - test is,  $N - P = 22 - 2 = 20$ ). We see that the *reduced- $\chi^2$*  is close to unity and thus the correlation is very good (Basak and Chakrabarti, 2013a). From a physical point of view, this correlation can be explained in the following way: the residual degree of ionization and free electron density ( $N_e$ ) of lower ionosphere is mostly governed by  $Z$ . During solar flares, bombardment of higher energetic X-ray photons on ionospheric bed leads to chemical evolution and excitation but the  $Z$ -dependence of the flux remains (Basak and Chakrabarti, 2013a).

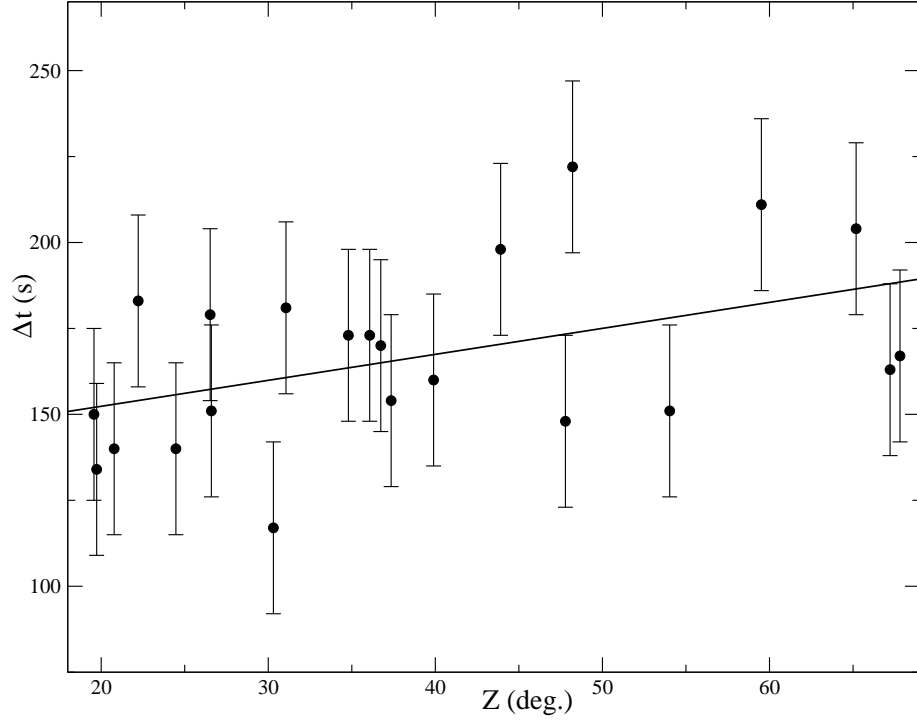


Figure 4.11: The time delay ( $\Delta t$ ) (s) of the ionosphere for each C-class solar flare is plotted as a function of  $Z$  at their occurrence time. The solid line is the fitted straight line for those data points (Basak and Chakrabarti, 2013a).

#### 4.4.2 Zenith angle effects on the correlation between peak flare flux and time delay

We extend our analysis to study the effects of the Zenith angle of the sun when the flare took place. In this part of the analysis, we chose 78 flares of C, M and X-classes which occurred at different times of the day. We grouped them into six separate equal sized time bins ( $DT$ ) according to their occurrence times. For each bin, we fitted  $\Delta t$  versus peak flare flux ( $\phi_{max}$ ) of respective flares with an empirically chosen exponentially decaying function and calculated *reduced- $\chi^2$*  to estimate the goodness of fit (Basak and Chakrabarti, 2013a). Finally, we compute the average and standard deviation ( $\sigma$ ) of the solar zenith angle  $Z$  (averaged over the  $T_x$ - $R_x$  propagation path) for each  $DT$ , and the *reduced- $\chi^2$*  varies exactly in the same way as the standard deviation ( $\sigma$ ) of zenith angle ( $Z$ ) distributed over  $T_x$ - $R_x$  path within each time bin  $DT$  (Basak and Chakrabarti, 2013a).

Table 4.2: Details of flares in different time-bin (Basak and Chakrabarti, 2013a)

	<i>Time range (s)</i>	C- type	M- type	X- type	<i>a (s)</i>	<i>b</i>	<i>Red-<math>\chi^2</math></i>	<i>f =</i> <i>N - P</i>	<i><math>\sigma</math></i> <i>(deg.)</i>
DT1	22000-28000	6	4	1	347.0	0.39	0.923	9	3.231
DT2	28000-34000	14	3	0	247.1	0.23	1.039	15	3.084
DT3	34000-40000	8	3	0	311.3	0.35	1.324	9	6.535
DT4	40000-46000	8	2	0	346.8	0.40	1.532	8	13.698
DT5	46000-52000	11	4	1	219.4	0.29	1.663	14	12.629
DT6	52000-58000	12	1	0	238.6	0.30	1.725	11	12.26

### *Sorting and grouping of solar flares*

We binned 78 flares of C, M and X classes into six separate 100-min time-bins namely, *DT1*, *DT2*, *DT3*, *DT4*, *DT5* and *DT6*. The data is taken from the data bank of IERC/ICSP for the NWC-IERC propagation path. The range of time-bins and details of the flares present in those bins are given in Table 4.2. The pictorial presentation is in Fig. 4.12. We chose the size of bins in a way that they are sufficiently small so that one could assume  $Z$  to be constant in each bin and are sufficiently big, so that there are statistically significant number of flares in each bin (Basak and Chakrabarti, 2013a). Thus, we neglect the  $Z$  variation within a given bin and for validity of our statistical results we accommodated sufficient number of flare cases in each bin from the available VLF data.

### *Time bin wise analysis of flare events*

Time delay ( $\Delta t$ ) is defined by Eqn. (4-1) is similar to the time delay parameters defined by Appleton (1953); Valnicsek and Ranzinger (1972); Zigman (2007) etc. We first fit the X-ray and VLF data analytically before obtaining  $\Delta t$  (Section 4.2.2). In the Section 4.4.1, we sorted only the C-class flares and showed that,  $\Delta t = f_1(Z)$ , i.e.,  $\Delta t$ s for these flares depend on mean  $Z$  computed over the signal propagation path (Basak and Chakrabarti, 2013a).

While calculating  $\alpha_{eff}$  in Section 4.3.4, we showed that,  $\Delta t = f_2(\phi_{max})$ , i.e.,  $\Delta t$  significantly depends of the corresponding peak flare flux  $\phi_{max}$  (Basak and Chakrabarti, 2013a). In order to demonstrate  $\Delta t = f(Z, \phi_{max})$ , i.e., the dependence of  $\Delta t$  on  $\phi_{max}$  and  $Z$  simultaneously, we introduce this new approach. Observing the nature of dependence, we assume an empirical relation between the  $\Delta t$  and  $\phi_{max}$

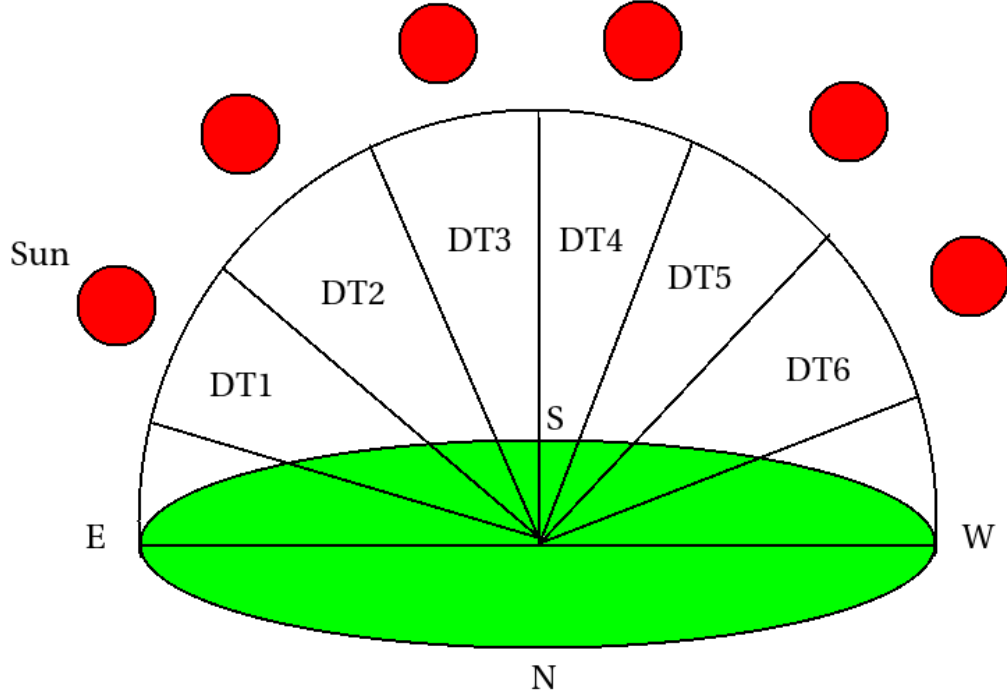


Figure 4.12: Schematic diagram of the positions of the sun at  $DT1$  to  $DT6$  time bins.

for the flares in each bin (Basak and Chakrabarti, 2013a):

$$\Delta t = ae^{-b(\log_{10} \phi_{max})}, \quad (4-13)$$

where,  $a$  and  $b$  take real values. We then fit data points of each bins separately using non-linear least square fitting technique using *Gnuplot* software and  $a$  and  $b$  are the parameter values (see, Table 4.2) corresponding to best fitting of Eqn. (4-13) and calculated *reduced- $\chi^2$*  for every fit to test the ‘goodness of fit’. The *reduced- $\chi^2$*  for  $j$ -th bin is (Basak and Chakrabarti, 2013a),

$$reduced \chi_j^2 = \frac{1}{f} \sum_{DT} \frac{(\Delta t_{obs} - \Delta t_{em})^2}{\sigma_{err}^2}, \quad (4-14)$$

where,  $\Delta t_{obs}$  is experimentally observed time delay,  $\Delta t_{em}$  is the time delay calculated using Eqn. (4-13),  $\sigma_{err}$  is the size of the errorbar, which comes from the limitations of the measuring instrument. In our case,  $\sigma_{err} = 30s$ . Now the degree of freedom is defined as,

$$f = N - P, \quad (4-15)$$

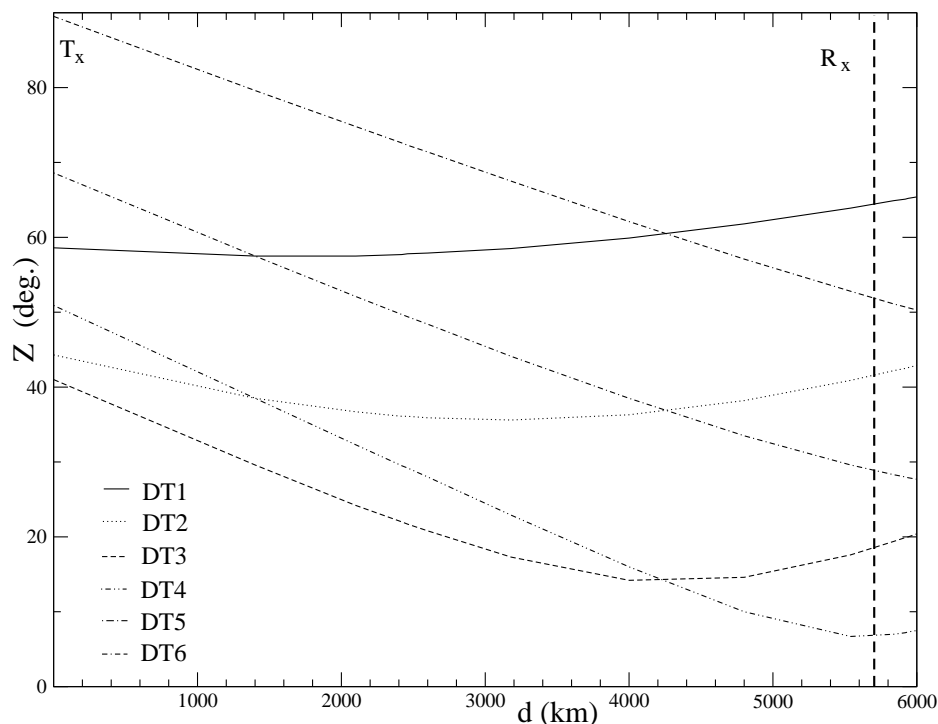


Figure 4.13: Variation of the mean zenith angle ( $Z$  in deg.) as a function of  $T_x$ - $R_x$  path at middle of time-bins mentioned in Table 4.2.  $T_x$  is at  $d = 0$  km and  $R_x$  is at  $d = 5691$  km (Basak and Chakrabarti, 2013a).

where,  $N$  is the number of flares within  $j$ -th time-bin and  $P$  is number of model parameters used to fit  $N$  number of data points and here  $P = 2$  from Eqn. (4-13). Our main objective here is to check the nature of  $\Delta t$  at different  $Z$ . This is because, the residual degree of ionization (due to Lyman- $\alpha$  and soft X-ray) of lower ionosphere is mainly governed by  $Z$ . In Fig. 4.13, we plot the variation of  $Z$  along  $T_x$ - $R_x$ . Six different graphs represent typical  $Z$  variation at midway of each time bin. Along the entire path,  $Z$  varies considerably for some time bin (e.g.  $DT3$ ,  $DT4$ ,  $DT5$ ,  $DT6$  mainly), and thus it is not possible to assume  $Z$  to be a constant. One way to quantify  $Z$  for each time bin, would be to measure ‘how bad’ the assumption of constant  $Z$  is. In other words, we would be interested in obtaining the standard deviation ( $\sigma$ ) of  $Z$  for each time bins. This  $\sigma$  will thus be an estimate of variation of residual ionization due to the flare alone along  $T_x$ - $R_x$  path (Basak and Chakrabarti, 2013a). In the next Section, we would test our hypothesis that if  $\sigma$  is large, i.e., the variation of ionization along the path is significant, then the *reduced- $\chi^2$*  is also

going to be large, i.e., the correlation between  $\Delta t$  and  $\phi_{max}$  would also not be very tight. The reverse should also be true, i.e., if  $\sigma$  is small, then *reduced- $\chi^2$*  is also small.

*Correlation between  $\sigma$  of zenith angle and reduced- $\chi^2$*

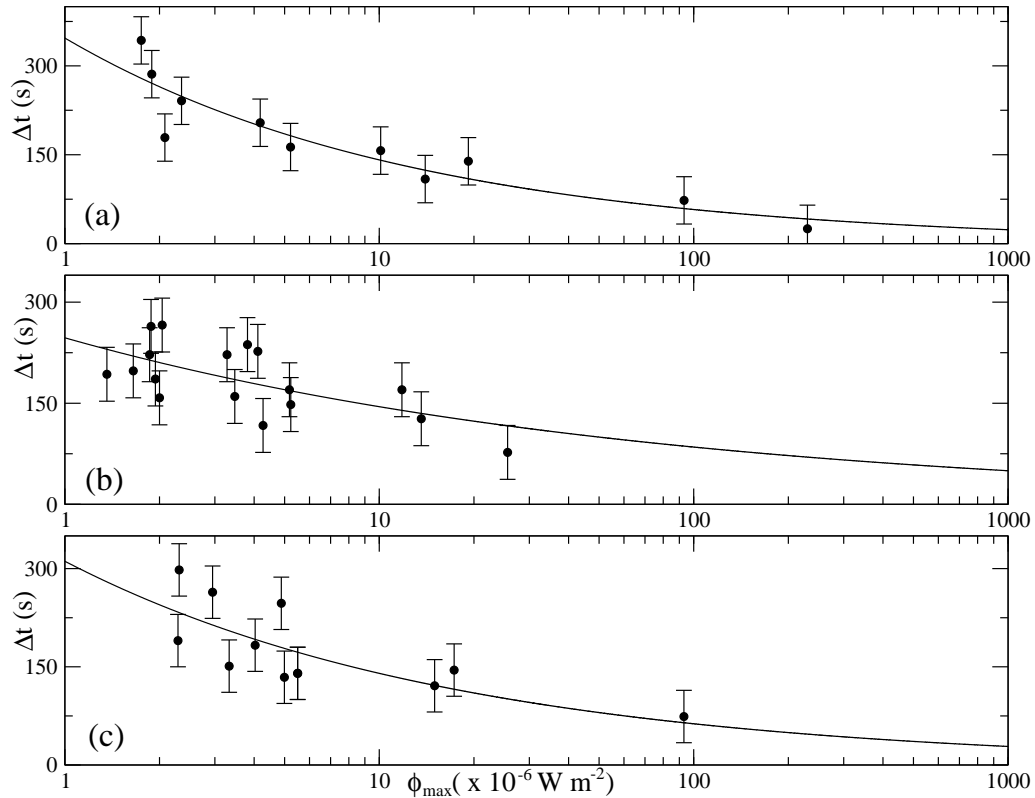


Figure 4.14: The time delay [ $\Delta t(s)$ ] for each of the solar flares has been plotted as a function of peak flare flux ( $\phi_{max}$  in  $\text{W m}^{-2}$ ). The solid line is the fitted empirical function (Eqn. 4-13). The time bins are (a)DT1, (b)DT2 and (c)DT3 (Basak and Chakrabarti, 2013a).

We have analysed a total of 78 flares (Table 4.2) and for each flare, the VLF peak appeared after the X-ray peak. Hence for all the cases under this investigation we got,  $\Delta t > 0$ . Grouping techniques and analysing procedures of flares are already discussed in the earlier Section. The procedure is from Basak and Chakrabarti (2013a).

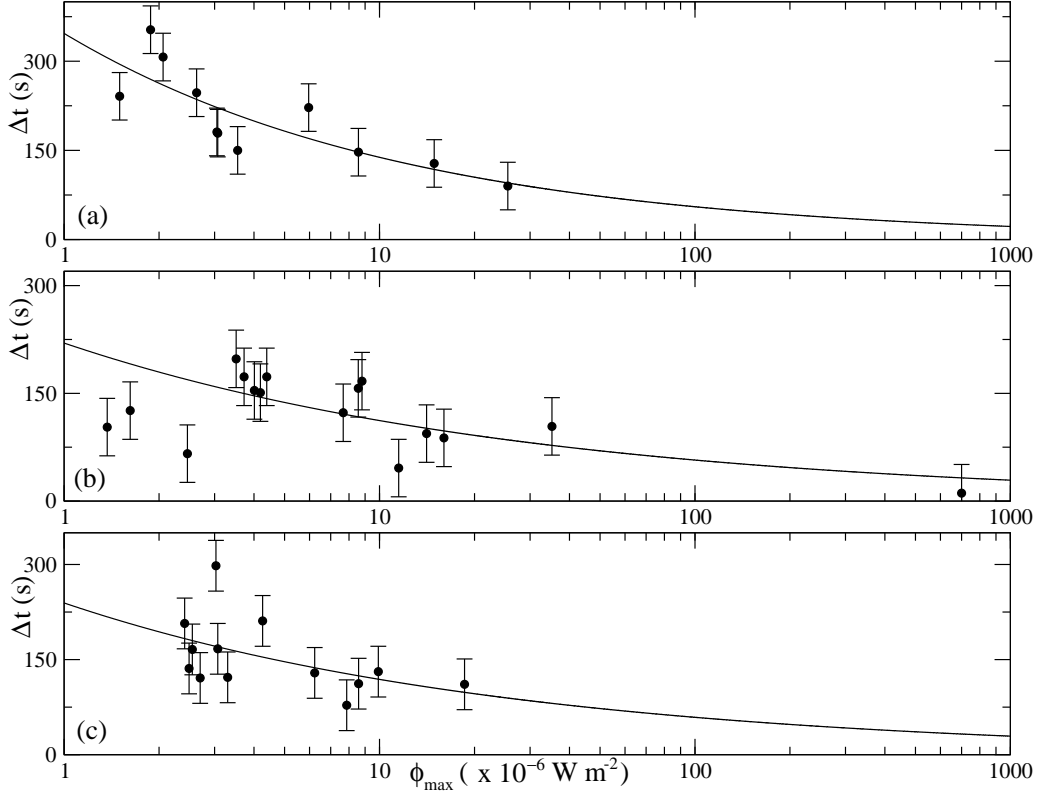


Figure 4.15: The same plot of time delay ( $\Delta t$ ) as in Fig. 4.14. The time bins are (a) *DT4*, (b) *DT5* and (c) *DT6* (Basak and Chakrabarti, 2013a).

All the flare events are plotted for each time bin in Fig. 4.14 and Fig. 4.15. Error bars correspond to the resolutions of the available GOES-15 X-ray data from the NOAA archive and IERC recorded VLF data. First, we note the decreasing tendency of  $\Delta t$  with increasing  $\phi_{max}$ , which we already reported during  $\alpha_{eff}$  for limited number of flares within a small span of  $Z$ . After fitting them with the empirical function (Eqn. 4-13) the fitting parameters  $a$  and  $b$  are evaluated (Table 4.2). Thereafter we calculate *reduced- $\chi^2$*  for each fit to estimate the ‘goodness of fit’ (the degrees of freedom,  $f$  corresponding to those fitting are given in Table 4.2). The *reduced- $\chi^2$*  physically represents the dominance of  $\phi_{max}$  on  $\Delta t$  during the flares at an effective ionization level of the D-region governed by  $Z$ . Six different time bins represent discrete residual ionized states caused by different path averaged  $Z$  values. The *reduced- $\chi^2$*  values are around ‘unity’ which means that the correlation is generally very good. However, as we progress from *DT1* to *DT6*, we see that the *reduced- $\chi^2$*  increases (Fig. 4.16). Thus the fitting becomes poorer and control of

$\phi_{max}$  over  $\Delta t$  weakens gradually.

So far, we discussed the nature of  $\Delta t$ . Possible physical explanation of this, at least for the low-latitude, trans-equatorial, medium length signal propagation path (NWC-IERC) can be understood by the following exercise. In Fig. 4.13, the variation of  $Z$  over  $T_x$ - $R_x$  path at mid-point of the time bins was found to be very significant. This  $Z$  variation and hence the variation of the residual ionization level of D-region over the propagation path increases monotonically from  $DT1$  to  $DT6$  (see Fig. 4.16) (Basak and Chakrabarti, 2013a). The standard deviation ( $\sigma$ ) of  $Z$  denotes the spread of it over the path.

Our findings indicate that the gradient of residual ionization level over  $T_x$ - $R_x$  path is the key determining factor of  $\Delta t$  for different classes of solar X-ray flares occurred at different times.

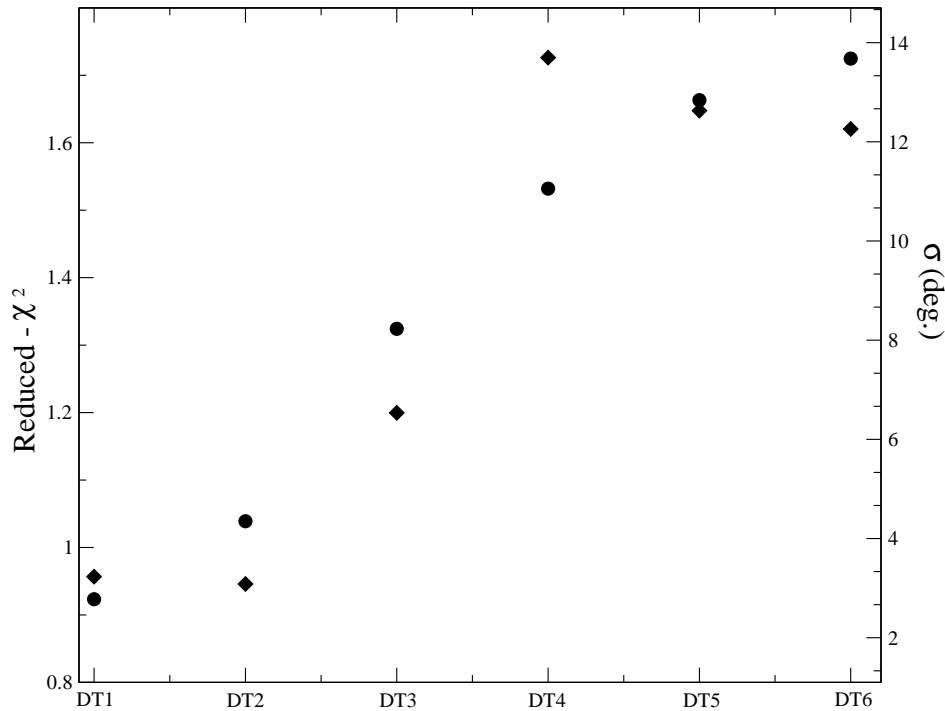


Figure 4.16: The *reduced- $\chi^2$*  (circle) and the standard deviation ( $\sigma$ ) (diamond) of the zenith angle ( $Z$ ) along  $T_x$ - $R_x$  path as functions of  $DT1$ ,  $DT2$ ,  $DT3$  etc (Basak and Chakrabarti, 2013a).

## Chapter 5

# MODELLING OF VLF SIGNALS PERTURBED BY SOLAR FLARES

### 5.1 Overview of the model and the background

Our ionosphere is a gigantic detector of extraterrestrial radiation. Study of the evolution of its chemical composition in presence of high energetic phenomena is of utmost importance not only to understand how the VLF radiation would be affected, but also to understand the overall stability of this complex system. In the present work, we apply the GEANT4 simulation (applicable to any high energy radiation detector) to understand the changes in the D-region electron density ( $N_e$ ) during flares as the ion-chemistry leaves hardly any impression on VLF propagation characteristics (Palit, Basak et al., 2013). For that reason, the knowledge of only the dominant chemical processes in the D-region ionosphere would be enough to study the modulation due to events such as solar flares (Rowe et al., 1974; Mitra, 1981; Chamberlain, 1978). One such simplified model, namely, the Glukhov-Pasko-Inan (GPI) model (Glukhov et al., 1992) can be applied for the events which cause excess ionization in the D-region. Inan et al. (Inan et al., 2006) used this model (though modified for lower altitudes) to find the effects of Gamma Ray Bursts on the state of ionization. The model has also been adopted successfully by Haldoupis (Haldoupis et al., 2009) for his work on the early VLF perturbations associated with transient luminous events.

Presently, we model the VLF signal variation due to the D-region ionospheric modulation during solar flares by combining a Monte Carlo simulation (GEANT4) for electron-ion production with the GPI model for the D-region to find the rate of free electron production at different altitudes by X-rays and  $\gamma$ -rays emitted from the flares (Palit, Basak et al., 2013). Finally, the Long Wave Propagation Capability

(LWPC) code (Ferguson, 1998) has been used to simulate the expected changes in the VLF amplitude. The LWPC code computes the amplitude and phase of the VLF signal for any arbitrary propagation path and ionospheric conditions along the path, including the effects of the earth's magnetic field. It uses the exponential D-region ionosphere defined by Wait and Spies (1964) and the waveguide mode formulation developed by Budden (1951). This program has been used by many workers and is quite successful for modeling of long-range propagation of VLF signals even in presence of ionospheric anomalies (Grubor et al., 2008; Rodger et al., 1999; Chakrabarti et al., 2012, Pal et al. 2012a, 2012b; Palit, Basak et al., 2013). Instead of Wait's model for the D-region ionosphere, we use our own result for that part of the ionosphere, by incorporating the results from the GEANT4 Monte-Carlo simulation and the GPI scheme in the LWPC program (Palit, Basak et al., 2013).

We compare the simulated VLF signal amplitude deviations due to the effect of solar flares with those of the observational data from NWC/19.8 kHz and detected by the ground based VLF receiver of the Ionospheric and Earthquake Research Centre (IERC) under Indian Centre for Space Physics (ICSP). To illustrate the success of our method, we use one X2.2 type and one M3.5 type solar flare data which occurred on 15th Feb 2011 and 24th Feb 2011 respectively and compare with the predicted VLF output from our model (Palit, Basak et al., 2013). Our interest is to reproduce the change in the VLF signal during the solar event and examine the decay of the signal during long recovery time.

## 5.2 The Model

### 5.2.1 GEANT4 Monte Carlo simulation

Geometry and Tracking (GEANT4) is a well known detector simulation program (Agostinelli et al., 2003), which includes all the required physics for the production of electron-ion pair in the atmosphere by energetic photon interactions. Most of the ionizations occur due to the collision of molecules with secondary electrons produced by initial photo ionization (Palit, Basak et al., 2013). The earth's ionosphere is a giant detector and as such, the software used to analyse detectors in high energy physics could be used here as well. Furthermore, GEANT4 is an openly available and widely tested toolkit. We simulated the rate of ionization at different altitudes due to solar X-ray photons during flares using this GEANT4 (Palit, Basak et al., 2013).

The ionosphere, constructed in the detector construction class consists of con-

centric spherical shells, so that the atmosphere is divided into several layers. The distribution of layers is chosen accordingly. They consist of average molecular densities and other parameters at those heights. The corresponding data is obtained from NASA-MSISE-90 atmospheric model (Hedin, 1991) of the atmosphere (Palit, Basak et al., 2013).

Initially, the Monte-Carlo process is triggered by primary particle generation class of GEANT4 with photons of energy ranging from 1-100 keV. We are not interested in high energy gamma ray photons as their energy deposition height is much lower than that of the D-region Ionosphere. First, a uniform spectrum where equal number of photons per keV bin is chosen as the input in primary generation class, such that the incident photons in a specific bin have random energies within the range of the bins. This gives a distribution of electron-ion production rate in a matrix form. We produce an altitude distribution by a simulation with different incident angles of the photons. For this simulation, we collect the back-ground subtracted solar spectra during the flares from Rhesi satellite data.

Several previous workers (e.g., Glukhov et al., 1992 and Haldoupis et al., 2009) approximated total energy deposition by a photon and divided it with a pre-assumed value of the average energy for production of an electron-ion pair and ultimately calculated the rate of ionization. Without such an approximation, instead, we follow the electron ionization interactions down to the lowest possible level in the Monte Carlo process (Palit, Basak et al., 2013). For this, the lower energy threshold for electron and photon processes is extended down to 10 eV in the electromagnetic processes in the GEANT4 toolkit. From simulations we found the average energy required per electron-ion pair production as  $\sim 31$  eV (Palit, Basak et al., 2013).

The ionization effect due to the solar X-ray is dominant in the D region ( $\sim 60 - 100$  km) only. The simulation also shows that the altitude of maximum ionization is somewhat lower for X-class flare ( $\sim 81$  km) than that of M-class ( $\sim 88$  km). This is consistent with the obvious result that the relative abundance of high energy photons is larger in the spectrum of an X-class flare. The effects of the zenithal variation of the Sun is included in the simulation to account for the variation of the flux in long duration flares (Palit, Basak et al., 2013).

We simulate the condition at the middle of the VLF propagation path and assume that the resulting electron density distribution apply for the whole path. Along the propagation path in question, the solar zenith angle variation is at the most  $\sim 30^\circ$  (Palit, Basak et al., 2013).

We thus compute free electron production rates per unit volume at all the rele-

vant heights for both the flares we wish to model.

### 5.2.2 The Glukhov-Pasco-Inan chemical model

To understand the ionospheric chemistry during flares, we use the Glukhov-Pasco-Inan chemical model (Glukhov et al., 1992). Here, the evolution of the number density of four types of ion species are considered. These are: electrons, positive ions, negative ions and positive cluster ions. The positive ions  $N^+$  comprise of mainly  $O_2^+$  and  $NO_2^+$ . The negative ions  $N^-$  include  $O_2^-$ ,  $CO_3^-$ ,  $NO_2^-$ ,  $NO_3^-$  etc. The positive cluster ions  $N_x^+$  are usually of the form  $H^+(H_2O)_n$ . The GPI model is meant for the night time D-region ionosphere. Modified set of equations exists (Lehtinen & Inan, 2007), which are applicable at lower heights ( $\sim 50$  km), where the inclusion of negative ion clusters  $N_x^-$  is important and the scheme has been used for the day time lower ionosphere also (Inan et al., 2007; Palit, Basak et al., 2013). However, for the altitudes of our interest in the model (above 60 km) where the VLF is reflected, the simplified model such as GPI is sufficient. We concentrate only on the ionization produced by the X-ray from solar flares. Though it is a simplification, this will produce good results as long as the electron-ion production rates due to the X-rays dominate over the regular production rates. The model is for the strong flares (at least for upper C-class and above) (Palit, Basak et al., 2013).

In the GPI scheme, time evolution of the ion densities follow ODEs, the right hand sides of which have production (+ve) and loss (-ve) terms:

$$\frac{dN_e}{dt} = I + \gamma N^- - \beta N_e - \alpha_d N_e N^+ - \alpha_d^c N_e N_x^+, \quad (5-1)$$

$$\frac{dN^-}{dt} = \beta N_e - \gamma N^- - \alpha_i N^- (N^+ + N_x^+), \quad (5-2)$$

$$\frac{dN^+}{dt} = I - B N^+ - \alpha_d N_e N^+ - \alpha_i N^- N^+, \quad (5-3)$$

$$\frac{dN_x^+}{dt} = B N^+ - \alpha_d^c N_e N_x^+ - \alpha_i N^- N_x^+. \quad (5-4)$$

The plasma neutrality condition requires,

$$N^- + N_e = N^+ + N_x^+. \quad (5-5)$$

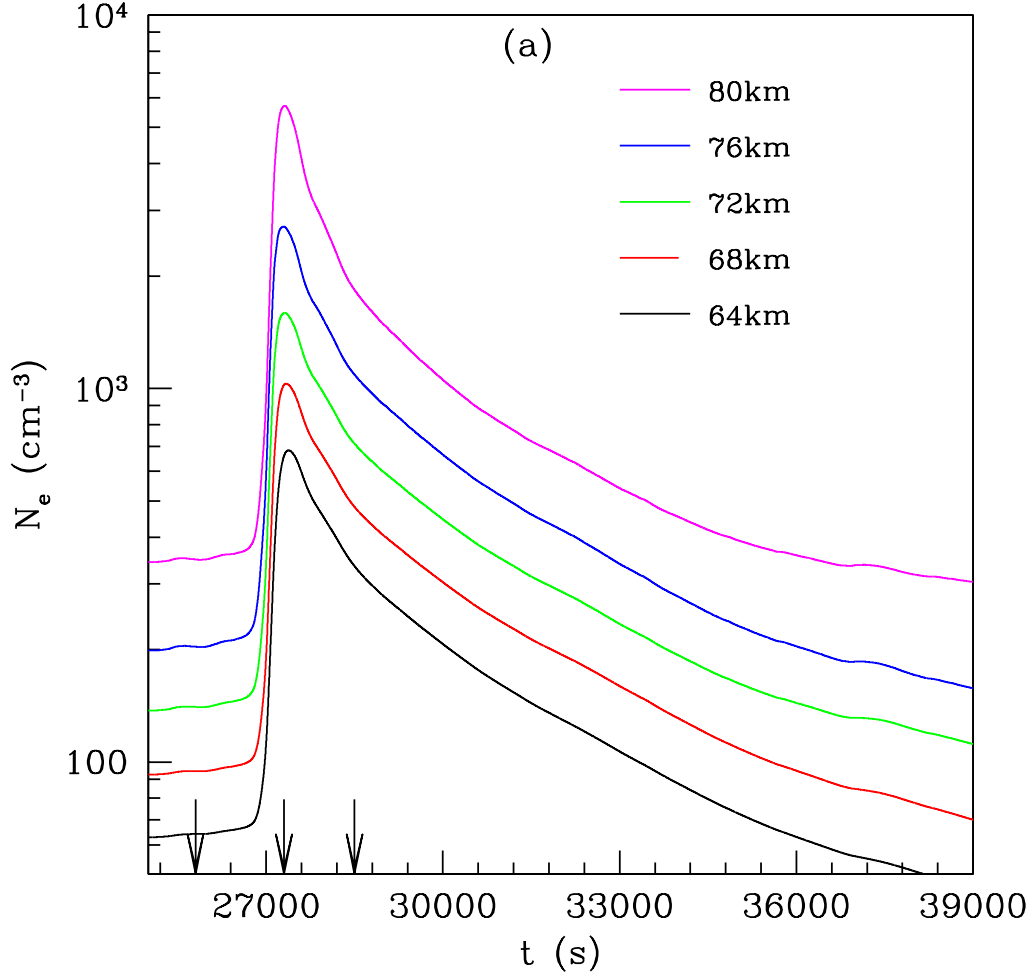


Figure 5.1: Electron density at different layers during the (a) M-class flare. The time started from 6:56:40 UT (Palit, Basak et al., 2013).

Here  $\beta$  is the electron attachment rate (Rowe et al., 1974), the value of which is given by ,

$$\beta = 10^{-31} N_{O_2} N_{N_2} + 1.4 \times 10^{29} \left(\frac{300}{T}\right) e^{(-\frac{600}{T})} N_{O_2}^2. \quad (5-6)$$

$N_{O_2}$  and  $N_{N_2}$  represent the number densities of molecular Oxygen and Nitrogen respectively, and  $T$  is the electron temperature. The neutral atom concentrations at different altitudes, required for the calculations of the coefficients were obtained from NASA-MSISE atmospheric model (Palit, Basak et al., 2013). The detachment coefficient, i.e., the coefficient of detachment of electrons from negative ions has

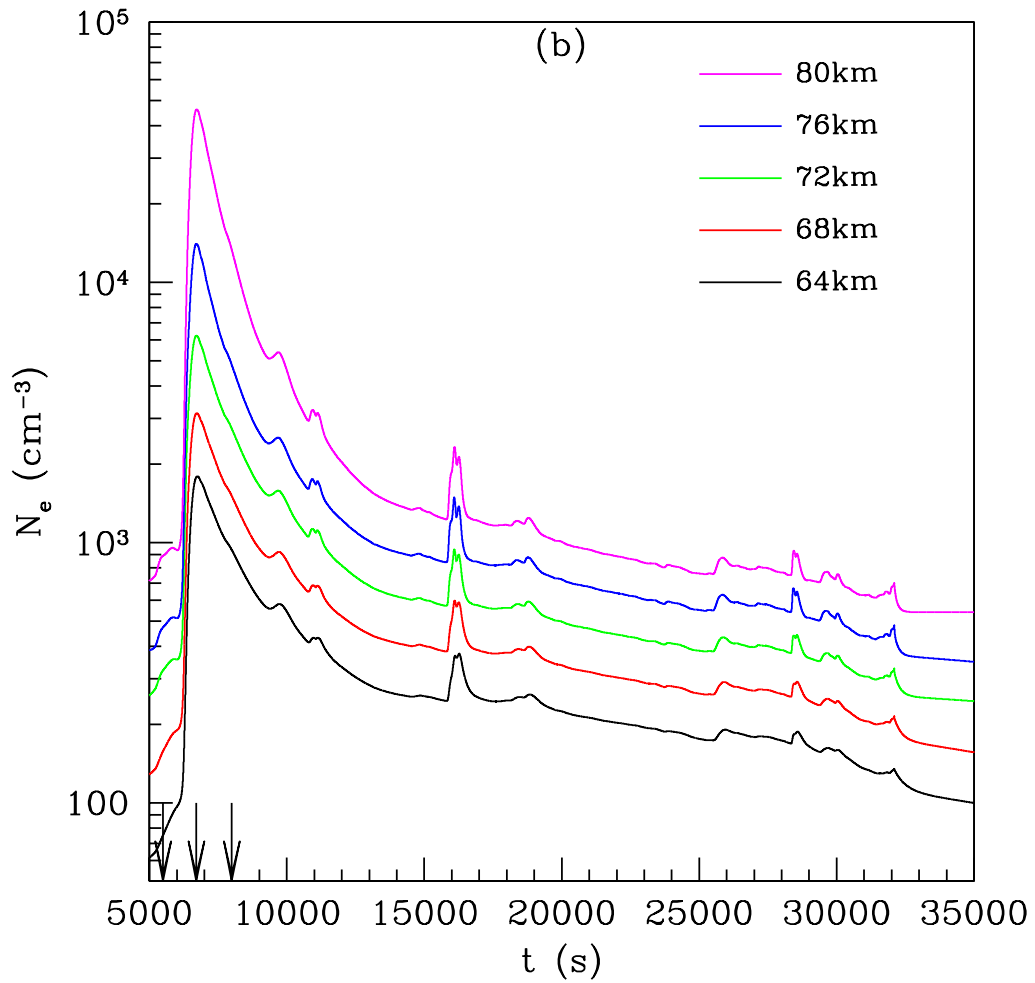


Figure 5.2: Electron density at different layers during the (b) X-class flare. The time started from 01:23:20 UT (Palit, Basak et al., 2013).

contributions from both photodetachment (at daytime) and processes other than photodetachment. The coefficient for the photodetachment process is  $\sim 10^{-2}$  to  $5 \times 10^{-1}$  and for the other process it is  $\sim 10^{-1}$  to  $10^{-2}$  at 80 km (Bragin, 1973; Palit, Basak et al., 2013). According to Lehtinen and Inan (2007) and Pasko and Inan (1994), the value of the detachment coefficient  $\gamma$  varies widely from  $10^{-23} N \text{ s}^{-1}$  to  $10^{-16} N \text{ s}^{-1}$ . Following Glukhov et al. (1992) the value of  $\gamma$  is taken to be  $3 \times 10^{-18} N \text{ s}^{-1}$ , where  $N$  is the total number density of neutrals. In our calculations the value of  $\gamma$  comes out to be  $2.4 \times 10^{-2}$  at 75 km to  $6.6 \times 10^{-3}$  at 84 km, which

is reasonable (Palit, Basak et al., 2013).

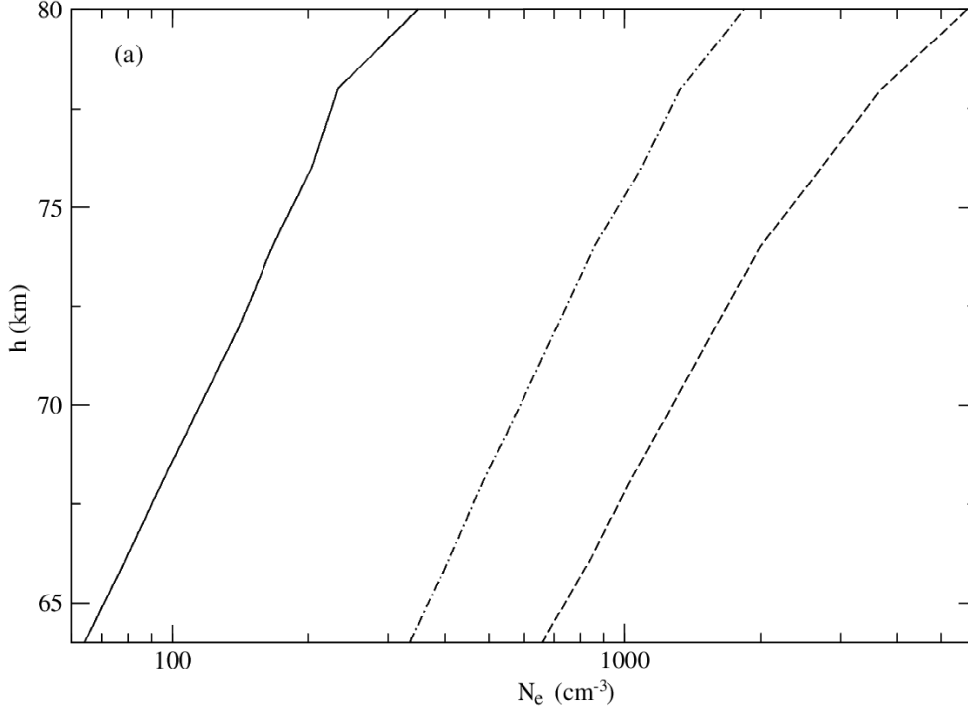


Figure 5.3: Altitude profiles of electron density as obtained from the GPI model at three different times for an M-class flare. Solid line shows the ambient profiles before the beginning of the flare while the dashed and the dot-dashed lines represent the profile during the peak and at a time during recovery (Palit, Basak et al., 2013).

We have used effective coefficient of dissociative recombination  $\alpha_d$  values as  $3 \times 10^{-7} \text{ cm}^{-3}\text{sec}^{-1}$  for  $\alpha_d$ .

The effective recombination coefficient of electrons with positive cluster ions  $\alpha_d^c$  has the value  $\sim 10^{-6} - 10^{-5} \text{ cm}^{-3}\text{sec}^{-1}$ . Here the value of  $10^{-5} \text{ cm}^{-3}\text{sec}^{-1}$  is adopted as suggested by Glukhov et al., (1982). The value of the effective coefficient of ion-ion recombination processes for all types of positive ions with negative ions is taken to be  $10^{-7} \text{ cm}^{-3}\text{sec}^{-1}$  (Mitra, 1968; Rowe et al, 1974).  $B$  is the effective rate of conversion from the positive ion ( $N^+$ ) to the positive cluster ions ( $N_x^+$ ) and has the value  $10^{-30} N^2 \text{ s}^{-1}$  (Rowe et al., 1974; Mitra, 1968), in agreement with Glukhov et al. (1992) (Palit, Basak et al., 2013).

The term  $I$ , which corresponds to the electron-ion production rate, can be written as  $I = I_0 + I_x$ . Here,  $I_0$  is from the constant source of ionization which is responsible

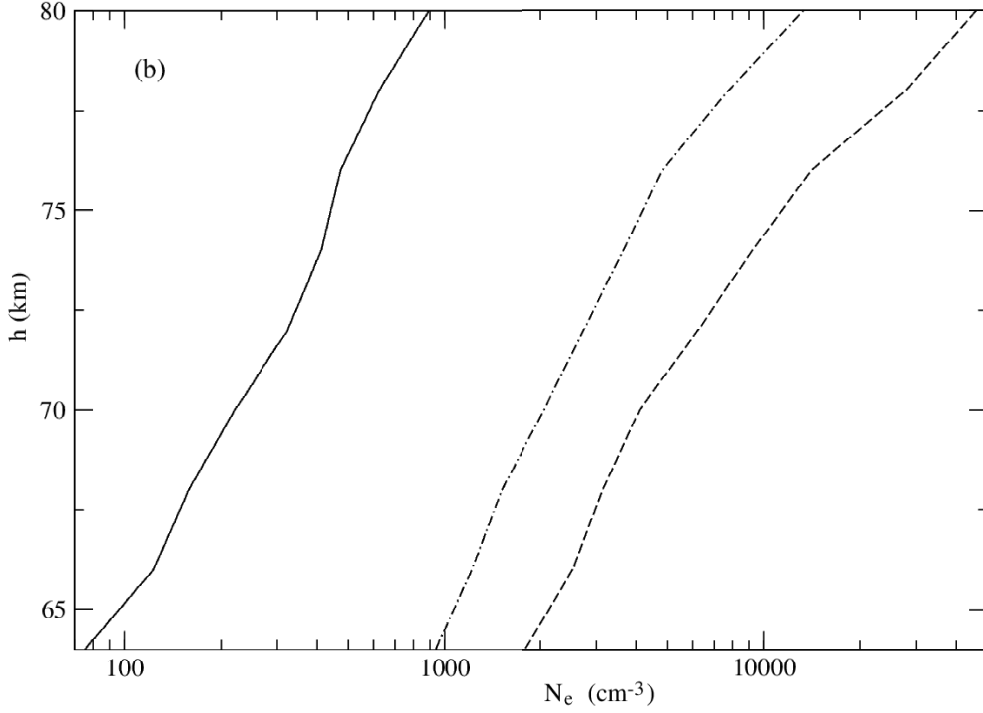


Figure 5.4: Same as Fig. 5.3 but for an X-class flare. Solid line shows the ambient profile before the beginning of the flare while the dashed and the dot-dashed lines represent the profiles during the peak and at a time during recovery (Palit, Basak et al., 2013).

for the ambient distribution of ions. In our case,  $I_0$  corresponds to the background ultraviolet ray and Lyman alpha lines etc. from the quiet Sun, which produces the D region. The  $I_x$  is generated by the X-ray photons (in the energy range from 1 to 12 keV, important for the D-region) coming from the solar corona during solar flares only (Palit, Basak et al., 2013).

To account for the time variation of the number density of the ion species, we divide each term into a constant and a time dependent parts, i.e.,  $N_e$  is replaced by  $N_{0e} + N_e(t)$ ,  $N^+$  with  $N_0^+ + N^+(t)$ ,  $N^-$  with  $N_0^- + N^-(t)$  and  $N_x^+$  with  $N_{0x}^+ + N_x^+(t)$  (Palit, Basak et al., 2013). A set of equations governing the equilibrium conditions can be obtained from Equations (5-1 to 5-4), by replacing the ion density terms with their ambient values,  $I$  by  $I_0$  and equating the production rates to zero (Glukhov et al., 1992).

Then utilizing the conditions of equilibrium and above replacements in Eqns.

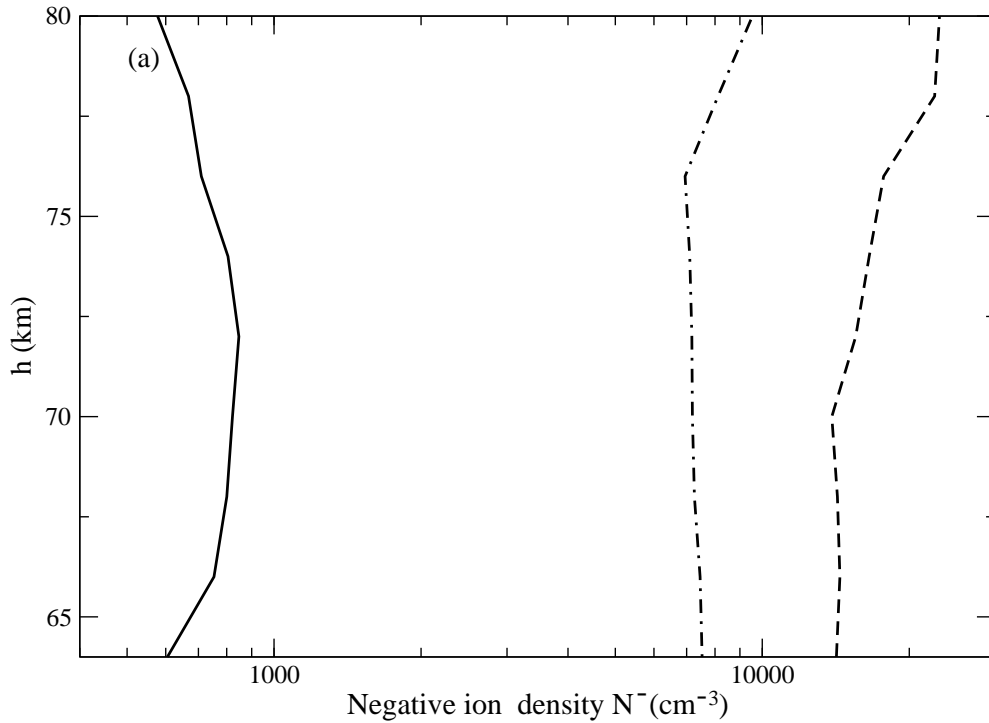


Figure 5.5: Altitude profile of the negative ions as obtained from the GPI scheme. Solid, dashed and dot-dashed lines represent respectively the ambient profile, that at the peak and at a time during recovery of the X-type flares discussed in the text (Palit, Basak et al., 2013).

(5-1 to 5-4), we get the set of equations which are applicable for flare induced lower ionosphere.

The unperturbed values of the electron and ion densities are obtained from the IRI model (Rawer et al., 1978). Unperturbed negative ion density  $N_0^-$  is obtained from the relationship  $N_0^- = \lambda N_{0e}$ , where  $\lambda$  is the relative composition of the negative ions. The values of positive ion densities are calculated from the charge neutrality condition, i.e.,

$$N_{0e} + N_0^- = N_{0x}^+ + N_0^+. \quad (5-7)$$

Using the ionization rate per unit volume ( $I_x$ ), obtained from GEANT4 simulation and the coefficients of the ODEs, calculated from MSIS data, we solve the modified ODEs by Runge-Kutta method to find the residual electron density at various altitudes during the course of the flare (Palit, Basak et al., 2013).

Figures (5.1) and (5.2) show the electron density variations at different altitudes

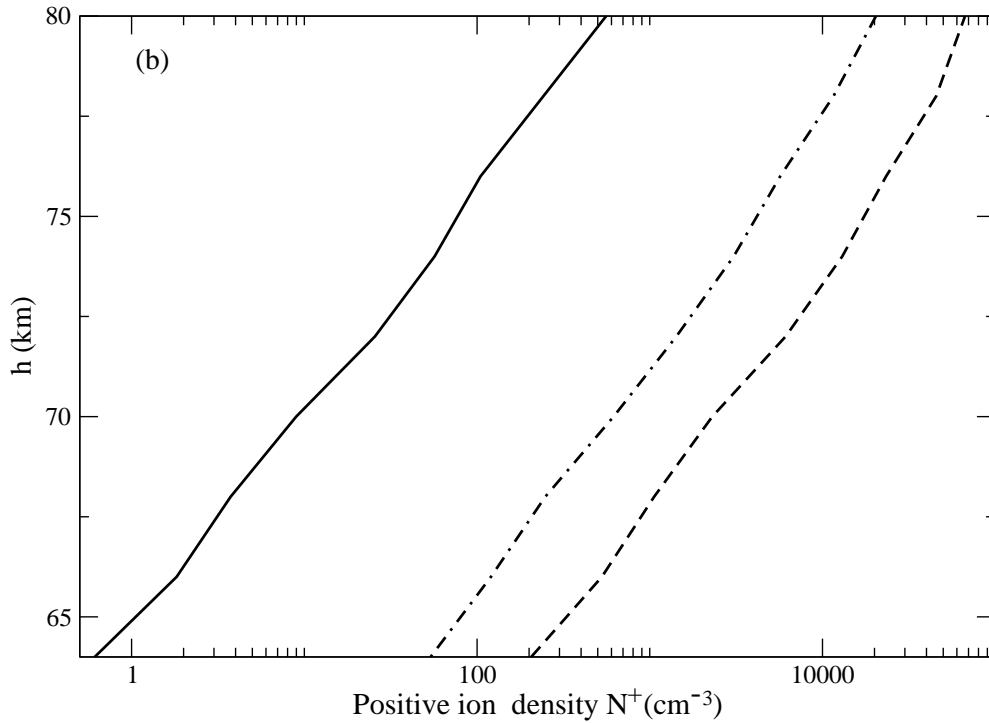


Figure 5.6: Same as Fig. 5.5 except for positive ions. Solid, dashed and dot-dashed lines represent respectively the ambient profile, that at the peak and at a time during recovery of the X-type flares discussed in the text (Palit, Basak et al., 2013).

throughout the flares. The flare time enhancement in electron density from ambient values can be clearly seen.

We follow the same procedure to obtain altitude profiles ( $N_e$ ) due to the quiet background electron density during the entire time when the M & X class flares (Figs. 5.3 and 5.4).

These are plotted at three different times including the peak time. The times are shown by arrows in Figs. (5.1) and (5.2). The ambient electron density during an X-class flare was higher than that of the M-class flare (Palit, Basak et al., 2013). This is because the background X-ray flux during the X-class flare was stronger. The height profiles of the negative ions, positive ions and positive cluster ions are presented in Figs. (5.5), (5.6) and (5.7) respectively for three different times during the flare as numerically calculated from GPI model (Palit, Basak et al., 2013).

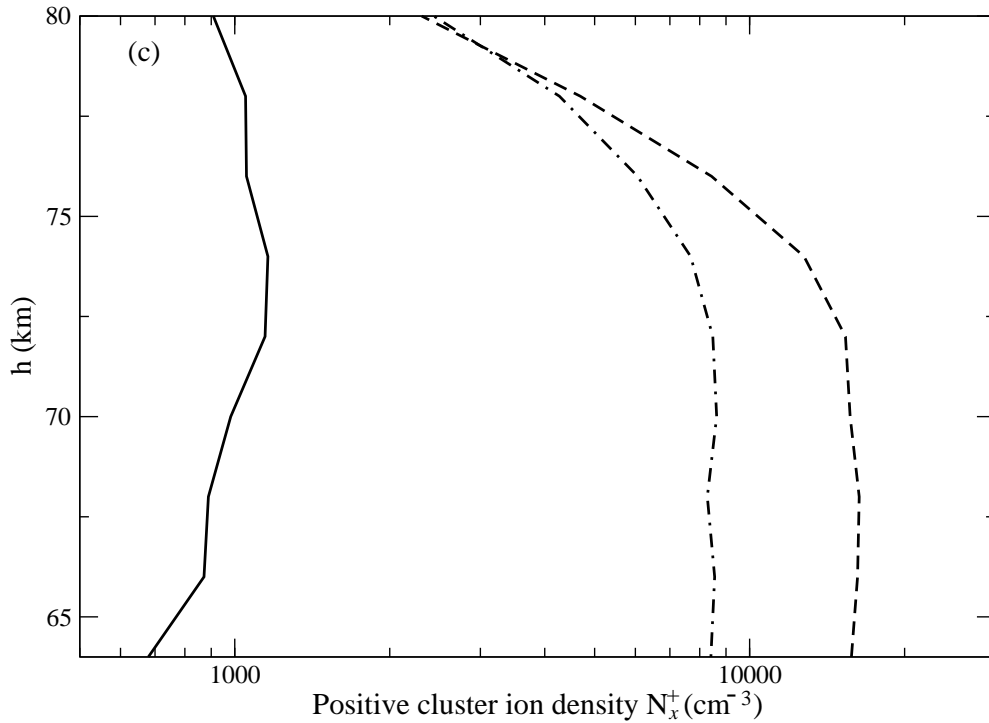


Figure 5.7: Same as Fig. 5.5 except for the Positive Cluster ions. Solid, dashed and dot-dashed lines represent respectively the ambient profile, that at the peak and at a time during recovery of the X-type flares discussed in the text (Palit, Basak et al., 2013).

### 5.2.3 LWPC modelling of VLF signal response

From the GPI model, we have the electron densities ( $N_e$ ) at various altitudes. We can input them to obtain the time variation of the deviation of the VLF signal amplitude during a flare event. We use the Long Wave Propagation Capability (LWPC) code (Ferguson, J.A., 1998) to accomplish this. The electron density profiles (Figs. 5.1 and 5.2) represent the modulated D-region ionosphere due to the solar flares and can be used as the inputs of the LWPC code to simulate the VLF signal amplitude behaviour. The electron-neutral collision frequency in the lower ionosphere plays an important role for the propagation of VLF signals. We used the collision frequency profiles between electrons and neutrals as described by Kelley (2009). This is given by the following equation,

$$\nu_e(h) = 5.4 \times 10^{-10} n_n T^{1/2}, \quad (5-8)$$

where,  $n_n$  and  $T$  are the neutral density in cubic centimetre and electron temperature in Kelvin respectively. Assuming the temperature of the electrons and the ions are the same and using the ideal gas equation the above equation can be expressed as (Schmitter, 2011; Palit, Basak et al., 2013),

$$\nu_e(h) = 3.95 \times 10^{12} T^{-1/2} \exp(-0.145h). \quad (5-9)$$

### 5.3 Results and interpretation

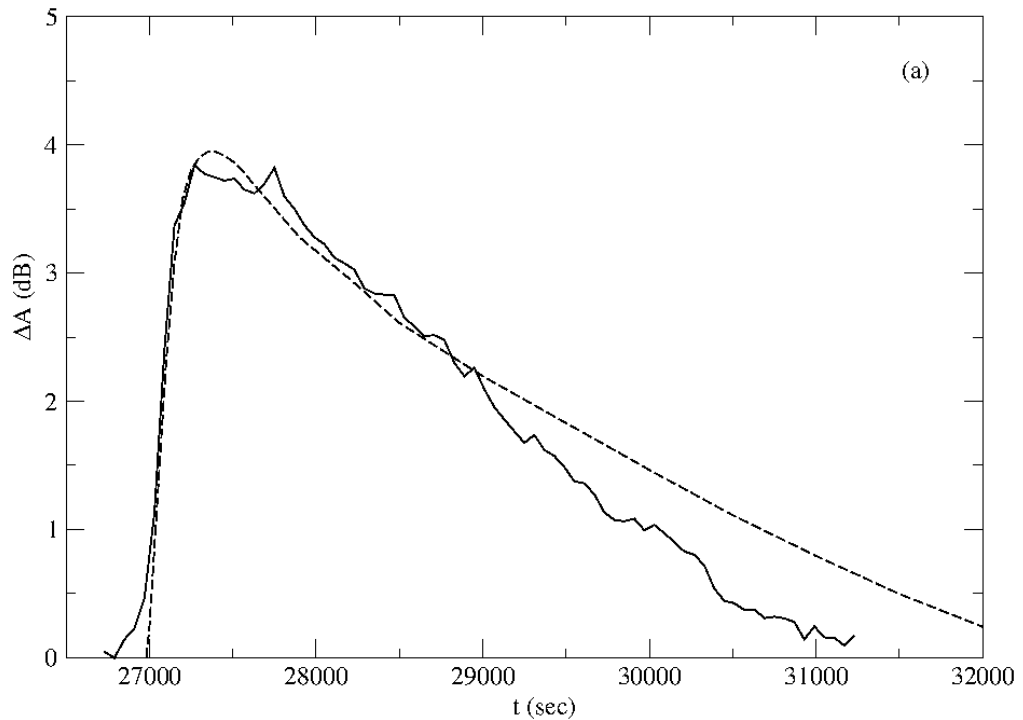


Figure 5.8: Simulation results of VLF amplitude modulations (dotted line) and corresponding observed VLF data (solid line) are plotted with UT for an M-class solar flare (Palit, Basak et al., 2013).

Using GPI model we obtained the altitude variations of the electron densities before and during the chosen flares. We now use the LWPC model to compute the resulting VLF amplitudes as a function of time. To find the observational deviation in the VLF signal due to the flares, we subtract the flare day data from the VLF data of the nearest quiet day. For the signal generated by the LWPC code also the subtraction is made, but with a constant VLF profile obtained from the ambient electron density (Palit, Basak et al., 2013).

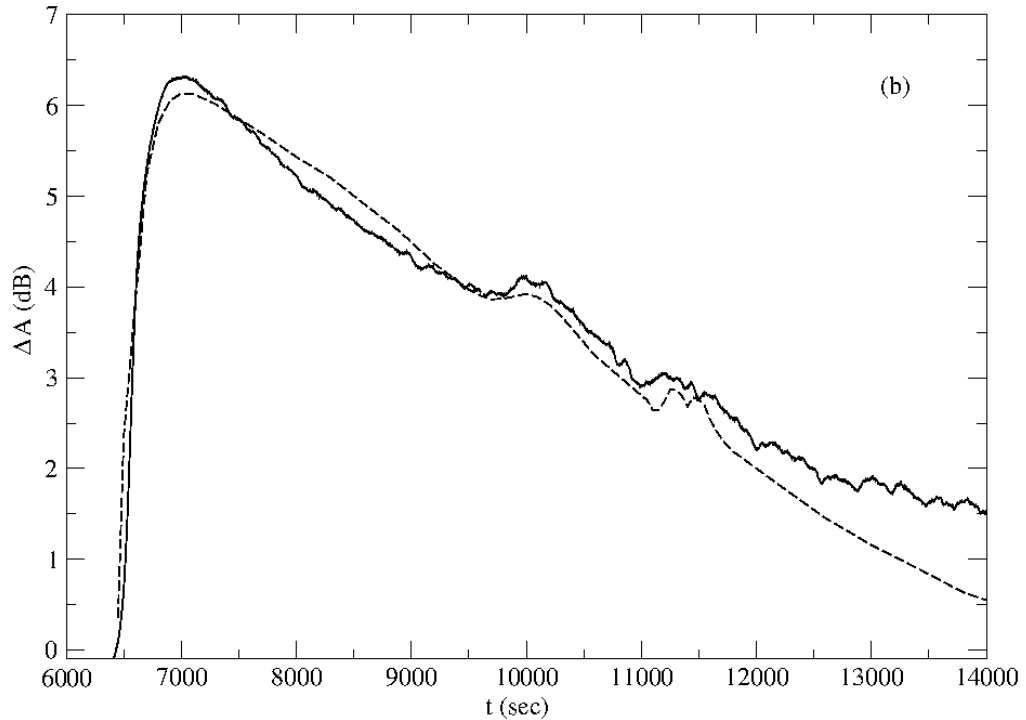


Figure 5.9: Same as Fig. 5.8 except for an X-class solar flare (Palit, Basak et al., 2013).

The response of the VLF signal to this electron distribution as obtained from the LWPC code after the appropriate subtraction of the background is shown in Figs. (5.8) and (5.9) for M and X classes of flares respectively. We see that the variations in VLF signal strengths resemble with those recorded for NWC to IERC/ICSP propagation path by IERC based receivers. For the M-class flare, the resulting VLF signals from model matches with the observation up to a certain point of time beyond which modelled slope becomes gradually smaller than that of the observation (Palit, Basak et al., 2013). For the X-class flare the modelled value of slope becomes larger than that of the observation. The M-class flare occurred at the local afternoon and X-class flare, on the other hand, occurred in the morning. The mismatch may be due to the effect of the solar zenithal angle on the ambient electron densities at various altitudes. In our simplified model, this effect was not considered (Palit, Basak et al., 2013).

We can also see (comparing Figs. 5.8 and 5.9 with Figs. 5.1 and 5.2) that the differences in slopes of decay between the models and the observations start to occur when the electron densities fall below a certain level for both the flares ( $\sim 2000 \text{ cm}^{-1}$

at 80 km) (Palit, Basak et al., 2013). Furthermore, since the M-class flare spectrum is relatively softer than that of the X-class one, the ambient (unperturbed) electron density starts to dominate the VLF amplitude a bit earlier during decay of the M-class flare. We can see that the deviation of the modelled slope from the observed one starts earlier for M-class flare than the other (Palit, Basak et al., 2013). We will work on this for further improvements.

## Chapter 6

# BEHAVIOUR OF NEGATIVE IONS IN D-REGION DURING A SOLAR FLARE

### 6.1 Introduction to $\lambda$ -parameter

The negative ions exclusively found in the D-region of the ionosphere. We already discussed the D-region chemistry in Section 1.3.1. According to Mitra (1974), the negative ions are reduced significantly above 70 km. In our case, we got almost a similar results for low latitude ionosphere above NWC-IERC propagation path (Basak and Chakrabarti, 2013b). The negative ions found are  $O^-$ ,  $O_2^-$ ,  $Cl^-$ ,  $NO_2^-$ ,  $CO_3^-$ ,  $HCO_3^-$ ,  $CO_4^-$ ,  $NO_3^-(H_2O)$ ,  $CO_3^-(H_2O)$ . Among them  $NO_3^-$  and  $CO_3^-$  are found to be chemically most dominating ions (Mitra, 1974). In this Chapter, we would discuss relative abundances of negative ions. In this case, the  $\lambda$ -parameter is defined as (Basak and Chakrabarti, 2013b),

$$\lambda = \frac{N^-}{N_e}, \quad (6-1)$$

where,  $N^-$  and  $N_e$  are the negative ions and electron densities respectively. The variation of  $\lambda$  during solar flares at several D-region heights is significant during flares. In the next few Sections, we would analyse the  $\lambda$ -profile of the D-region over NWC-IERC transequatorial low latitude path during an M-class flare (GCP is shown at Fig. 1.7). For this, we have chosen a M1.92 class flare (as detected by GOES), which occurred on the 9th Feb 2011 and was recorded by IERC/ICSP based VLF receiving system (Basak and Chakrabarti, 2013b). The amplitude ( $\Delta A$ ) and phase perturbation are shown in Fig. 6.1.

First, we simulated the electron density ( $N_e$ ) using the standard LWPC method (also see, Section 4.3.3). Then we inputted it to the generalised electron continuity equation (Deshpande et al, 1972). Finally, we evaluated the  $\lambda$ -profile.

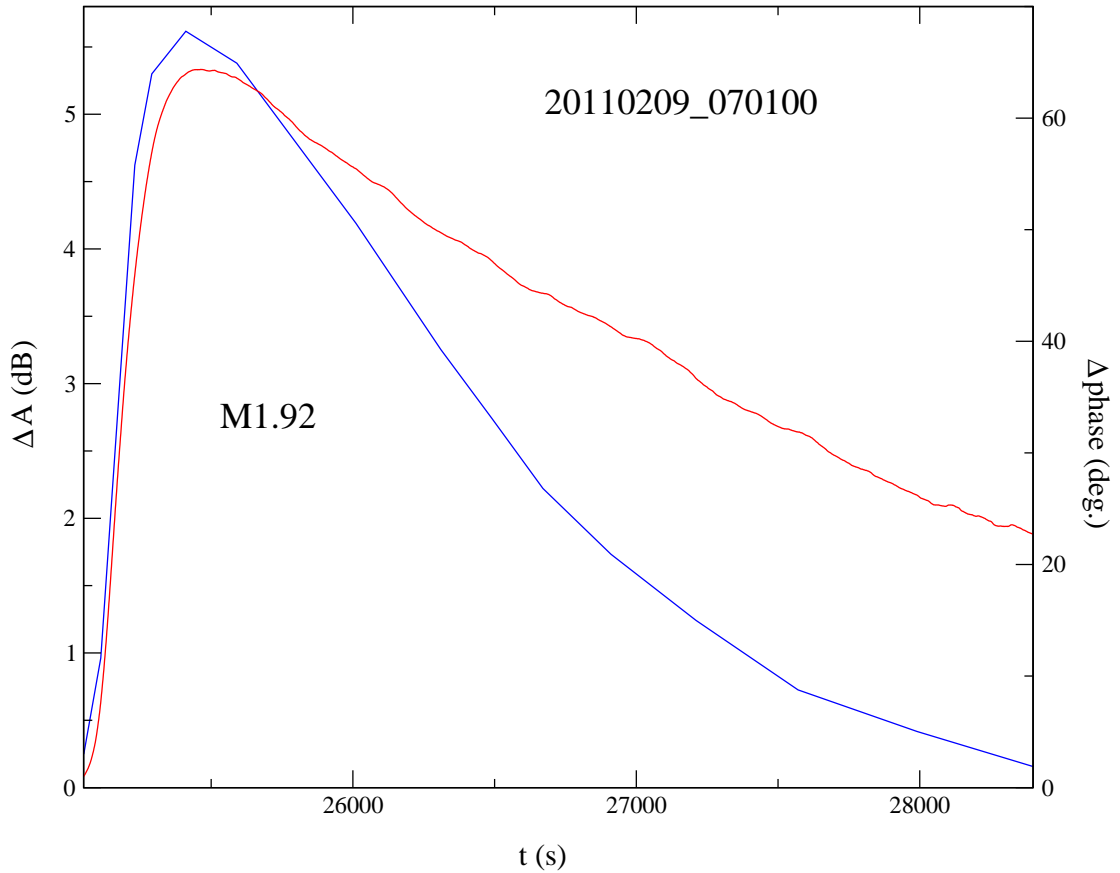


Figure 6.1: VLF amplitude ( $\Delta A$  in dB) (blue line) and phase (deg.) (red line) response of NWC/19.8 kHz signal during the M1.92 class solar flare is presented. Date and flare peak times are shown in *yyyymmdd\_hhmmss* format (Basak and Chakrabarti, 2013b).

## 6.2 Theoretical formulation of $\lambda$

### 6.2.1 LWPC simulation for enhanced electron density

Basics of LWPC code are stated in Section 1.5.3. It computes the subionospherically propagated VLF amplitude and phase response using simplified 2-parameter model of the lower ionosphere (Wait and Spies, 1964).

In Section 4.3.3, we simulated Wait's model parameters ( $h'$ ,  $\beta$ ) for several flares of different classes, but only for the peak times of the flares. Presently, we run the

simulations for the entire M1.92 class flare. Like in the earlier analysis, here also we denote the unperturbed lower ionosphere as  $h' = 74$  km and  $\beta = 0.3$  km<sup>-1</sup> and we used ‘RANGE-EXPONENTIAL model’ to deal with flare perturbed ionosphere (Basak and Chakrabarti, 2013b) which takes VLF amplitude and phase perturbations (see Fig. 6.1) as input and finally produces  $h'$  and  $\beta$  (Fig. 6.2) corresponding to the perturbed ionosphere. We used Wait’s formula (Eqn. 4-10) and calculated  $N_e$ -profile

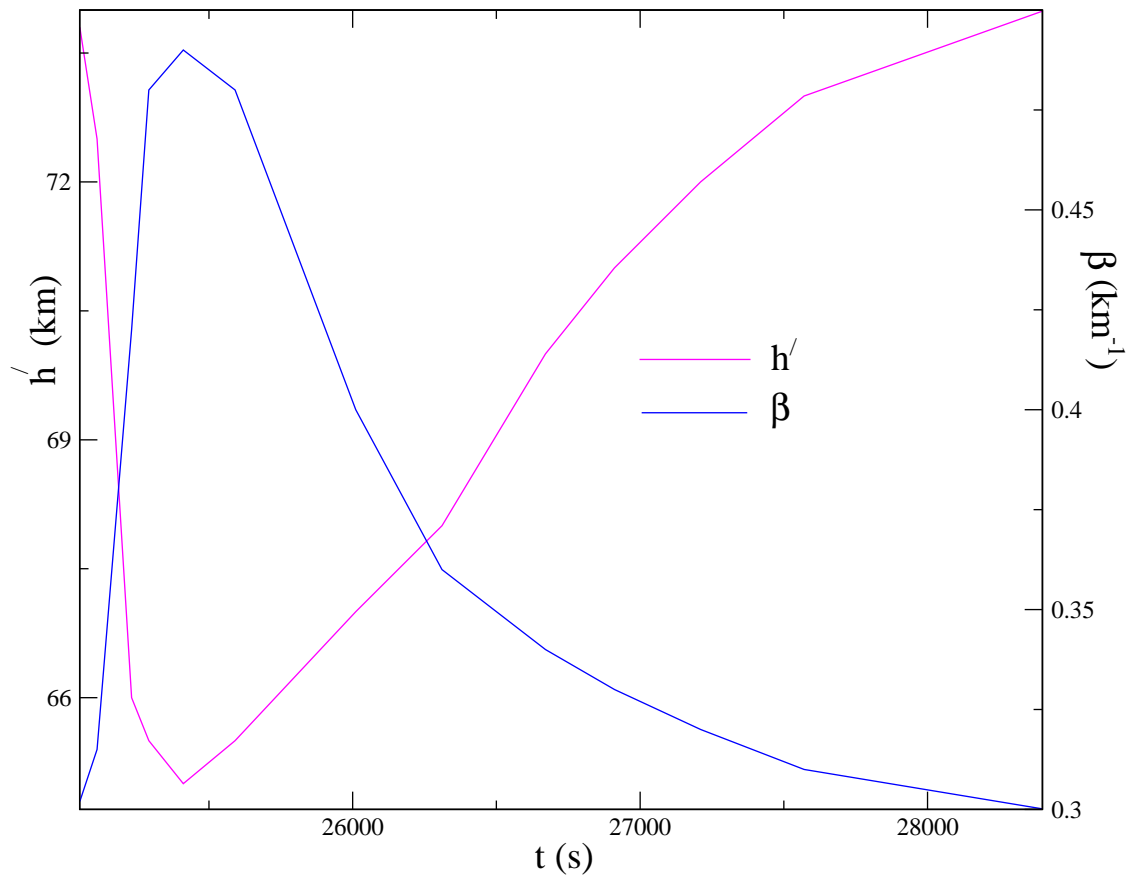


Figure 6.2: Wait’s model parameters, effective reflection height ( $h'$  in km) and sharpness factor ( $\beta$  in km<sup>-1</sup>) variations during an M1.92 class flare (as obtained from the LWPC simulation) are shown (Basak and Chakrabarti, 2013b).

at  $h = 74$  km. Fig. 6.3 shows  $N_e$  plotted with corresponding flare X-ray flux density. We observed the time delay ( $\Delta t$ ) (the most crucial parameter of analysis of previous Chapter) of the  $N_e$  peak with respect to the X-ray peak. In the relaxation regime, the  $N_e$  comes back to the pre-flare quiet values much later than the time when the

X-ray light curve does so. This directly indicates the effective relaxation time scales of D-region chemical reactions (Basak and Chakrabarti, 2013b). However, taking time derivative to Eqn. (4-10) we get,

$$\frac{dN_e}{dt} = N_e \left[ (h - h') \frac{d\beta}{dt} - \beta \frac{dh'}{dt} \right]. \quad (6-2)$$

If we supply the time derivative of  $h'$  and  $\beta$ , we can evaluate Eqn. (6-2) for heights between 65 km to 75 km (Fig. 6.4).

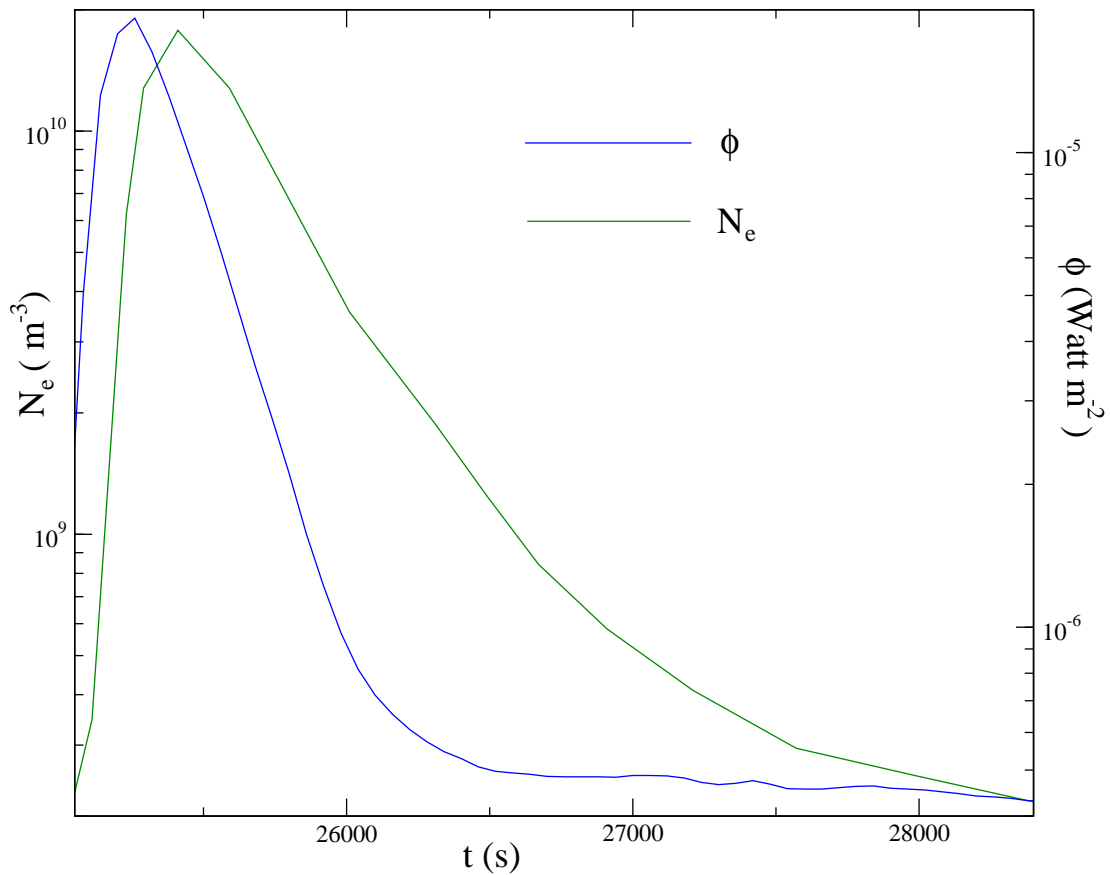


Figure 6.3: D-region electron density ( $N_e$  in  $\text{m}^{-3}$ ) (green line) at a height of 74 km as simulated using LWPC, has been plotted along with solar flare X-ray flux density ( $\phi$  in  $\text{Watt m}^{-2}$ ) (blue line) as measured by GOES-15 during an M1.92 class flare (Basak and Chakrabarti, 2013b).

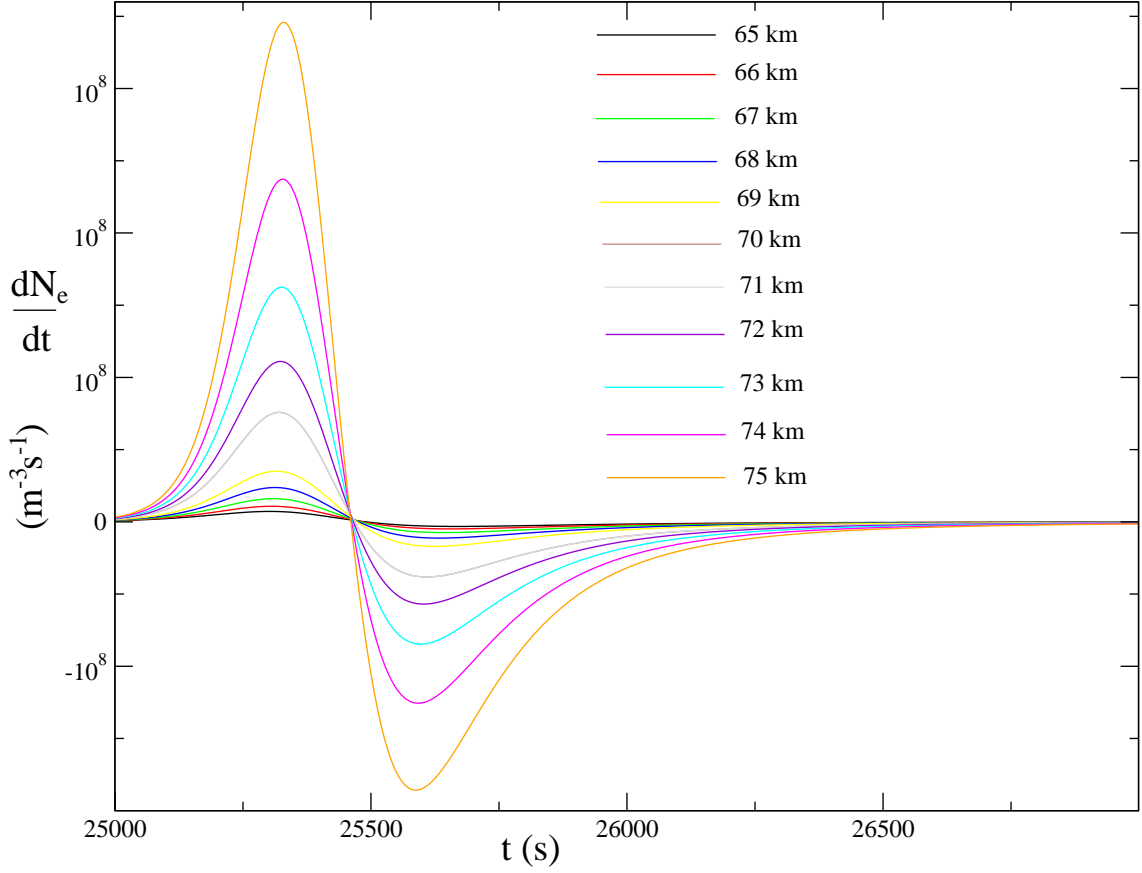


Figure 6.4: Time derivative of D-region electron density ( $\frac{dN_e}{dt}$  in  $\text{m}^{-3}\text{s}^{-1}$ ) at several heights (65-75 km) as simulated using LWPC. Different heights are indicated with separate colours (Basak and Chakrabarti, 2013b).

### 6.2.2 Solution of the continuity equation for the electrons

The generalised electron continuity equation in the D-region has already been mentioned (Eqn. 4-3), where the dissociative recombination ( $\alpha_D$ ) and mutual ionic recombination ( $\alpha_i$ ) processes are taken into account. For the purpose of the present analysis, we take,  $\alpha_D = 5 \times 10^{-12} \text{ m}^3\text{s}^{-1}$  and  $\alpha_i = 1 \times 10^{-12} \text{ m}^3\text{s}^{-1}$ , which are typical values for an M-class flare (Basak and Chakrabarti, 2013b). We calculate the electron production rate  $q(t)$  using Eqn. (4-4) and respective values of the parameters corresponding to this M-class flare. We supply previously calculated  $N_e(h, t)$  and  $\frac{dN_e}{dt}(h, t)$  using Eqns. (4-10) and (6-2) respectively. Hence the Eqn. (4-3) becomes

a first order differential equation of  $\lambda(t)$  for each height  $h$ . We solve it numerically and obtain  $\lambda(h, t)$  (Basak and Chakrabarti, 2013b).

### 6.3 Results

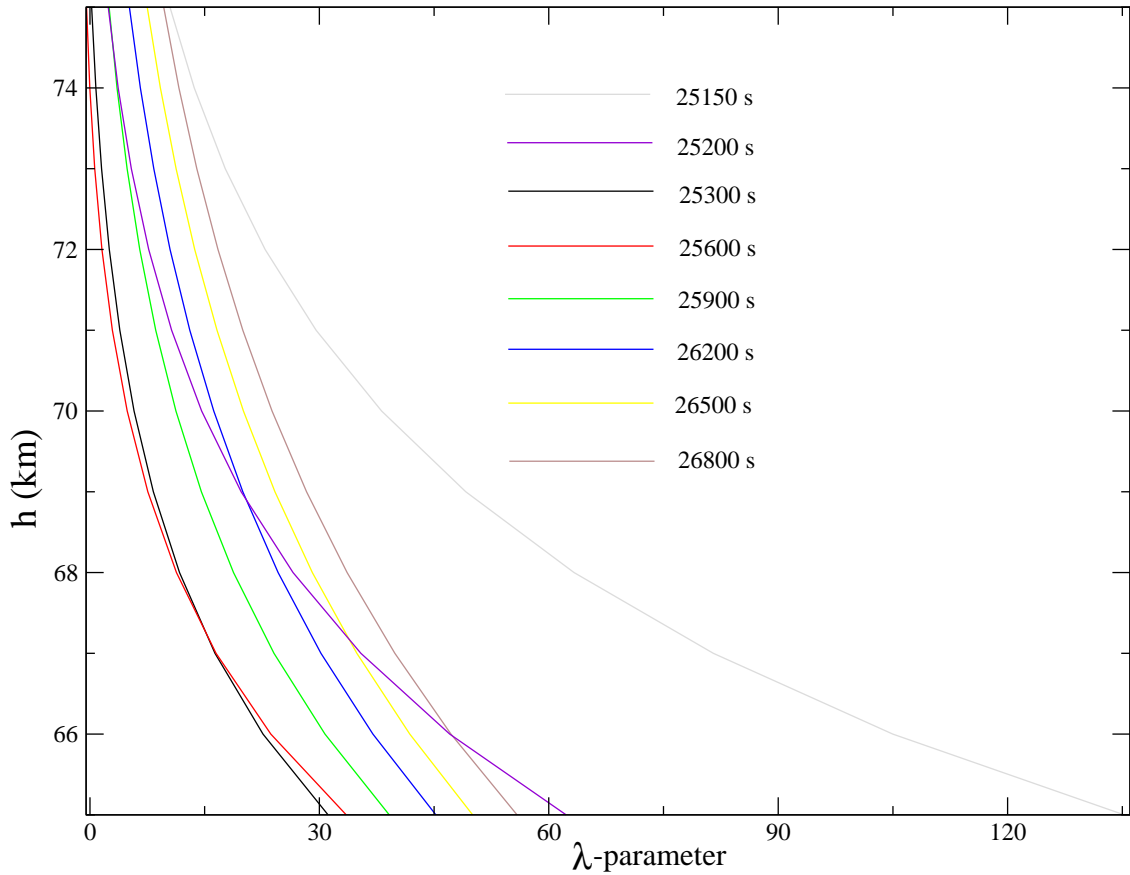


Figure 6.5: The altitude profile of  $\lambda$ -parameter at different times during the M1.92 class flares. Different colours indicate different times (Basak and Chakrabarti, 2013b).

The results of  $\lambda$  are presented in two different ways. In Fig. 6.5, we plot the altitude profile of  $\lambda$  at different times during that flare and in Fig. 6.6, we presented the temporal variation of  $\lambda$  at different D-region heights ( $h$ ) starting from 65 km to 75 km. The  $\lambda$  is reduced as height increases (Rowe et al. 1974, Mitra 1974) and our results support that. Again, above 70-72 km, the  $\lambda \sim 1$  i.e., the negative ions

are lesser in number (Mitra 1974). The results in Fig. 6.6 supports the results of Rowe et al. (1970) though they did analysis for a weak flare. We observed that in the near ionization regime of a flare,  $\lambda$  decreases and in the recombination regime, it goes up gradually (Basak and Chakrabarti, 2013b). This decrease of  $\lambda$  is primarily due to two reasons. First, the negative cluster ions are destroyed at a faster rate through mutual ionization process during a flare. Second, the production rate of the negative ion is much slower than the electron production rate  $q(t)$  (Basak and Chakrabarti, 2013b).

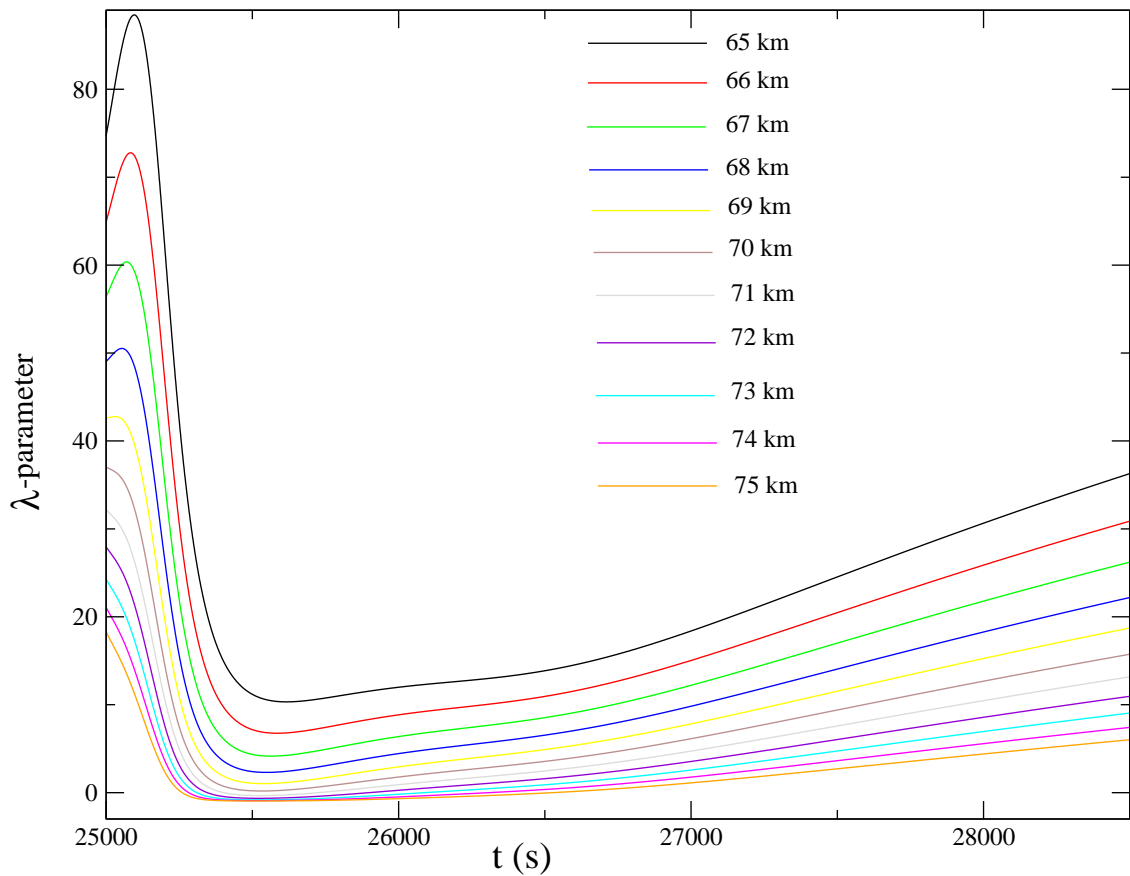


Figure 6.6:  $\lambda$ -parameter variation during the M1.92 class flare at several D-region heights (Basak and Chakrabarti, 2013b).

## Chapter 7

# CONCLUSIONS AND FUTURE PLAN

In this thesis, the main objective was to study the effects of solar energetic phenomena on the lower ionosphere using subionospherically propagating Very Low Frequency signals. Apart from the regular solar radiation effects on ionospheric weather and hence on VLF radio signal, we focussed on occasional VLF signal enhancements during solar flares and corresponding perturbations associated with D-region ionosphere. The Chapter wise conclusions are as follows.

In Chapter 1, we started with the basic details of the atmosphere and the ionosphere. We then moved to deeper discussions on the lower ionospheric chemistry and the part of the energy spectrum of solar radiation responsible for the lower ionospheric perturbations. The necessary theoretical background and computer programs based on it regarding VLF, are discussed. Finally, we presented a discussion about the parameters representing ionospheric perturbation during solar flares. As an example, we gave data corresponding to the VLF-detection of solar flares by the receiving stations at ICSP. For a better understanding of the aim of this thesis, this elaborate discussion on the background matter was necessary.

In Chapter 2, we described earlier works on the main topic of this thesis. The history of the ionospheric studies using radio wave propagation is very rich. Initial fundamental contributions of this subject are pioneered by Appleton, Mitra, Wait and other physicists. Here, we discussed different theories, models and experimental models on the effective recombination processes in the D-region during flares and other energetic events. The  $\alpha_{eff}$  is related to the flare energies and time delay (Zigman, 2007; Nina, 2012) for higher latitude paths. This earlier observations helped us to frame problems of this thesis as well as to verify the validity of already established relations for low latitude ionosphere, i.e., our propagation paths. For example, Thomson and Clilverd (2001) reported solar zenith angle ( $Z$ ) dependence of flare-events in higher latitudes, both for the short and very long paths. We

established the same type of relationship for low latitudes, trans-equatorial, mixed (sea plus land) medium length path, such as, NWC-IERC (GCP is shown at Fig. 1.7). The assumptions made, the procedure, and the results are presented in later Chapters. During our analysis, in several occasions, we took helps from the simplified D-region ion models to represent the ionosphere. So, we described models such as a 6-ion model by Mitra and Rowe (1972), GPI model by Glukhov et al. (1992) and a few others.

Our main tool to probe the solar flares is the VLF radio wave. However, before the VLF-study of our flare-perturbed ionosphere, a knowledge of the basic characteristics of the regular VLF signal in the absence of any energetic events was essential. In Chapter 3, the basic details of VLF propagation are provided. The nature of the transmitters are discussed. Details of VLF receivers used by IERC, ICSP and SNBNCBS are presented. To pictorially demonstrate the diurnal VLF signal dependence on the propagation path, latitude, transmitter stability factor, sensitivity of receiver, ground conductivity, geomagnetic field, day-night terminator interaction with propagation path etc., we plot the data for several paths, namely NWC-IERC, VTX-IERC, NWC-SNBNCBS, VTX-SNBNCBS etc. The differences in results are significant. For VTX-IERC, the daytime to nighttime amplitude ratio is  $<1$  but the opposite is true for the JJI-IERC path. Again, the same for NWC-SNBNCBS is  $>1$  and for VTX-SNBNCBS is  $<1$ . Possible reasons are the variation of the path lengths and the VLF propagation direction (east-west and west-east propagation). Moreover, we described the outcome of ICSP conducted VLF-campaigns and gave some results. These campaigns have done the groundwork for all the propagation paths and has calibrated the signal throughout the Indian subcontinent. Some of the campaign outcomes are explained through LWPC simulation results (Basak et al., 2010).

In Chapter 4, we focussed on analysing two D-region parameters, namely, the time delay ( $\Delta t$ ) and  $\alpha_{eff}$ . First, for  $\alpha_{eff}$  calculation, we analyse VLF data of 22 flares which occurred near the local mid-day in order to eliminate the effects of  $Z$  (Basak and Chakrabarti, 2013a). For all the flares presented here, we report that  $\Delta A$ ,  $\Delta t > 0$ . From Fig. 4.7, we find a decreasing trend of  $\Delta t$  with increasing  $\phi_{max}$ . From this result, we verify the Appleton (1953) relation regarding  $\Delta t$ . Most importantly, we calculated the effective recombination coefficient ( $\alpha_{eff}$ ) at the peak of these flares using a coupled theoretical model which consists of electron continuity theory and LWPC simulation (Fig. 4.8). The values of  $\alpha_{eff}$  at 74 km altitude are generally in agreement with earlier results reported by several other workers (Basak and Chakrabarti, 2013a). In the second part of this Chapter, for checking direct

connection between  $Z$  and  $\Delta t$ , we focussed on a narrow range of flare energies (C2-C7) in order that the dependence of  $\Delta t$  on  $\phi_{max}$  may be ignored (Basak and Chakrabarti, 2013a). The most important result we reported here is the linear correlation between the solar zenith angle ( $Z$ ) averaged over the propagation path at the flare time, and the time delay  $\Delta t$ . The fit is excellent as the reduced  $\chi^2$  is found to be close to unity (Basak and Chakrabarti, 2013a). We believe that when we narrow our choice of flare energies even further, the correlation would be even tighter. In the third and the final part of this Chapter, we moved towards a broader approach and we successfully analysed 78 flares of all classes. We earlier reported that the time delay of the VLF amplitude  $\Delta t$  is anti-correlated with the flare energy flux  $\phi_{max}$ . However, the relationship is not equally good at all times of the day. From the *reduced- $\chi^2$*  of the fit between the  $\Delta t$  and  $\phi_{max}$ , we note that *reduced- $\chi^2$*  is low in the early hours of the day and it worsens as the time of the occurrence of flares progresses (Basak and Chakrabarti, 2013a). To understand this behaviour, we also plot the variation of zenithal angle of the sun  $Z$  along the propagation path in different time slots. Most interestingly we find that the standard deviation of  $Z$  in each slot, when plotted against the time slots, behave similarly as the variation of *reduced- $\chi^2$*  (Fig. 4.16). Though it is true that *reduced- $\chi^2$*  is not following the  $\sigma$  for each of those *DTs* (Basak and Chakrabarti, 2013a), the overall increasing tendency of those parameters with *DTs* are comparable. This indicates that the dispersion in the  $\Delta t$  vs.  $\phi_{max}$  relationship primarily depends on how dispersed the ionization is along the propagation path and it happens specifically on the earlier times of the day i.e., at *DT1*, *DT2*, *DT3* and *DT4*. But for *DT5* and *DT6* the *reduced- $\chi^2$*  and  $\sigma$  behave in slightly opposite manner. Dominant recombination processes in the later part of the day may be the possible reason for this behaviour (Basak and Chakrabarti, 2013a).

In Chapter 5, we developed and used a 3-step computational model to simulate the VLF signal amplitude during M and X-classes of solar flares. The model consists of (i) GEANT4-Monte Carlo simulation, (ii) GPI-model of ionospheric chemistry and (iii) LWPC-model of VLF signal (Palit, Basak et al., 2013). This model is self consistent and is capable of reproducing observational results. This match is good at the ionizing regime for both of those flares but there is a little disagreement during the decay period of the flares (Palit, Basak et al., 2013). This is because the regular solar radiation on ionosphere ( $L_\alpha$ , UV) dominates during that decay period which is not included so far (Palit, Basak et al., 2013).

In Chapter 6, we dealt with the negative ion contents of the lower D-region during flares. This topic has been studied by several workers such as Mitra and

Rowe (1971), Mitra (1974), Rowe et al. (1970,73) and others. However, we did a generalised study of the variation of the  $\lambda$ -parameter both with height and time. In this purpose, we numerically solved the D-region electron continuity equation, where, we supplied the  $N_e$ -profile calculated from LWPC results (Basak and Chakrabarti, 2013b). The results generally agree with those present in the literature, namely, due to photoelectron detachment and photodissociation processes, the negative ion density during flares. However, for our VLF propagation path of interest, we found that the negative ions exist till somewhat higher altitudes ( $\sim 73$ -74 km) than the high latitude D-region heights (Basak and Chakrabarti, 2013b). Winkler and Notholt (2013) did model study on  $\text{Cl}^-$  ions and its complex compounds at nighttime in high latitude ionosphere. They report that, though negative ions are less abundant in daytime, in lower latitudes its availability increases, which supports our results.

In future, we will make a follow-up study with higher number of flares and for more than one propagation paths. Moreover, we will try to minimize the number of free parameters by doing actual simulations. The ion and electron-temperature and their comparative studies are also important parameters to investigate during flares. We would simulate cases of a composite flare where a flare occurs even before the original one is not decayed fully. These cases would give us the effects of history on the ionosphere. The VLF radiowave phase during flares may tell us more about a flare and the lower ionospheric height. Our next goal is to study effects of the geomagnetic effects such as the east-west or west-east radio signal propagation on the solar flare related perturbations in the D-region. This will be done with the use of the VLF-phase data of phase stable transmitters.

## Bibliography

- Agostinelli, S., Amako, K. et al., GEANT4 simulation toolkit, *Nuclear Instruments and Methods in Physics Research Section A: Accelerators, Spectrometers, Detectors and Associated Equipment*, Volume 506, Issue 3, 2003, Pages 250-303.
- Ananthakrishnan, S., Abdu, M. A., Piazza, L. R., D-region recombination coefficients and the short wavelengths x-ray flux during a solar flare, *Planet. Space Sci.*, 21, 367-375, 1973.
- Appleton, E. V., *Proc. Phys. Soc. (London)*, 37, 16D, 1925.
- Appleton, E. V., A note on the sluggishness of the ionosphere, *J. Atmos. Terre. Phy.*, 3, 282-284, 1953.
- Bain W. C., 1985, *IEE Proc.*, 132, Pt. H, 2, 139.
- Balachandra Swamy A. C., A new technique for estimating D-region effective recombination coefficients under different solar flare conditions, *Astroph. Space Sc.*, 185, 153-164, 1991.
- Barbar, N. F., Crombie, D. D., *JATP*, 16, 37, 1959.
- Basak, T., Chakrabarti, S. K., Pal, S., Global effects on Ionospheric weather over the Indian subcontinent at sunrise and sunset, *AIP Conf. Proc.*, 1286, 137-149, 2010.
- Basak, T., Chakrabarti, S. K., Effective recombination coefficient and solar zenith angle effects on low-latitude D-region ionosphere evaluated from VLF signal amplitude and its time delay during X-ray solar flares, *ApSS*, 2013a, (communicated).
- Basak, T., Chakrabarti, S. K., Effective negative ion profile of low-latitude D-region during solar flares evaluated from VLF signal analysis, 2013b (to be submitted).
- Berry L. A., 1964, *Radio Sci. J. Res. NBS*, 1964, 68D, 1275.

- Bragin, A. YU., 1973. Nature of the lower D region of the Ionosphere., *Nature* 245, 450 - 451, doi:10.1038/245450a0.
- Budden, K. G., The reflection of Very Low frequency radio waves at the surface of a sharply bounded ionosphere with superimposed magnetic field, *Phil. Mag.*, 42, 833-843, 1951.
- Budden, K. G., The wave-guide mode theory of wave propagation, (LOGOS Press, London) 1961.
- Burns, C. J., Turunen, E., Matveinen, J. K., *JATP*, 52, 205, 1990.
- Chakrabarti, S. K., Pal, S., Acharyya, K., Mandal, S., Chakrabarti, S., Khan, R., Bose, B., *IJP*, 76B, 693, 2002.
- Chakrabarti, S. K., Acharyya, K., Bose, B., Mandal, S., Chatterjee, A., Nandi, N. M., Pal, S., Khan, R., *IJP*, 77B, 173, 2003.
- Chakrabarti, S. K., Mondal, S. K., Sasmal, S., Pal, S., Basak, T., Chakrabarti, S., Bhowmick, D., Ray, S., Maji, S. K., Nandi, A., Yadav, V. K., Kotoch, T. B., Khadha, B., Giri, K., Garain, S. K., Choudhury, A. K., Partra, N. N., Iqbal, N., VLF signals in summer and winter in the Indian sub-continent using multi-station campaigns, *IJP*, 86(5), 323-334, 2012a.
- Chakrabarti, S.K., et al., VLF campaign during the total eclipse of July 22nd, 2009: Observational results and interpretations. *Journal of Atmospheric and Solar-Terrestrial Physics* 86, 65-70, 2012b.
- Chamberlain, Joseph W. Theory of planetary atmospheres : an introduction to their physics and chemistry; Academic, San Diego, Calif., 1978.
- Chakravarty, S. C., Gupta, S. P., Chandrasekaran, S., Middle atmospheric electro-dynamics at low latitude over India, *ASR*, 20(11), 2181-2189, 1997.
- Cummer S. A., 2000, *IEEE Tran. on Anten. Prop.*, 48, 9, 1420.
- Davies, K., *Ionospheric Radio*, IEE Electromagnetic Series 31 (book), 1990.
- Deshpande, S. D., Ganguly, S., Jain, V. C., Mitra, A. P., Ionospheric effects of solar flare-V. The flare event of 30th January 1968 and its implications, *JATP*, 34, 267-281, 1972.
- Fehsenfeld, F. C., Ferguson, E. E., Origin of water cluster ions in the D region, *JGR*, 74, 2217-2222, 1969.

- Ferguson, J. A., Computer Programs for Assessment of Long-Wavelength Radio Communications, Version 2.0., Technical document 3030, Space and Naval Warfare Systems Center, San Diego, 1998.
- Ferguson, J. A., Snyder, F. P., Naval Ocean Systems Center, San Diego, CA, 1980.
- Friedrich, M., Torkar, K. M., Steiner, R. J., Empirical recombination rates in the lower ionosphere, *ASR*, 34, 1937-1942, 2004.
- Garcia-Rigo, A., Hernandez-Pajares, M., Juan, J. M., Sanz, J., Solar flare detection system based on global positioning system data: First results, *Advances in Space Research*, 39, 889-895, 2007.
- Gledhill, J. A., The effective recombination coefficient of electrons in the ionosphere between 50 and 150 km, *Radio Sc.*, 21(30), 399-408, 1986.
- Glukhov V.S., Pasko V.P., Inan U.S., Relaxation of transient lower ionospheric disturbances caused by lightning-whistler-induced electron precipitation bursts; *Journal of Geophysical Research*. 97(A11), 16971-16979, 1992.
- Grubor, D., Sulic, D., Zigman, V., Influence of solar X-ray flares on the earth-ionosphere waveguide, *Serb. Astron. J.* 171, 29-35, 2005.
- Grubor, D., Sulic, D., Zigman, V., Classification of X-ray solar flares regarding their effects on the lower ionosphere electron density profile, *Ann. Geophys.*, 26, 1731-1740, 2008.
- Haldoupis C., Mika A., Shalimov S.; Modeling the relaxation of early VLF perturbations associated with transient luminous events; *Journal of Geophysical Research*, VOL. 114, A00E04, 11 PP., 2009.
- Han, F., Cummer, S. A., Li, J., Lu, G., Daytime ionospheric D region sharpness derived from VLF radio atmospheric, *JGR*, 116, A05314, 2011.
- Hargreaves, J. K., Birch, M. J., *Annales Geophysicae*, 23, 3267-3276, 2005.
- Hedin A.E. Extension of the MSIS Thermosphere Model into the middle and lower atmosphere; *Geophysical Research Letters* 96, NO. A2, P. 1159, 1991.
- Hinteregger, H. E., *JGR*, 66, 2367, 1961.
- Holloway, A. M., Wayne, R. P., *Atmospheric Chemistry* (book), RSC Publishing, 2010.

- Hunsucker, R. D. and Hargreaves, J. K., 2003, The high-latitude ionosphere and its effects on radio propagation, Cambridge University Press, USA.
- Inan U. S., Cohen M. B., Said R. K., Smith D. M., Lopez L. I.; Terrestrial gamma ray flashes and lightning discharges; *Geophysical Research Letters*, vol. 33, 118802, 5 PP., 2006.
- Inan U. S., Lehtinen N. G., Moore R. C., Hurley K., Boggs S., Smith D. M., Fishman G. J.; Massive disturbance of the daytime lower ionosphere by the giant g-ray flare from magnetar SGR 1806-20 ; *Geophysical Research Letters*, vol.34, L08103, 2007.
- Kasturirangan, K., Rao, U. R., Sharma, D. P., Rastogi, R. G., Chakravarty, S. C., Ionospheric effects of transient celestial X-ray and gamma-ray events, *Astrophys. Space Sc.*, 42(1), 57-62, 1976.
- Kelley, M. C.: *The Earths Ionosphere, Plasma Physics and Electrodynamics*, chapter 2.2, Academic Press, second edition, 2009.
- Le, H., Liu, L., Chen, B., Lei, J., Yue, X., Wan, W., Modeling the responses of the middle latitude ionosphere to solar flares, *Journal of Atmos. and Solar-Terr. Phy.*, 69, 1587-1598, 2007.
- Le, H., Liu, L., Chen, Y., Wan, W., Statistical analysis of ionospheric responses to solar flares in the solar cycle 23, *Journ. of Geo. Res.*, doi:10.1029/2012JA017934, 2012.
- Lehtinen N. G., Inan U. S.; Possible persistent ionization caused by giant blue jets; *Geophysical Research Letters*, Vol. 34, L08804, doi:10.1029/2006GL029051, 2007.
- Lynn, K. J. W., VLF waveguide propagation: The basics, *AIP Conf. Proc.*, 1286, 3-41, 2010.
- McRae, W. M., Thomson, N. R., Solar flare induced ionospheric D-region enhancements from VLF phase and amplitude observations, *Journ. Atmos. and Sol. Terre. Phy.*, 66, 77-87, 2004.
- Mitra, A. P., Jones, R. E., Recombination in the lower ionosphere, *JGR*, 50(3), 391-406, 1953.
- Mitra, A. P., *JATP*, 10, 140-152, Pergamon Press Ltd, London, 1957.
- Mitra, A. P., Recombination processes in the ionosphere, *Advan. in Upper Atmos. Res.*, Ed. Landmark, Pergamon press, 57-87, 1963.

- Mitra, A. P., A review of D-region processes in non-polar latitudes *Journal of Atmospheric and Terrestrial Physics*, 30(6), 1065-1114, 1968.
- Mitra, A. P., Rowe, J. N., Ionospheric effects of solar flares - VI. Changes in D-region ion chemistry during solar flares, *JATP*, 34, 795-806, 1972.
- Mitra, A. P., Rowe, J. N., Ionospheric constraints of mesospheric nitric oxide, *JATP*, 36, 1797-1808, 1974.
- Mitra, A. P., Ionospheric effects of solar flares, D.Reidel Pub. Co., Holland, 1974.
- Mitra, A. P. (1981) Chemistry of middle atmospheric ionization-a review *Journal of Atmospheric and Terrestrial Physics*, 43 (8). pp. 737-752. ISSN 0021-9169.
- Mitra, S. K., The upper atmosphere, The Asiatic Society, Calcutta, 1992.
- Narcisi, R. S., et al., Aeronomy Report No. 32, University of Illinois, USA, 1969.
- Narcisi, R. S., Baily, A. D., Della Lucca, L., Sherman, C., Thomas, D. M., *JATP*, 33, 1147, 1971.
- Nina, A., Cadez, V., Sulic, D., Sreckovic, V., Zigman, V., Effective electron recombination coefficient in ionospheric D-region during the relaxation regime after solar flare from February 18, 2011, *Nuclear Instruments and Methods in Physics Research B*, 279, 106-109, 2011.
- Osepian, A., Kirkwood, S., Dalin, P., Tereschenko, V., D-region electron density and effective recombination coefficients during twilight-experimental data and modelling during solar proton events, *Ann. Geo.*, 27, 3713-3724, 2009.
- Parthasarathy, R., Rai, D. B., Effective recombination coefficient in D-region, Scientific Report No. 1, Geophy. Inst. of the Univ. of Alaska, 1965.
- Pal, S., Chakrabarti, S. K., Theoretical models for computing VLF wave amplitude and phase and their applications, *AIP Conf. Proc.*, 1286, 42-60, 2010.
- Pal, S., Basak, T., Chakrabarti, S. K., Results of computing amplitude and phase of the VLF wave using wavehop theory, *Ad. Geo.*, 27, 1-11, 2011.
- Pal, S., Chakrabarti, S. K., Mondal S. K., Modeling of sub-ionospheric VLF signal perturbations associated with total solar eclipse, 2009 in Indian subcontinent, *Advances in Space Research*, 50, issue 2, 196-204, 2012.

- Pal, S., Maji, S. K., Chakrabarti, S. K., First ever VLF monitoring of the lunar occultation of a solar flare during the 2010 annular solar eclipse and its effects on the D-region electron density profile, *Planetary and Space Sc.*, 73, 310-317, 2012.
- Palit, S., Basak, T., Mondal, S. K., Pal, S., Chakrabarti, S. K., Modelling of the Very Low Frequency (VLF) radio wave signal profile due to solar flares using the GEANT4 Monte Carlo simulation coupled with ionospheric chemistry, *ACPD*, 13, 6007-6033, 2013.
- Poppoff, I. G., Whitten, R. C., D-Region Ionization by Solar X Rays, *JGR*, 67(7), 2986-2988, 1962.
- Pant, P., Relation between VLF phase deviations and solar X-ray fluxes during solar flares, *Astroph. Space Sc.*, 209, 297-306, 1993.
- Pozo, C. F. del, Hargraves, J. K., Aylward, A. D., Ion composition and effective ion recombination rate in the nighttime auroral lower ionosphere, *JASTP*, 59(15), 1919-1943, 1997.
- Qian, L., Burns, A. G., Chamberlin, P. C., Solomon, S. C., Variability of thermosphere and ionosphere responses to solar flares, *Journal of Geo. Res.*, 116, A10309, 2011.
- Rishbeth, H., Garriott, O. K., Introduction to Ionospheric Physics, Academic Press, London (book), 1969.
- Rodger, C. J., M. A. Clilverd, and N. R. Thomson, Modeling of subionospheric VLF signal perturbations associated with earthquakes, *Radio Sci.*, 34, 1177-1185, 1999.
- Rowe, J. N., Ferraro, A. J., Lee, H. S., Kreplin, R. W., Mitra, A. P., Observations of electron density during a solar flare, *JATP*, 32, 1609-1614, 1970.
- Rowe, J. N.; Mitra, A. P.; Ferraro, A. J.; Lee, H. S. An experimental and theoretical study of the D-region - II. A semi-empirical model for mid-latitude D-region. *Journal of Atmospheric and Terrestrial Physics*, Vol. 36, p. 755 - 785, 1974.
- Schmitter, E. D., Remote sensing planetary waves in the mid-latitude mesosphere using low frequency transmitter signals, *Ann. Geo.*, 29, 1287-1293, 2011.
- Schunk, R. W. (Editor), Solar-Terrestrial Energy Program, Handbook of Ionospheric Models, CASS, Utah State University, Logan, 1996.

- Sharma, D. P., Jain, A. K., Chakravarty, S. C., Kasturirangan, K., Ramanathan, K. R., Rao, U. R., Possibility of continuous monitoring of celestial X-ray sources through their ionization effects in the nocturnal D-region ionosphere, *Astrophys. Space Sc.*, 17(2), 409-425, 1972.
- Sharma, D. K., Rai, J., Israil, M., Subrahmanyam, P., Chopra, P., Garg, S. C., Enhancement in electron and ion temperatures due to solar flares by SROSS-C2 satellite, *Ann. Geo.*, 22, 2047-2052, 2004.
- Tascione, T. F., 1994, *Introduction to the Space Environment*, Krieger Publishing Company, Malabar, FL, USA.
- Thomson, N. R., Clilverd, M. A., Solar flare induced ionospheric D-region enhancements from VLF amplitude observations, *J. Atmos. and Terres. Phys.*, 63, 1729-1737, 2001.
- Thomas, L., Bowman, M. R., *JATP*, 47, 547-556, 1985.
- Thomson, N. R., Rodger, C. J., Clilverd, M. A., Large solar flares and their ionospheric D region enhancements, *J. Geophys. Res.*, 110, A06306, 2005.
- Tsurutani, B. T., Verkhoglyadova, O. P., Mannucci, A. J., Lakhina, G. S., Li, G., Zank, G. P., A brief review of "solar flare effects" on the ionosphere, *Radio Science*, 44, RSOA17, 2009.
- Turunen, E., Matveinen, H., Ranta, H., Sodankyla Ion Chemistry (SIC) Model. SGO Report No. 49, Sodankyla, Finland, 1992.
- Valnicek, B., Ranzinger, P., X-ray emission and D-region 'sluggishness', *Bulletin of the Astronomical Institute of Czechoslovakia*, 23, 318-322, 1972.
- Wagner, L. S., Thome, G. D., Measurement of E-layer effective recombination coefficient during solar flares, *Radio Sc.*, 7(4), 469-480, 1972.
- Wait, J. R., *Electromagnetic Waves in Stratified Media*, Pergamon Press, Oxford, 1962.
- Wait, J. R., *Introduction to antennas and Propagation*, Peter Peregrinus Ltd. London, 1986.
- Wait, J. R., Spies, K. P., Characteristics of the earth-ionosphere waveguide for VLF radio waves, *NBS Tech. Note* 300, 1964.

- Wakai, N., Kurihara, N. and Otsuka, A.: (2004) Numerical method for calculating LF sky-wave and their resultant wave field strengths, *Electronics letter*, **40**, No. 5.
- Whitten, R. C., Poppoff, I. G., A model of Solar-Flare-Induced Ionization in the D Region, *JGR*, 66(9), 2779-2786, 1961.
- Whitten, R. C., Poppoff, I. G., Associative Detachment in the D Region, *JGR*, 67(3), 1183-1185, 1962.
- Whitten, R. C., Poppoff, I. G., Edmonds, R. S., Berning, W. W., Effective recombination coefficients in the lower ionosphere, *JGR*, 70(7), 1737-1742, 1965.
- Winkler, H., Notholt, J., *ASR*, 51 (12), 2342-2352, 2013.
- Yoshida M., Yamauchi T., Horie T. et al., 2008, *NHESS*, 8, 129.
- Zhang, D. H., Mo, X. H., Cai, L., Zhang, W., Feng, M., Hao, Y. Q., Xiao, Z., Impact factor for the ionosphere total electron content response to solar flare irradiation, *Journ. of Geo. Res.*, 116, A04311, 2011.
- Zigman, V., Grubor, D., Sulic, D., D-region electron density evaluated from VLF amplitude time delay during X-ray solar flares, *J. Atmos. and Terres. Phys.*, 69, 775-792, 2007.